

**MATHEMATICAL MODELLING OF THE INFLUENCE OF
ELECTROSTIMULATION IN THE OSSEOINTEGRATION
OF DENTAL IMPLANTS**

By:

Juan Carlos Vanegas Acosta

Doctorado en Ingeniería - Ciencia y tecnología de los materiales

Promoter:

Diego Alexander Garzón Alvarado, Ph.D.

Departamento de Ingeniería Mecánica y Mecatrónica



Grupo de Modelado Matemático y Métodos Numéricos GNUM

Universidad Nacional de Colombia - Facultad de Ingeniería

Departamento de Ingeniería Mecánica y Mecatrónica

Bogotá, Colombia, March 2013

Electrostimulation denotes the influence of a static electric field (EF) on cell behavior and tissue formation. Several electrostimulation techniques have been reported to yield both increased rates of tissue recovery and reduced healing times in wounds. In dentistry, such techniques are being study and implemented to increase the bone formation around dental implants, which are devices inserted in the jaw bone to replace the root of a missing tooth. Although the biological effects of electrostimulation are well documented by experimental evidence, the exact underlying biological mechanisms influenced by the EF are still matter of discussion. In order to fill the gap, numerical models have gained interest as useful tools for providing information about the interaction paths.

The purpose of this research is to analyze possible EF interaction mechanisms that may take place during bone formation around a dental implant using a numerical approach. Accordingly, we have formulated and implemented mathematical models describing the influence of the EF in the most critical biological processes leading to bone formation at the bone-dental implant interface. The numerical solutions reproduce the distribution of spatial-temporal patterns describing the influence of EF during blood clotting, cell migration, granulation tissue formation and formation of new bone. Since the numerical approach also allows us to analyze the influence of both chemical and electrical stimuli on cell dynamics, a numerical study of cell migration in the presence of an electric field, or electrotaxis, is also conducted.

Numerical results indicate that electrostimulation promotes blood clot formation near the implant surface. Moreover, the presence of the electrical stimulus directs cell migration and increases the cell migration speed in agreement with the experimental findings on cell electrotaxis. A higher cell migration also accounts for a larger number of cells colonizing the implant surface. Furthermore, formation of granulation tissue in the presence of an EF is higher near the implant surface. Since the EF exposure increases both cell colonization and new tissue formation at the implant surface, numerical calculations show that the use of electrostimulation induces new bone formation at the bone-dental implant interface up to osseointegration (anchoring of the dental implant with the host bone) in less amount of time.

These results are in agreement with experimental observations, and provide additional information on the EF interaction mechanisms with cells and tissues during wound healing, and ultimately, towards osseointegration. Given this agreement, the numerical framework is suitable to explore electrostimulation in other clinical scenarios, especially those dealing with different types of tissues and other electrostimulation modalities.

1	Introduction	1
1.1	Background	1
1.2	Scope of the research	2
1.3	Objectives of the research	3
1.3.1	General objective	3
1.3.2	Specific objectives	3
1.4	Outline of this thesis	3
2	Dental implants	6
2.1	Introduction	6
2.2	The bone-dental implant interface	7
2.3	Osseointegration	9
2.4	Mechanobiology of the bone-dental implant interface	10
2.5	Electrostimulation and bone growth	12
2.6	Modeling osseointegration	13
3	Biological modeling using FEM	17
3.1	Introduction	17
3.2	The reaction-diffusion equation	18
3.3	Biological models	19
3.3.1	Schnakenberg model	19
3.3.2	Glycolysis model	19
3.3.3	Chemotaxis model	20
3.4	The finite elements method	20
3.5	Numerical implementation	26
3.5.1	Schnakenberg model	26
3.5.2	Glycolysis Model	28
3.5.3	Chemotaxis Model	31
3.6	Characteristics of the solutions	33

4	Mathematical modeling of cell electrotaxis	36
4.1	Introduction	36
4.2	Mathematical model	37
4.3	Description of the simulation	39
4.3.1	Analyzed cases	41
4.4	Results	42
4.4.1	First case: Electrotaxis	42
4.4.2	Second case: Chemotaxis opposed to electrotaxis	46
4.4.3	Third case: Electrotaxis aided by chemotaxis	49
4.4.4	Forth case: Electrotaxis independent of chemotaxis	50
4.5	Discussion	51
5	Modeling electrically stimulated blood clotting	57
5.1	Introduction	57
5.2	Blood clotting and electrical stimulation	58
5.3	Mathematical model	59
5.4	Description of the simulation	61
5.5	Results	62
5.6	Discussion	64
6	Modeling electrically stimulated osteogenesis	67
6.1	Introduction	67
6.2	Mathematical model	68
6.3	Description of the simulation	72
6.3.1	Analyzed cases	74
6.4	Numerical results	75
6.5	Discussion	82
7	Perspectives and conclusion	86
Appendix A	List of parameters	89
A.1	Parameters for the model of cell electrotaxis (Chapter 4)	89
A.2	Parameters for the model of blood clotting (Chapter 5)	90
A.2.1	Dimensionless form of the kinetic reaction equations	90
A.2.2	Parameters of the model	92
A.3	Parameters for the model of osteogenesis (Chapter 6)	93
Appendix B	List of publications	96
References		98

LIST OF FIGURES

2.1	Detail of a screw-type dental implant	7
2.2	Osteoinduction, osteoconduction, osteogenesis and osseointegration	9
2.3	Biological stages of healing at the bone-dental implant interface	10
2.4	Mechanical phenomena at the bone-dental implant interface	11
2.5	Schematic of the bioelectric model	15
3.1	Reference element in 1D	22
3.2	Reference element in 2D	23
3.3	Schnakenberg model in 1D. Chemical activator.	27
3.4	Schnakenberg model in 1D. Chemical inhibitor.	27
3.5	Schnakenberg model in 2D. Chemical activator.	28
3.6	Glycolysis model in 2D. Glucose concentration.	29
3.7	Glycolysis model in 2D. Pyruvate concentration.	29
3.8	Glycolysis model in 2D. Spot-like patterns.	30
3.9	Glycolysis model in 2D. Stripe-like patterns.	30
3.10	Chemotaxis model in 2D. Cell density	32
3.11	Chemotaxis model in 2D. Chemical concentration	32
3.12	Glycolysis-chemotaxis coupling model.	33
4.1	Mesh, initial and boundary conditions	40
4.2	Osteogenic cell migration with different EF strengths	42
4.3	Osteogenic cells colonization with different EF strengths	43
4.4	Osteogenic cells migration, only chemical stimulus	43
4.5	Numerical relations for cell migration directed by an external electric field	44
4.6	Osteogenic cell migration when the applied electric field changes direction	45
4.7	Osteogenic cell migration, chemical stimulus in opposite direction	46
4.8	Numerical relations for cell migration directed by an electric field with an opposite-side chemical stimulus	47
4.9	Osteogenic cell migration with low EF strengths and the chemical stimulus in opposite direction	48
4.10	Osteogenic cell migration with the chemical stimulus in the same direction	49

LIST OF FIGURES

4.11	Numerical relations for cell migration directed by an electric field with a equal-sided chemical stimulus	50
4.12	Osteogenic cell colonization with different EF strengths and the chemical stimulus in the same direction	51
4.13	Osteogenic cell migration under a constant flux of osteogenic chemical	52
5.1	The bone-dental implant interface, simulation domain and mesh	61
5.2	Fibrin network formation when no EF is applied	64
5.3	Fibrin formation after 10 minutes of exposure to different EF strengths	65
5.4	Fibrin formation when exposed to different EF strengths	66
6.1	Interface, simulation domain and connections for electrostimulation	73
6.2	Fibrin formation after 10 minutes of exposure to different EF strengths	76
6.3	Osteogenic cells density profile 5 days after injury	77
6.4	Osteogenic cell density and osteogenic chemical concentration 7 days after injury	78
6.5	Granulation tissue formation	80
6.6	Displacement of the fibrillar matrix	81
6.7	Bone formation 14 days and 21 days after injury	83

1.1 Background

Based on initial researches made in the 1800's, it is recognized that biological tissues and specially bone have a characteristic electrical behavior [1]. In the presence of a compression load, the electrical response of bone is an electronegative potential that in turn stimulates new bone deposition. In contrast, when tension is applied an electronegative potential appears inducing resorption of bone matrix [2]. The control of this osteogenic behavior by applying an external electric field is the base of the electrostimulation and many electrotherapy techniques [3].

The biological effects of electrostimulation are more a consequence of the intensity of the stimulus rather than its frequency [2]. It also has been found that the effects of static stimulus may last for hours, days and even weeks, and therefore, they may influence long-lasting biological processes such as growth development and wound healing [1]. These findings support the preferential use of static electrical fields and its related biological influence [4].

In general terms, it has been established that cells in an external electric field tend to align perpendicular to the field lines [5]. This cell alignment is related to cell adhesion, cell migration and tissue contraction events also observed in vitro during the application of external static electric fields [6]. Cell movement and speed are also biased by the presence of the external electric field. This phenomenon, called *electrotaxis*, has been found to be dependent on the time of the stimulus, the intensity of the applied electric field and the presence of molecular activators like calcium ions [7].

Although the effects of electrostimulation had been observed specially in bone, cartilage, ligament, muscle and skin [5,8], there is no general consensus about the underlying biological (and mechanical) processes influenced by the external electrical stimulus nor the frequency, and intensity of the applied electric field. Furthermore, several studies indicate that magnetic fields may also influence tissue formation [4,6]. However, since biological tissues are almost "insensitive" to magnetic fields, its effects are tend to be less observed and evaluated [4], and again, there is no consensus about the nature of the magnetic stimulus and the underlying biological effects.

Despite the lack of knowledge, experimental evidence is clear in pointing out the influence of electrostimulation in tissue formation, including bone growth [8–11]. As a consequence, it has strong applicability as a therapeutic alternative provided its relatively easy usage and implementation, low cost of treatments and its few secondary effects [8].

Nevertheless the great amount of knowledge obtained from experimental models which explain the biological process of bone formation [12, 13], mathematical models and computational simulations have proven useful in providing additional information about the interaction mechanisms between proteins, cells and tissues during the entire healing process [14, 15]. Nevertheless, although experimental results support the influence of electrostimulation in bone growth [2, 8], to the best of our knowledge, there is no mathematical model aimed at understanding the interaction mechanisms between the EF and bone formation.

Therefore, in this thesis we present the formulation and implementation of a mathematical model dealing with the influence of the electrostimulation in the bone growth process. For application purposes, the bone growth needed for the osseointegration of a dental implant is studied. The results propose remarks about the relation between electrostimulation and bone growth at the bone-dental implant interface, primary issue for a long-lasting osseointegration [16].

This model can be considered part of a relatively new modeling strategy in which biology and mechanics, both already combined in a computational approach known as *computational mechanobiology*, are put together with the electrical response of bone and related tissues, an approach better known as *computational bioelectrics*.

1.2 Scope of the research

Previous researches have established that cell migration can be controlled by an external electric field by inducing electrotaxis [1, 5]. Electrotaxis may cause electrical polarization of the cell, and stimulate the synthesis of signaling molecules needed for cell migration by chemotaxis [1]. In addition, there is a relation between the applied electric field, the cell adhesion mechanism and the orientation profile of cells adhered to a substrate [4]. Studies with electroactive surface materials revealed increments in cell adhesion when using electrostimulation [6]. In consequence, electrostimulation may enhance bone formation possibly by influencing the signaling mechanisms on the osteocyte network [17]. Therefore, it is suitable to establish a relation between an external electric field, cell migration and bone growth.

For the case of dental implants, it is plausible to consider that a higher rate of cell migration towards the implant surface, with a consequent higher adhesion rate over the implant, is responsible for a faster and better wound healing at the bone-dental implant interface, which ultimately increases bone formation over the implant and the rate of osseointegration. Accordingly, this thesis is aimed at supporting the following propositions:

- Electrostimulation has a role on cell migration at the bone-dental implant interface and on the implant osteoinduction.
- Cell migration at the bone-dental implant interface is increased by electrostimulation due to electrotaxis. This phenomenon increases the number of osteogenic cells at the bone-dental implant interface, a process referred here as *electro-osteoconduction*.
- Higher rates of cells and molecules adhesion at the bone-dental implant interface are obtained by using electrostimulation.

- Cell contractile forces at the bone-dental implant interface can be reduced or better supported by using electrostimulation, thus improving the osseointegration of the implant.
- Electrostimulation improves bone growth at the bone-dental implant interface, increasing the rate of osseointegration and reducing the healing time.

1.3 Objectives of the research

1.3.1 General objective

To formulate, implement and validate a mechanobiological mathematical model of the influence of electrostimulation in the bone growth over a dental implant.

1.3.2 Specific objectives

- To determinate the influence of electrostimulation in the mechanobiological process of wound healing and bone growth at the bone-dental implant interface, and in the osteoinductive and osteoconductive properties of the implant surface.
- To formulate a mathematical model of bone growth over a dental implant considering the most relevant biological factors and the influence of the electrostimulation on them.
- To implement the mathematical model using a self-programmed finite elements method (FEM) subroutine and an available FEM software.
- To validate the numerical results in a qualitative and quantitative approach by using previously reported experimental data.

1.4 Outline of this thesis

This thesis is divided into seven chapters. **Chapter 1** corresponds to this introduction. **Chapter 2** is dedicated to present dental implants as part of a prosthetic unit aimed at replacing a missing tooth. The idea of osseointegration is also considered in **Chapter 2**, together with some considerations about the implant surface that foster an adequate bone formation. At this point, the biological process of wound healing of the implant insertion site or bone-dental implant interface is reviewed. Finally, the most important biological, mechanical and electrical elements needed to obtain a successful osseointegration are synthesized in an schematic model, base for the mathematical models presented in the following chapters.

Prior to that, **Chapter 3** reviews the modeling of biological systems and identifies three mathematical models widely used in the literature to represent biologically-inspired behaviors. These models are numerically implemented using the Finite Elements Method (FEM), the numerical method used in the rest of this thesis, for which the generalities are given. Using FEM, the chosen biological models are numerically solved and the results are discussed in terms on the distribution of spatial-temporal patterns suitable to describe features observed during the process of wound healing and bone formation at the bone-dental implant interface.

Electrotaxis causes cell migration parallel to the electric field vector. It is known that the electrical stimulus leading to electrotaxis is an overriding signal for other guidance cues directing cell migration and that this cell migration is directed towards a preferential electrode depending of the type of cells exposed. Therefore, the aim of **Chapter 4** is to introduce a mathematical model for electrotaxis in osteogenic cells. This model is implemented using FEM as described in **Chapter 2**, using as domain an ideal 1-mm square Petri dish resembling an osteoblasts-like cell culture. Results show the existence of numerical relations allowing the quantification of the osteogenic cell migration speed when exposed to different EF strengths and also to a chemical stimulus. Quantification of the cell colonization is also obtained. The spatial-temporal patterns obtained after simulation are comparable with those found during experimental electrotaxis, showing also that the EF is an overriding signal over chemotaxis. Furthermore, results show that the colonization of the preferential electrode by the osteogenic cells depends on the EF strength. Accordingly, the term *electro-osteoconduction* is introduced. Numerical results compare favorably with experimental reports. Therefore, the model is suitable to be used to describe tissue formation during wound healing in the presence of electrostimulation.

As detailed in **Chapter 2**, the healing of the tissues damaged during the insertion of a dental implant is performed by a sequence of biological events leading to the osseointegration of the implant. The first part of this sequence is blood loss detention, and the transformation of the poured blood into a fibrillar network made of fibrin, a process called blood clotting. The latter can be simplified into the kinetic reaction between thrombin and fibrinogen that precedes the conversion of fibrinogen into fibrin. Based on experimental observations of the electrical properties of these molecules, **Chapter 5** presents a hypothesis for the control mechanism created by the presence of an static electrical stimulus in the formation of the blood clot. Accordingly, the electrical stimulus increases the fibrillar network formation in such a way that a preferential region of higher fibrin density can be obtained. This idea is validated by means of a numerical model for the blood clot formation at the bone-dental implant interface. Results compare favorably to experimental observations for blood clotting with and without the application of the static electrical stimulus. From the results is observed that the density of the fibrillar network depends on the strength of the static electrical stimulus, and that the blood clot formation has a preferential direction of formation in the presence of the electrical signal. These findings are the biological basis for the formation of viable electrostimulated tissues during the subsequent biological events leading to bone formation at the bone-dental implant interface.

As commented in this introduction, electrostimulation denotes the influence of a static electric field on cell behavior and tissue formation. Several electrostimulation techniques have been reported to yield both increased rates of tissue recovery and reduced healing times in wounds. Therefore, and considering the results of the models presented in **Chapters 3 - 5**, **Chapter 6** introduces a mathematical model for electrically stimulated osteogenesis at the bone-dental implant interface. The model describes the influence of the electric field in the most critical biological processes leading to bone formation at the bone-dental implant interface, as outline in **Chapter 2**. The numerical solution is able to reproduce the distribution of spatial-temporal patterns describing the influence of electrostimulation during blood clotting, osteogenic cell migration, granulation tissue formation, displacements of the fibrillar matrix, and formation of new bone. In addition, the model describes the electrically mediated cell behavior and tissue formation which lead to an increased osteogenesis in both smooth and rough implant surfaces.

Finally, **Chapter 7** summarizes some intrinsic simplifications made during the modeling process that can be addressed as future work to obtain more accurate predictions. These simplifications are presented in the form of perspectives. Since numerical results obtained using the numerical framework presented in this thesis compare favorably with experimental evidence, final conclusion remarks also commented in **Chapter 7** are intended to present the approach as the basis for a prediction tool suitable to describe the outcome of electrostimulation in clinical scenarios dealing with different types of cells, tissues and wounds.

2.1 Introduction

A dental implant is a biomaterial device inserted in the jaw bone to replace a missing tooth. After placement, biological tissue recovery events create a firm, stable and long lasting connection between the bone and the implant, a process called *osseointegration* [16, 18, 19]. An adequate osseointegration is conditioned to the acceptance of the implant by the living tissues as well as to the formation of viable bone over the implant surface [16, 20]. The healing at the connection zone or *bone-dental implant interface* depends on biological and patient-related factors [16, 18], the implant design and surface [21–23], the load distribution between bone and implant [23, 24], the surgical procedure used for the implant placement [20, 25], and more recently studied, the electrical properties of biological tissues [4, 8].

Although the healing process at the bone-implant interface is deeply discussed in the experimental literature, in recent years mathematical models have gain insight for their capacity of reproduce biological behavior, also regarding the wound healing process at the bone-dental implant interface. Accordingly, some models describe the biological events leading to bone healing [14, 26, 27], and others describe both the mechanical loading environment and the implant surface interactions under the assumption of partially or even fully osseointegrated interfaces [15, 28, 29].

This chapter provides a review of dental implants, the formation of the bone-dental implant interface, the process of bone formation leading to osseointegration and previous numerical strategies aimed at modeling the bone growth needed for to gain successful osseointegration of a dental implant. In addition, the most prominent effects of electrostimulation in bone are presented. The discussion is supported on a literature review of experimental evidence that provides the guidelines for the mathematical modeling of the osseointegration of a dental implant, taking into account biological, mechanical and electrical factors. Finally, the scope, hypothesis and objectives of the research conducted in this thesis to formulate and implement a new complementary numerical approach are presented.

2.2 The bone-dental implant interface

Teeth are anatomic structures used during chewing. Each tooth has a crown, a neck and a root [30,31]. The crown is the visible part inside the mouth and the root lies inside the jaw bone. The neck is the boundary between the crown and the root [30]. Teeth grow inside the *dental alveoli*, a socket-like bone formation placed within the *alveolar bone*, the bone ridge covering the jaw bone.

A dental implant is a biomaterial device surgically inserted in the jaw bone to replace the root of a missing tooth [19,32]. The implant is part of the prosthetic unit that replaces the missing tooth and is formed by the abutment, the joint and the prosthesis that replaces the missing crown (Fig. 2.1).

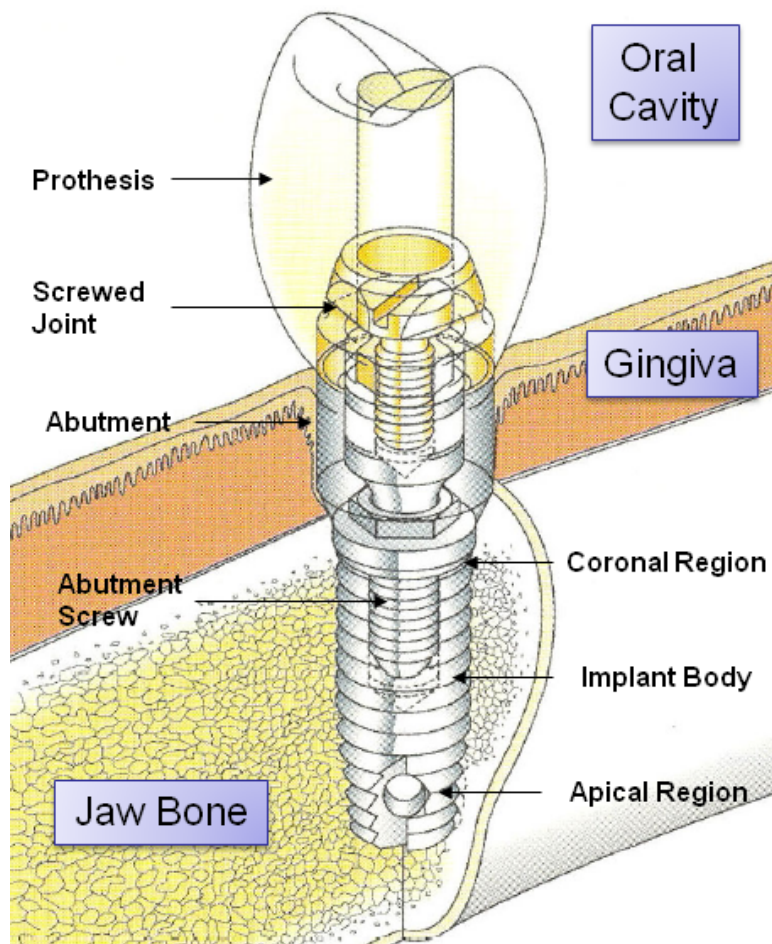


Figure 2.1: Detail of a screw-type dental implant. Adapted from [33].

The majority of available dental implants are made of commercially pure titanium [34], given its proven biocompatibility or acceptance by the living tissues [21,35]. The biocompatibility comprises the absence of corrosion and material wearing that may lead to undesirable inflammatory responses, death of surrounding tissues or thrombus formations by unexpected coagulation effects. It also implies that the living organism is not producing undesirable immunological responses such as increased antibody counting, cell mutations or formation of

cancer cells [19, 33, 35].

There are several types of dental implants, being the most recognized those with roughed and screwed body, and with dimensions ranging from 6.0 mm to 16.0 mm length and 3.5 mm to 5.0 mm diameter, depending on the nature of tooth to be replaced [20, 23]. However, the optimal length and diameter needed for a successful long-lasting implantation depends on the anchorage conditions of the host bone, and the biological and mechanical factors associated to bone healing [12, 13, 23, 24, 36, 37]. Therefore, nowadays there are available in the market different geometries of dental implants, being the screw-type geometry introduced in the 1960s by PI Branemark the most recognized [38]. This type of implant shows high mechanical retention provided by its canaled body, has and outstanding ability in transferring compressive forces, and provides adequate retention after insertion in the jaw bone, a process called as primary stability [23, 39].

Although the surface macro-topography of the implant, related to the screw-like geometry and the canaled body, is relevant for the implant stability and stresses (forces) distribution, the microtopography, described as the surface irregularities present on several commercial implants, provide the implant with additional properties that improve their capability to interact with the physiological environment [21, 33]. These surface irregularities are the results of exposing the implant to different chemical and mechanical processes aimed at modify the implant surface, creating a surface pattern similar to that left behind by the osteoclast resorption front during bone remodeling [21, 39, 40]. Such a pattern allows the secretion products released by the osteoblastic cells to interlace with the implant, ensuring bone formation directly over the implant surface by fostering and improving cell adhesion and tissue attachment [41].

Besides the implant characteristics, the insertion procedure has been shown to be of importance in the success of the prosthetic unit. The presence of a large number of bacteria inside the mouth demands the injury caused during implant placement to be carefully preserved in order to avoid possible infections leading to implant loosening. According to this, the most referenced insertion technique includes the implant coverage with the epithelial tissue originally present at the insertion site [20, 23, 25, 30, 38, 42]. The use of this technique reduces the wound healing time by the temporally isolation of the implant from an environment rich in microorganism such as the oral cavity, that ultimately increases the bone formation at the implant surface by reducing the bacterial contamination risk [19, 20, 23]. Despite this advantage, this technique, also known as the *two-stages* intervention, requires two surgical interventions to complete the prosthesis placement [38]. During the first intervention, the implant is inserted in jaw bone and covered by the epithelial tissue. About 4 to 6 week later, a second intervention is carried out to remove the epithelium cover, expose the cortical side of the implant and attach the abutment and the prosthesis [25]. The better primary stability and primary healing of the bone-dental interface obtained using this technique is traded-off by the higher trauma caused to the patient and the delay in completing the final dental restoration [25].

However, there is another type of insertion technique in which the implant, the abutment and the prosthesis are placed at the same time during a single surgical intervention. This technique, known as *single-stage* intervention, avoids the epithelium coverage, reduces the healing time and increases the patient benefit [43]. Nevertheless, and as can be expected, this technique reports higher bacterial contamination problems present during wound healing, and is less used in practice because it increases the chance of scar tissue formation (loosening of the implant) due to the micromovements induced during the early loading of the prosthesis and the implant underneath [23, 43].

2.3 Osseointegration

Although the evaluation of the anatomic characteristics of the host bone, the selection of the implant and the use of an adequate insertion protocol are all conditions related to the healing of the bone-dental implant interface, the implant osseointegration is, however, more dependent on the bone formation directly over the implant surface [16, 20]. A successful osseointegration requires the action of two phenomena: *osteinduction* and *osteoconduction* [16]. Osteoinduction is the process by which stem cells are somehow stimulated to differentiate at the bone-dental implant interface into osteogenic cells which synthesize bone tissue (Fig. 2.2a). New bone deposition by these cells is known as *osteogenesis* (Fig. 2.2b) [16]. There are two kinds of osteogenesis. A first called *distant osteogenesis* during which bone tissue is initially deposited at the host bone and grows towards the implant surface [36], and a second called *contact osteogenesis* during which bone tissue formation is carried out from the implant surface towards the host bone (Fig. 2.2b) [36, 44].

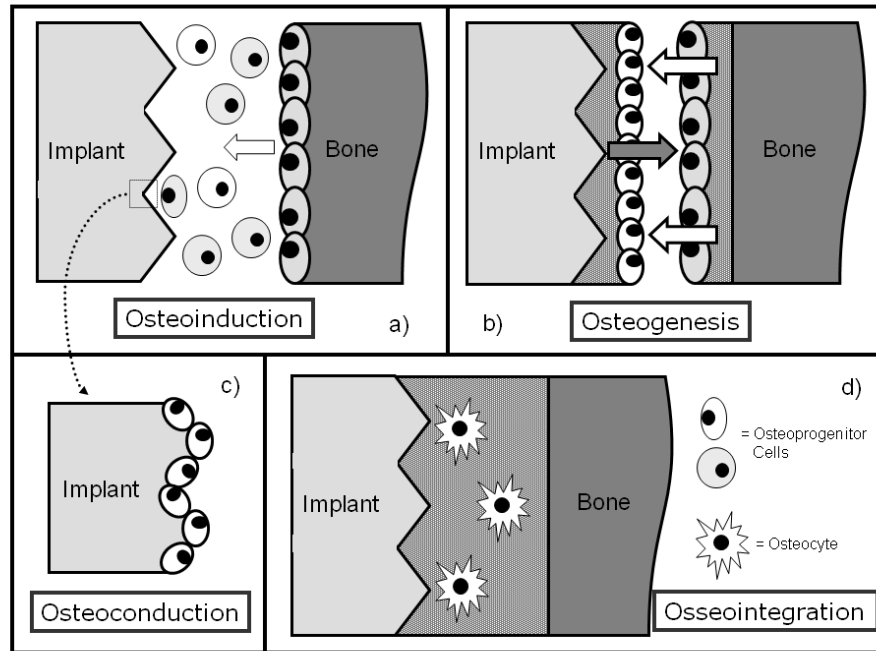


Figure 2.2: Schematic representation of the processes of osteoinduction, osteoconduction, osteogenesis and osseointegration. See text for details.

There are two kinds of osteogenesis. A first called *distant osteogenesis* during which bone tissue is initially deposited at the host bone and grows towards the implant surface [36], and a second called *contact osteogenesis* during which bone tissue formation is carried out from the implant surface towards the host bone (Fig. 2.2b) [36, 44]. Contact osteogenesis implies that the implant surface is being colonized by the osteogenic cells [36]. This cell colonization, or osteoconduction, allows bone to grow a biomaterial surface (Fig. 2.2c) [16, 36]. This process depends on the material biocompatibility and the implant surface characteristics [45, 46]. More specifically, osteoconduction creates a direct contact between the implant and the surrounding

growing tissues. This biomaterial-tissue contact set the pathway for the wound healing process to be successfully conducted, leading ultimately to the implant osseointegration (Fig. 2.2d).

2.4 Mechanobiology of the bone-dental implant interface

Healing at the bone-dental implant interface can be summarized into four biological stages, each one associated with a characteristic biological event [12, 31] (Fig. 2.3), namely: 1) Hematoma formation (bleeding and blood clotting), 2) clot degradation and wound cleansing (fibrinolysis), 3) granulation tissue (fibroplasia and angiogenesis) formation, and 4) new osteoid formation (bone modeling).

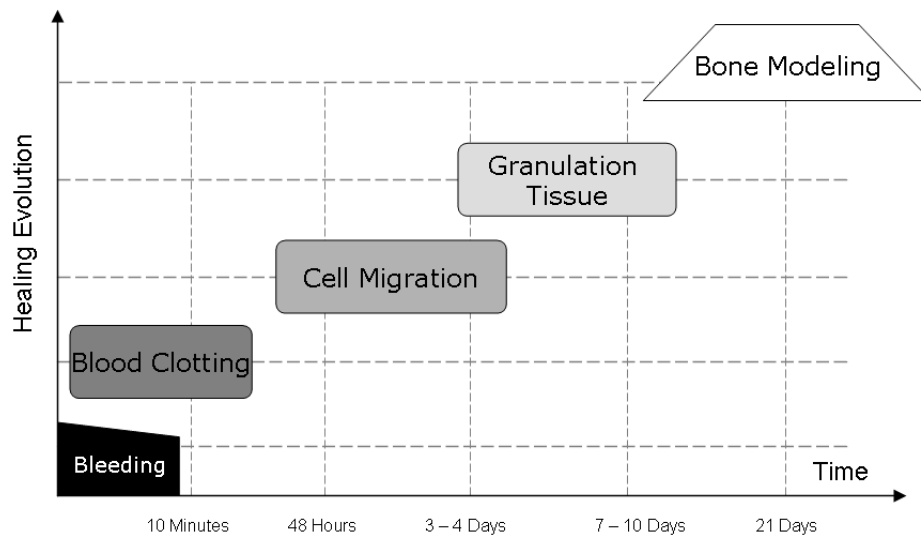


Figure 2.3: Biological stages of healing at the bone-dental implant interface [15, 31, 47].

Biological wound healing events are activated with the bleeding caused during the surgical procedure of implant placement [25, 43]. After bleeding, the injured blood vessels constrict and the platelets from the bloodstream are activated to form a plug which temporarily stops the blood loss [48, 49]. The temporary plug is then replaced by a haemostatic plug formed by the reaction kinetics between two blood proteins, specifically, thrombin and fibrinogen [48, 50]. Thrombin converts fibrinogen into *fibrin fibers* [48, 50]. These fibers accumulate to form the *fibrin clot*, which completely detains the blood pouring about 10 minutes after the injury [51]. This fibrin clot also protects the tissue left exposed after implantation [12, 49]. Then, a cleaning activity, carried out mainly by macrophages and neutrophils, starts the degradation of some of the fibrin fibers to create paths for the migration of the *osteogenic cells* [31, 36].

Around the fourth day after injury, *fibroplasia*, the replacement of the fibrin clot with a new extracellular matrix known as *granulation tissue*, is started. This new matrix, mainly composed of collagen and new capillaries [12], provides mechanical and nutritional support for the migration of the osteogenic cells [31]. Cell migration is stimulated by several molecules released during blood clotting and platelet activation, such as the platelet-derived growth factor (PDGF), the transforming growth factor beta (TGF- β) [36] and the fibroblast growth factor (FGF) [47]. Between the seventh and the tenth day of healing, some of the fibroblasts

present in the interface are transformed into *myoblasts* [13]. These cells have cytoplasmatic microfilaments of α -actin of *smooth muscle* that allows them to generate the contractile forces which contract the tissues under formation [12, 13, 36].

This contraction also appears when fibroblasts and osteogenic cells adhere to the fibrillar network and begin to move through it in an attempt to colonize the implant surface [36]. Accordingly, cell migration causes displacement of the attached fibers, which eventually might be separated from the implant surface [36, 41]. Such a separation prevents the cells from reaching the implant surface, thus reducing tissue formation directly over the implant surface, and increasing the risk of implant loosening [20].

Around fourteen days after injury, osteogenesis initiates the bone formation along the vascular structures [31]. During osteogenesis, the granulation tissue is replaced by new collagen fibers which are slowly mineralized to create the new bone matrix [24]. In the case of dental implants, osteogenesis may be initiated either as *direct osteogenesis* or as *contact osteogenesis* [36]. During direct osteogenesis, the new bone is deposited from the host bone surface and towards the implant surface. In contrast, during contact osteogenesis bone deposition is started at the implant surface and evolves towards the host bone. Although contact osteogenesis increases the rate of bone formation at the interface [36], the clinically accepted osseointegration rate of 80% is usually reached about 3-4 months after implant placement [20, 36]. During this time lapse, bone modelling and remodelling processes work together to fully restore the biomechanical integrity of the new bone and to consolidate the anchorage of the dental implant [24].

Although the biological activity of wound healing concludes with the modeling and subsequent bone remodeling [24], the process is highly influenced by mechanical action throughout the different stages. Accordingly, biological processes such as cell adhesion, cell migration, together with external loading, modify the new tissue formation profile, as depicted in Fig. 2.4.

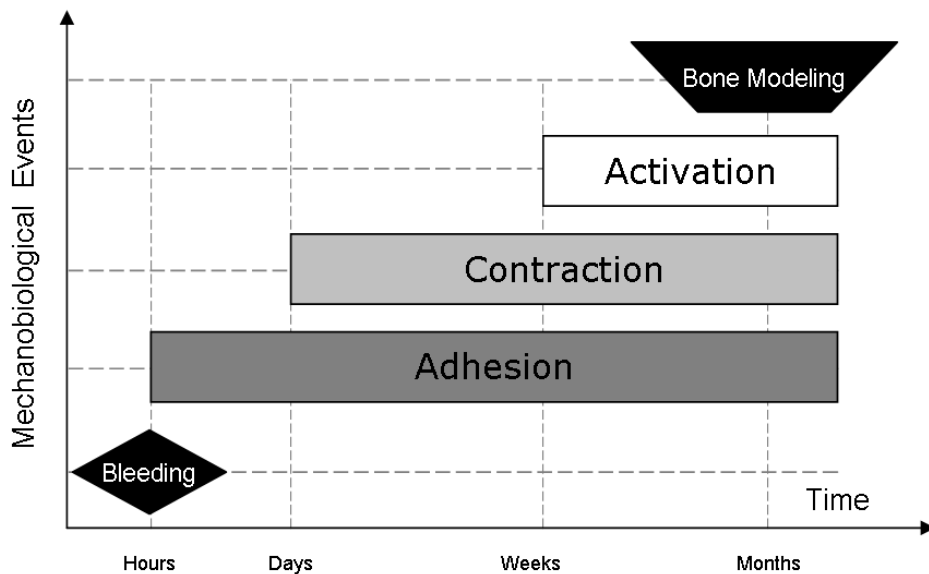


Figure 2.4: Mechanical phenomena occurring during the healing of the bone-dental implant interface.

The mechanical action interacts as follows. First, the adhesion forces produced by cells attached to a substrate [52] activate chemical signaling [53], which control cell proliferation and differentiation, as in the case of the platelet aggregation and activation stages [54].

Then, the contraction exerted by cells moving over a substrate [13] causes the displacement of the attached fibrin fibers and their detachment from the implant surface [36,41]. This kind of event is present during fibroplasia and modeling stages where fibroblasts and osteogenic cells adhere to the fibrin network and begin to move through it in an attempt to colonize the implant surface. Fibers detachment prevents suitable bone formation directly over the implant surface and lead in consequence to an increased risk of implant rejection [20,32].

Finally, the mechanical activation caused by the application of an external load induces the metabolic activity necessary to produce structural changes in the extracellular matrix of the tissues under formation [24,37]. A phenomenon of this kind is particularly relevant during *bone mechanotransduction* [55,56], which is responsible for controlling functional adaptation to external loads during tissue formation. The mechanical adaptation to this external action, a bone property, is described by the *Wolf's Law* [24,40].

2.5 Electrostimulation and bone growth

The four stages leading to bone formation at the dental-implant interface are all influenced by the EF. It has been found that platelets and fibrinogen, among many other molecules present during blood clotting, tend to migrate towards the positive electrode when a potential difference is applied to a blood sample [57]. This behavior is the principle of *electrothrombosis* and of a platelet measurement technique called *electrical aggregometry*. During electrothrombosis, platelets are activated to form a thrombus or blood clot after the application of a static EF [58]. In electrical aggregometry, two platinum electrodes are immersed in a blood plasma sample. Platelets respond to the electrical stimulus by accumulating at the polarized electrodes, making it possible to calculate the number of available cells [58].

In general, cell migration and speed are biased by applied static EFs [5,7,9]. Many different types of cells exposed to static EFs have been found to migrate parallel to the EF lines and towards a preferential electrode in response to electrotaxis [5,6]. Since a static EF induces reorientation of cell surface and signaling molecules such as integrins [4,59], the application of this kind of stimulus appears to be more important for cell migration than chemical and haptotactic signals [6,60]. In fact, it has been reported that an EF overrides other cell migration cues [5], thus playing a significant role during cell recruitment for wound healing and new tissue formation [1].

Furthermore, the use of electrostimulation increases bone formation and bone healing, even in delayed unions and nonunions of long-bone fractures, in which a natural complete healing is no longer expected [3]. Experimental studies conducted on animal protocols and dental implants have shown that electrostimulation increases the rate of wound healing at the bone-dental implant interface [11,61]. Although this increase may in general lead to higher osseointegration rates, it is important to identify the adequate dosimetry of the stimulus in terms of intensity, exposure time, and length of treatment, to fully validate the effect of the electrical stimulus on osseointegration [11,61].

2.6 Modeling osseointegration

Although several biological and mechanical factors converge at the bone-dental implant interface, most of the mathematical models available only consider the mechanical factors, leading to conclusions regarding the long range viability of the implants, the loading distributions and the mechanical behavior of the materials used in the implant manufacturing [29, 62]. In this type of models, the formation of the bone-dental implant interface is not considered and the assumed biological starting point is the complete and stable osseointegration [29].

There are also models approaching to the healing biological phenomena at the interface, describing fibrous tissue formation as the results of mechanical variables [28] or by considering the phenomenological behavior of the mechanics involved [63]. Nevertheless, there are models with a biological framework that base their descriptions on phase changes at the interface [15] and on variations of the cellular concentrations and extracellular matrix density [14, 26]. In this cases, the equations used include specific terms describing cellular processes as mitosis, proliferation, differentiation and apoptosis, as well as natural biological events leading to the formation, transformation and degradation of the extracellular matrix [14, 26, 64].

Mechanobiological approach

A complete mechanobiological model for the formation of the bone-dental implant interface leading to the implant osseointegration is still not know, although several works have succeeded in the attempt of formulating mathematical description that include some of the biological and mechanical events related to the wound healing process. Therefore, there are models dealing with cell adhesion and proliferation [65, 66], blood coagulation [67, 68], angiogenesis and cell contraction [69, 70], and bone formation [14, 27].

Considering the biological and mechanical nature of the wound healing process at the bone-dental implant interface, and the results provided by the above mentioned mathematical models, the following elements are to be included in the formulation of a robust mechanobiological model for the bone-dental implant interface:

1. The biological stages of wound healing at the interface may be assumed as a sequence of events in a time scale divided in minutes, hours, days, weeks and months [12, 15, 47].
2. The bleeding stage may be simplified as the formation of the fibrin clot by the reaction kinetics between thrombin and fibrinogen [12, 48].
3. The fibrinolysis stage may be considered as a natural clot degradation term, whereas the fibroplasia and the angiogenesis can be simplified in a single event leading to synthesis of new collagen matrix [13].
4. The formation and replacement of the collagen matrix by new bone is related to the presence of an specific concentration of osteogenic cells and the presence of a chemoattractant signal controlling cell migration and proliferation [14, 36, 44].
5. The adequate bone formation around the dental implant depends on the surface topography and the formation of the cementation line [41, 53].
6. The adhesion mechanical factors may be considered as part of the cell differentiation process and should be related to the implant surface topography and the implant osteoinduction and osteoconduction properties [41].

7. The contraction and activation mechanical factors are similar at a micro-structural level and therefore may be simplified as the viscoelastic behavior of the fibrillar fibrin matrix that compounds the blood clot [71] and guides the subsequent bone formation process [40,72].
8. The loading effects over the implant may be neglected if the recommended initial healing time of three to six months prior to prosthesis placement is considered [20,73].
9. The surface irregularities of the dental implant influence the cell and proliferation profiles, as is shown through experimental assays [36,41].

Furthermore, considering the experimental results on electrostimulation and the reported influence of EF on both cell dynamics and tissue formation [5, 6], specially bone [3, 61], the following elements are to be included in the formulation of a bioelectric model of the osseointegration of a dental implant:

1. Since thrombin and fibrinogen have a net electrical charge, the presence of an external electric field induce an electric force in these molecules that guides their accumulation towards a preferential electrode [57].
2. The adhesion properties of the implant surface can be increased by using electroactive surface treatments [21, 59]. Furthermore, the presence of an electric stimulus induces a surface electric charge that mediates the absorption of biomolecules needed for cell adhesion directly over the implant surface [59].
3. Cell migration is electrically controlled as due to electrotaxis [5]. Therefore, cell migration speed and cell accumulation over the implant surface can be electrically mediated.
4. Electrical stimulation enhances the synthesis of collagen % [60,74] and therefore increases the formation of granulation tissue.
5. The bonding capacity of the tissues under formation is reinforced by influence of the electrical stimulus in both the integrins and the focal contacts intervening in cell adhesion [4]. Accordingly, the contraction forces exerted during cell migration can be counteracted by an electrical adhesive force that reduces tissue detachment from the implant surface [75].
6. Cell elongation during electrostimulation [5] can be considered as a change in the contact area of the cells when colonizing the implant surface, thus enhancing the adhesion forces and the tissue bonding capacity [9, 59].
7. Electrical stimulation enhances bone growth at the bone-dental implant interface but also directly over the implant surface [11,61]. Therefore, electrical stimulation increases the rate of contact osteogenesis, reducing the time lapse for osseointegration [10,76].

Most of these elements were used for the formulation of a new mathematical model with a bioelectric approach. This model includes the biological stages described in Fig. 2.3, some of the mechanical factors described in Fig. 2.4, the displacement of the new tissues caused by the contraction exerted during cell migration [36], the implant surface irregularities, and the effects of electrostimulation. A schematic of this new model is shown in Fig. 2.5, in which the

sequence of biological stages is shown at the left side, and the aspects considered at each stage are shown at the right side. The right-most boxes summarize the most important aspects used at each event, which also represent the simplifications made to the complex chain of biological and mechanical phenomena leading to the osseointegration of a dental implant.

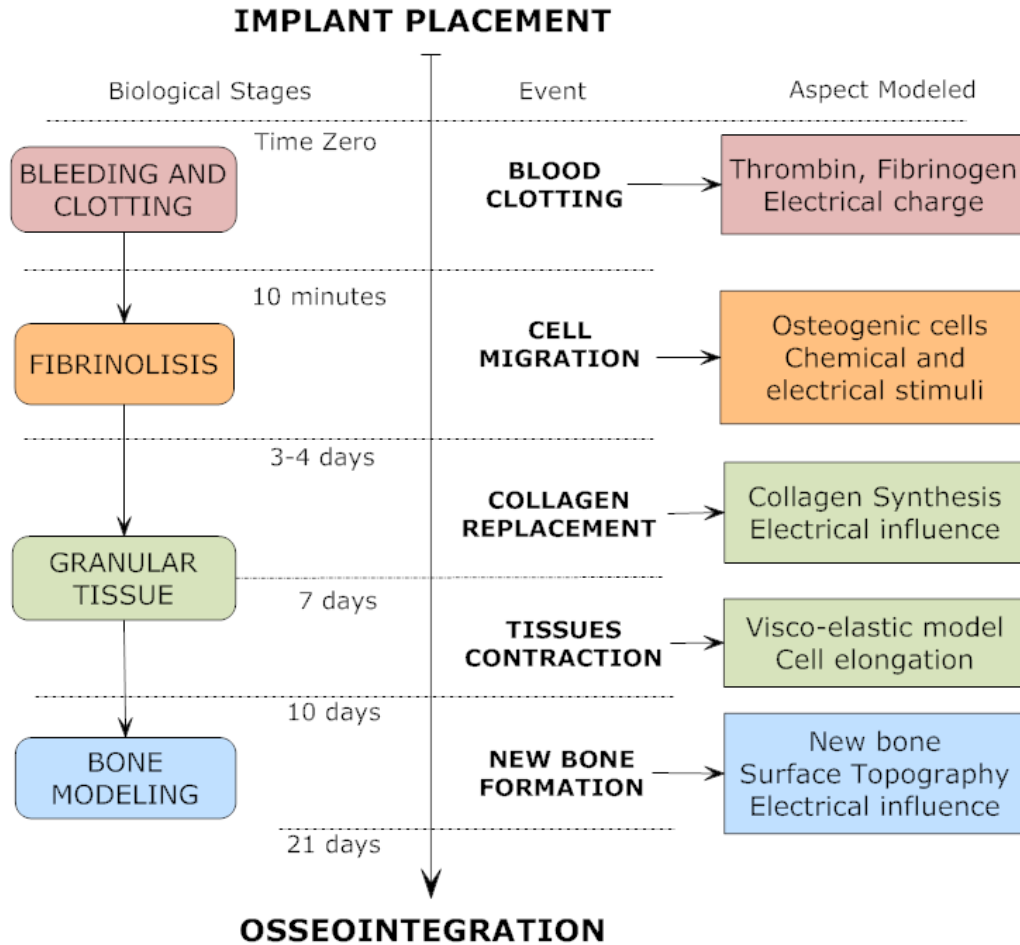


Figure 2.5: Schematic of a mechanobiological model of the osseointegration of a dental implant.

This model simplifies the biological wound healing process as a sequence of stages each one associated to a series of events. In this way, the bleeding and coagulation stage is simplified as the fibrin blood clot formation by the kinetic reaction between thrombin and fibrinogen. During fibroplasia osteogenic cell migration is initiated by the presence of a chemoattractant signal. The new collagen matrix formation by the osteoprogenitor cells simplifies the fibroplasia and angiogenesis processes in a single stage called granular tissue [12]. The displacement of the osteoprogenitor cells over the collagen matrix causes fibrillar contraction conditioned to the viscoelastic response of the fibers and the collagen mechanical properties. This contraction constitutes the interaction between biological and mechanical factors presented in this mechanobiological model. Finally, the new bone formation process, conditioned to the surface topography of the implant included as a numerical parameter and the adequate formation of

the cemented line due to the contact osteogenesis process, leads to the initial osseointegration of the dental implant.

In addition, the influence of electrostimulation at each stage is included as modifying effects. Accordingly, blood clotting is influenced by the electrical charge of both thrombin and fibrinogen, fibroplasia is influenced by electrotaxis, granular tissue formation is enhanced by the increased collagen synthesis, and bone modeling is governed by the joint activity of the chemical and electrical stimuli at the bone-dental implant interface. Further details about the model implementation are introduced in Chapters [5](#) and [6](#).

CHAPTER 3

BIOLOGICAL MODELING AND COMPUTATIONAL IMPLEMENTATION USING THE FINITE ELEMENTS METHOD

3.1 Introduction

Applications of mathematical modeling in developmental biology has motivated the formulation of numerical models that after being solved lead to spatial-temporal patterns [77]. According to the characteristics of the patterns, these models can be classified in two categories, i.e., models of chemical interaction and models of cell movement interaction, with the former subdivided into gradient models and reaction models [78].

Gradient models are mathematical models for chemical substances experiencing differences of concentration that during its temporal evolution tend to a uniform state in space and time [78]. In contrast, reaction models are models for which the chemical interactions between the substances generate complex patterns in space and time, due to the presence of terms representing transport, synthesis and degradation of the substances [78, 79]. On the other hand, cell movement interaction models involve the formation of patterns due to changes in cell density as a consequence of aggregation or repulsion between the cells, or as a response to specific chemicals substances [79].

There are in general two types of solutions to these mathematical models: 1) spatial-temporal patterns and 2) traveling waves [78, 79]. In 1952, Alan Turing [80] showed that a reaction-diffusion model with the appropriate parameters and defined in a closed spatial domain, evolves into a heterogeneous spatial patterns due to small perturbations of the chemical concentrations, a phenomenon known as *diffusion instability* [78, 79, 81]. These also called *Turing instabilities* are characterized by a stable state in time, and an unstable pattern formation in space. Such behaviour is typically observed during morphogenesis and skin pattern formation in animals [78, 79, 82, 83]. In contrast, the traveling wave solution represents, from the physical point of view, processes of transition from one equilibrium to another due to the presence of an external stimulus. These transitions allow the generation of a wave-like pattern that moves from the initial conditions and towards the stimulation agent, as in the case of cells migrating in the presence of a chemical stimulus [79, 84].

Given the nature and scope of these different types of solutions, the different mathematical formulations have been found to be practical in the description of several biological processes mainly because of the possible association of the nature of the numerical solutions (the spatial-temporal patterns and the traveling waves) and biological phenomena (tissue formation, cell migration, growth and healing) [78, 79, 85]. Accordingly, the aim of this chapter is to introduce a basic set of mathematical models with applications in developmental biology to evaluate the nature of the solutions and the performance when using the finite elements method as an alternative implementation method to others previously reported [77–79, 86, 87].

3.2 The reaction-diffusion equation

A diffusion problem can be mathematically described by the motion of the density of a set of species $\mathbf{u}(\mathbf{x}, t)$ (bacteria, cells, chemicals) in any environment [77, 78, 82]. Accordingly, the movement of $\mathbf{u}(\mathbf{x}, t)$ or diffusion, indicates the change in concentration from points of higher concentration to points of lower concentration [86–88]. This principle is known as *Fick's Law* and is expressed as follows [86]:

$$\mathbf{J}(\mathbf{x}, t) = -D\nabla\mathbf{u}(\mathbf{x}, t), \quad (3.1)$$

where \mathbf{J} is the *diffusive flux vector*, and D is the *diffusion coefficient*.

Furthermore, the reaction between two or more substances gives place to an additional reactive function $f(\mathbf{u}, \mathbf{x}, t)$ representing the change in the concentration of the $\mathbf{u}(\mathbf{x}, t)$ substances due to interaction effects such as production, proliferation, consumption degradation, among others [78, 82].

According to the principle of conservation, the rate of change of the amount of mass contained in a volume V must be equal to the sum of both the total flow of mass through the surface S of the volume, and the amount of mass transformed inside the volume by the reactive term. This is mathematically expressed as follows:

$$\frac{\partial}{\partial t} \int_V \mathbf{u}(\mathbf{x}, t) dV = - \int_S (\mathbf{J} \cdot \bar{n}) dS + \int_V f dV, \quad (3.2)$$

where \bar{n} is the normal vector to the surface S . Applying the divergence theorem to the diffusive term, and combining Eq. (3.1) with Eq. (3.2) the following expression is obtained:

$$\frac{\partial}{\partial t} \int_V \mathbf{u}(\mathbf{x}, t) dV = \int_V \nabla \cdot (D\nabla\mathbf{u}(\mathbf{x}, t)) dV + \int_V f dV. \quad (3.3)$$

Eq. (3.3) corresponds to an integral equation defined in the domain $\Omega = V$ with boundary conditions evaluated in the surface $\Gamma = S$. In order to ensure spatial patterns formation due only to the interactions within the contour no external flows are supported and therefore boundary conditions are in all cases equal to zero [81]. Accordingly, and writing Eq. (3.3) in differential form, the following expression is obtained [78]:

$$\underbrace{\frac{\partial\mathbf{u}(\mathbf{x}, t)}{\partial t}}_{\text{Change}} = \underbrace{\nabla \cdot (D\nabla\mathbf{u}(\mathbf{x}, t))}_{\text{Diffusion}} + \underbrace{f(\mathbf{u}, \mathbf{x}, t)}_{\text{Reaction}}. \quad (3.4)$$

Eq. (3.4) is known as the *reaction-diffusion equation* and allows, together with the given boundary conditions, the mathematical description of the spatial and temporal behaviour of the species denoted by $\mathbf{u}(\mathbf{x}, t)$ within the space region Ω [78, 81, 86].

3.3 Biological models

There are different models to obtain a mathematical description of complex phenomena occurring in nature [77, 79, 85–87]. However, for the sake of introduction, only three well-referenced models formulated using reaction diffusion equations will be implemented. The first two models are the Schnakenberg model, or morphogenesis model [77, 78, 86, 87], and the glycolysis model [78, 83, 86], both used to explain the synthesis of glucose into cellular energy. These two models generate spatial-temporal patterns and meet the stability criteria defined by Turing [83]. A third model also constructed on reaction-diffusion equations but presenting a traveling wave-like solution, is the chemotaxis model [82, 86]. This model has been used to illustrate cell movement as a traveling wave-like pattern in response to a given chemical stimulus within the surrounding environment.

3.3.1 Schnakenberg model

The Schnakenberg model describes the behavior of a chemical activator u in the presence of a chemical inhibitor v [77, 78]. It has been used in stability analysis applications and pattern formation [78, 83], allowing the prediction of the interaction mechanisms between molecular chemical systems [78, 87] and morphogenic constructions such as bone formation and growth [78, 89]. In its dimensionless form, the model is described by the following equations [78]:

$$\frac{\partial u}{\partial t} = \nabla^2 u + \gamma(a - u + u^2 v) \quad (3.5a)$$

$$\frac{\partial v}{\partial t} = d\nabla^2 v + \gamma(b - u^2 v). \quad (3.5b)$$

In Eq. (3.5), the movement of both the activator and the inhibitor substances is described as a diffusive term with an equivalent diffusion constant given by the coefficient d [78, 86]. The reaction term for the activator substance (Eq. (3.5)a) is described as a constant production given by the parameter a , a linear consumption, and a non-linear kinetic reaction representing the production of the activator u in presence of the inhibitor v . On the other hand, the reaction term for the inhibitor substance (Eq. (3.5)b) is given as a constant production with coefficient b and a non-linear kinetic reaction for the consumption of the inhibitor substance in the presence of the activator. Constant γ is a positive dimensionless constant [78].

3.3.2 Glycolysis model

Glycolysis is the process for the synthesis of the glucose molecule that provides energy to a cell. After a sequence of reactions, glucose is converted into pyruvate and ATP, the latter being a metabolic exchange unit for the living organism [86]. This conversion process is mathematically described (in a dimensionless form) by the following equations [78, 86]:

$$\frac{\partial u}{\partial t} = D_u \nabla^2 u + \delta - ku - u^2 v \quad (3.6a)$$

$$\frac{\partial v}{\partial t} = D_v \nabla^2 v + ku + uv^2 - v. \quad (3.6b)$$

In Eq. (3.6), u is the glucose concentration and v is the pyruvate. The biological interpretation is similar to the Schnakenber model, following a diffusion mechanism for the two substances that are regulated by the diffusion coefficients D_u and D_v . The reaction term for the glucose concentration (Eq. (3.6)a) is given as constant production δ , a linear consumption with coefficient k , and a non-linear consumption. Similarly, the reaction term for the pyruvate (Eq. (3.6)b) is given as a linear production with coefficient k , a non-linear activation, and a linear consumption.

3.3.3 Chemotaxis model

Chemotaxis is referred to the cell migration directed towards the gradient of concentration of certain external chemical stimulus in the cellular environment called *chemoattractant* [82, 86]. A model of this phenomenon describes cell movement as a travelling wave controlled in speed by the concentration of the chemoattractant [86]. Since this kind of cell movement can be concomitant with other cellular processes such as cell division (mitosis) and cell death, a complete model for the cell dynamic is described by the following equations [86]:

$$\frac{\partial u}{\partial t} = \nabla \cdot [D_u \nabla u - \alpha u \nabla v] + rf(v)u \left[1 - \frac{u}{u_0} \right] - \delta_u u \quad (3.7a)$$

$$\frac{\partial v}{\partial t} = D_v \nabla^2 v + g(u) - \delta_v v. \quad (3.7b)$$

In Eq. (3.7), n denotes the cell density and u the concentration of the chemoattractant. Cell migration is described by means of the transport due to gradients in cell concentration, given as a diffusion term with diffusion coefficient D_u . Cell attraction to the chemiotractant is controlled by an additional transport term due to the gradient of the chemical concentration, controlled by the cell density and the chemoattractant sensitivity α . The cell density reaction term (Eq. (3.7)a) includes a function $f(v)$ depending on the chemical concentration, and a logistic function with coefficient r and saturation value u_0 for the cell proliferation, together with the cell death controlled by the coefficient δ_u . Finally, the chemoattractant reaction term (Eq. (3.7)b) relies on a production function $g(u)$ controlled by the density of cells, and a linear consumption mechanism with coefficient δ_v representing the cell consumption of chemical during migration and proliferation [86].

3.4 The finite elements method

The finite elements method (FEM) is a numerical method for the solution of partial differential equations. Based on the idea that a whole can be divided into small constitutive parts, the method can be easily implemented for complex geometries in a wide range of applications.

In general terms, the method consist in the transformation of a partial differential equation into a system of linear ordinary equations [78, 90, 91]. Additional techniques must be used in order to reduce integrals and other mathematical operators, but the main assumption for the reduction of the system relies on the so-called *weighted residual method* [92–95].

For this method, let D be a linear differential operation over a function $u(x)$ to obtain as result a function $F(x)$:

$$D(u(x)) = F(x). \quad (3.8)$$

Then, assume that the function $u(x)$ is approximated by the linear combination of a set of *basis functions* $N_i(x)$ and punctual values a_i . Accordingly,

$$u(x) \cong \tilde{u}(x) = \sum_{i=1}^n a_i N_i(x). \quad (3.9)$$

Plugging the approximated form $\tilde{u}(x)$ into Eq. (3.8) leads to a results that approximates $F(x)$. In consequence, an error or *residual* will appear [95]:

$$R(x) = D(\tilde{u}(x)) - F(x) \neq 0. \quad (3.10)$$

Let Ω be a domain divided into a number NE of *elements*, each one defined as a subdomain Ω_e . Given the linearity of the operator D , a local residual $R_e(x)$ will exist at each subdomain. By forcing the local residuals to be zero at the every subdomain, it is possible to obtain a representation of the punctual values a^i for which the approximated representation $\tilde{u}(x)$ equals $u(x)$ [92, 95]. Accordingly,

$$\int_{\Omega_e} R_e(x) W^i(x) dx = 0 \quad i = 1, 2, 3, \dots, n, \quad (3.11)$$

where W^i are a set of *weight functions* equal in number to the set of punctual values a^i . Choosing appropriate weight functions, the problem is reduced to a set of n algebraic equations for the punctual values a^i , which in fact, are unknown values of the original function $u(x)$ in the given subdomain R_e [95]. By taking the sum of the local residuals, it is possible to obtain a global residual R_g and a comprehensive solution of the problem defined in the domain Ω .

In the case of the reaction-diffusion equations used in the biological models, the implementation of the FEM allows the calculation of the variables u and v throughout the domain and at every time step. Using the weight residual method, the equations for the Schnakenberg model (Eq. (3.5)) can be written for a local subdomain Ω_e as follows:

$$\int_{\Omega} \frac{\partial u}{\partial t} W^i d\Omega = \int_{\Omega} D_u \frac{\partial^2 u}{\partial \mathbf{x}^2} W^i d\Omega + \int_{\Omega} (\gamma(a - u + u^2 v)) W^i d\Omega \quad (3.12a)$$

$$\int_{\Omega} \frac{\partial v}{\partial t} W^i d\Omega = \int_{\Omega} D_v \frac{\partial^2 v}{\partial \mathbf{x}^2} W^i d\Omega + \int_{\Omega} (\gamma(b - u^2 v)) W^i d\Omega \quad (3.12b)$$

Using integration by parts in the second order derivative term, and organizing the terms to write the expression in the form of residuals we obtain:

$$\int_{\Omega} \frac{\partial u}{\partial t} W^i d\Omega + \int_{\Omega} D_u \frac{\partial u}{\partial \mathbf{x}} \frac{\partial W^i}{\partial \mathbf{x}} d\Omega - \int_{\Omega} (\gamma(a - u + u^2 v)) W^i d\Omega = 0 \quad (3.13a)$$

$$\int_{\Omega} \frac{\partial v}{\partial t} W^i d\Omega + \int_{\Omega} D_v \frac{\partial v}{\partial \mathbf{x}} \frac{\partial W^i}{\partial \mathbf{x}} d\Omega - \int_{\Omega} (\gamma(b - u^2 v)) W^i d\Omega = 0 \quad (3.13b)$$

where boundary conditions are assumed all equal to zero. The integral expression in Eq.(3.13) are the *weak form* of the partial differential reaction-diffusion equations for the Schnakenberg model [95].

In general terms, variables u and v can be approximated by a linear combination of the basis functions as follows [94]:

$$u(\mathbf{x}) \cong \tilde{u}(\mathbf{x}) = \sum_{i=1}^n u^i N^i(\mathbf{x}) \quad (3.14a)$$

$$v(\mathbf{x}) \cong \tilde{v}(\mathbf{x}) = \sum_{i=1}^n v^i N^i(\mathbf{x}). \quad (3.14b)$$

However, as a first approximation, let Ω to be a one-dimensional domain. Accordingly, Eq. (3.14) can be considered as a linear interpolation with the basis functions being the one-dimensional Lagrangian polynomials [95]. Therefore, for a given one-dimensional subdomain Ω_e (Fig. 3.1a), only two basis functions exist and only two punctual values a^i are unknown (Fig. 3.1b). [92].

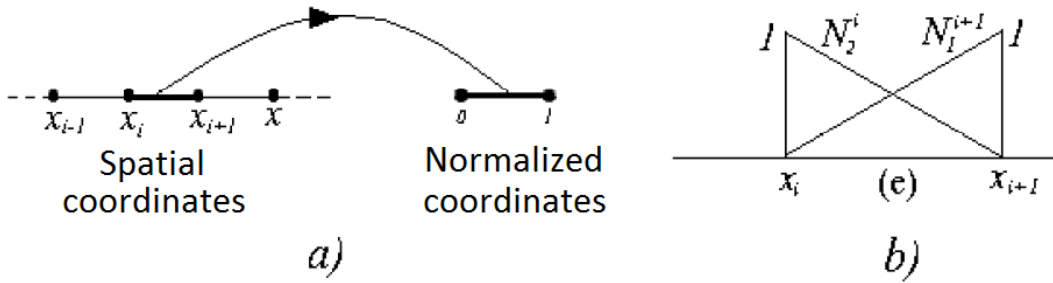


Figure 3.1: a) The one-dimensional reference element. b) One dimensional shape functions.

An additional normalization to these functions lead to a definition in the interval $-1 \leq \xi \leq 1$ with ξ the normalization variable. This process ensures that the basis functions are independent of the nodal coordinates at each element, allowing their use in the rest of the subdomains within Ω . According to the normalization, the one-dimensional basis function or *shape functions* are expressed as follows:

$$N^1(\xi) = \frac{1}{2}(\xi + 1) \quad (3.15a)$$

$$N^2(\xi) = \frac{1}{2}(\xi - 1) \quad (3.15b)$$

Besides of the variable interpolation, a geometrical interpolation should be introduced in order to discretized the one-dimensional domain. Hence, a so-called *isoparametric formulation* [92,94] is adopted. In this formulation, both the variables and the geometry are discretized and interpolated using the same number of punctual values and the normalized shape functions, in such a way that the approximations can be described as follows:

$$\text{Geometry} = \left\{ \begin{array}{l} x = \sum_{i=1}^2 x^i N^i(\xi) = \mathbf{x} \cdot \mathbf{N} \end{array} \right. \quad (3.16)$$

$$(3.17)$$

$$\text{Variables} = \left\{ \begin{array}{l} u = \sum_{i=1}^2 u^i N^i(\xi) = \mathbf{u} \cdot \mathbf{N} \\ v = \sum_{i=1}^2 v^i N^i(\xi) = \mathbf{v} \cdot \mathbf{N} \end{array} \right. \quad (3.18)$$

The extension of this formulation to a bi(tri)-dimensional domain must considered both the description of the shape functions in more than one variable and the geometry of the domain. Accordingly, several types of shape functions can be obtained, being the most recognized those for cuadrilateral (cubic) and triangular (piramidal) elements [94]. For the simplicity of a bi-dimensional implementation, a cuadrilateral element is considered (Fig. 3.2a). For this type of element, the variables u and v can be written again in terms of a linear interpolation with shape functions defined in a bi-dimensional reference frame (Fig. 3.2b). Using Lagrangian polynomials, this new shape functions are written as [94]:

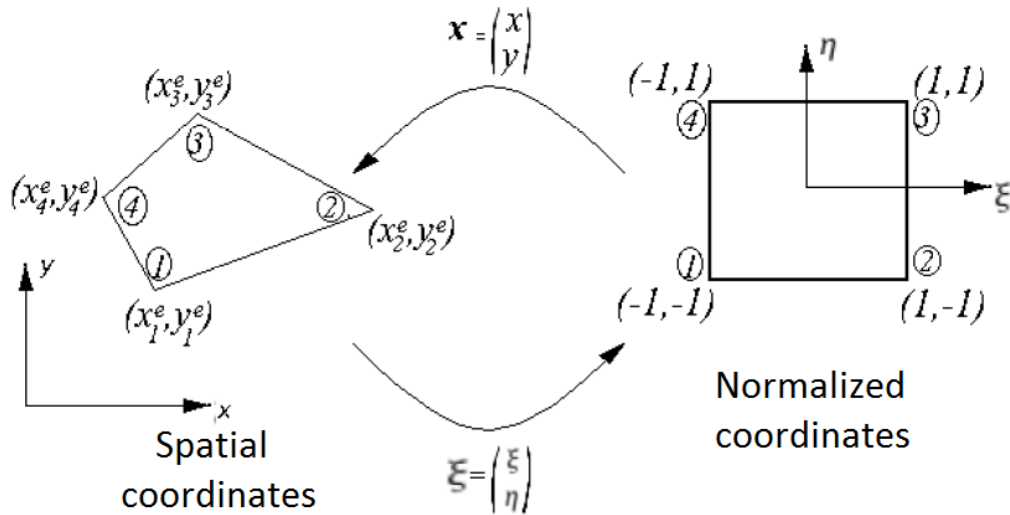


Figure 3.2: The bi-dimensional element defined in the normalized reference coordinates frame. The number of each node is circled.

$$N_1(\xi, \eta) = \frac{1}{4}(1 - \xi)(1 - \eta) \quad (3.19a)$$

$$N_2(\xi, \eta) = \frac{1}{4}(1 + \xi)(1 - \eta) \quad (3.19b)$$

$$N_3(\xi, \eta) = \frac{1}{4}(1 + \xi)(1 + \eta) \quad (3.19c)$$

$$N_4(\xi, \eta) = \frac{1}{4}(1 - \xi)(1 + \eta) \quad (3.19d)$$

In consequence, the geometry and variables approximation is given by:

$$\text{Geometry} = \begin{cases} x(\xi, \eta) = \sum_{i=1}^4 N^i(\xi, \eta)x^i = \mathbf{x} \cdot \mathbf{N} \\ y(\xi, \eta) = \sum_{i=1}^4 N^i(\xi, \eta)y^i = \mathbf{y} \cdot \mathbf{N} \end{cases} \quad (3.20)$$

$$\text{Variables} = \begin{cases} u(\xi, \eta) = \sum_{i=1}^4 N^i(\xi, \eta)u_i^{(e)} = \mathbf{u} \cdot \mathbf{N} \\ v(\xi, \eta) = \sum_{i=1}^4 N^i(\xi, \eta)v_i^{(e)} = \mathbf{v} \cdot \mathbf{N} \end{cases} \quad (3.21)$$

This discretization also implies the transformation of the integral defined in the subdomain Ω_e into an integral defined in the normalized reference frame. Therefore, an additional variable transformation is needed to write the domain differential $d\Omega$ in terms of the normalized frame. This is done by introducing the *jacobian* (\mathbf{J}) of the transformation, which allows writing an integral defined in the spatial coordinates frame into the normalized coordinate frame [94], as follows:

$$\underbrace{\int_{\Omega^{(e)}} f(x, y) d\Omega}_{\text{Spatial coordinates}} = \underbrace{\int_{-1}^1 \int_{-1}^1 f(x(\xi, \eta), y(\xi, \eta)) |\mathbf{J}(\xi, \eta)| d\xi d\eta}_{\text{Normalized coordinates}} \quad (3.22)$$

where $|\mathbf{J}|$ is the determinant of the jacobian given by:

$$\mathbf{J}(\xi, \eta) = \begin{pmatrix} \frac{\partial \xi}{\partial x} & \frac{\partial \xi}{\partial y} \\ \frac{\partial \eta}{\partial x} & \frac{\partial \eta}{\partial y} \end{pmatrix} \quad (3.23)$$

After a complete spatial discretization, an additional discretization should be carried out for the time domain. This is accomplished by using the *Backward Euler method*, according to which the time derivative of a variable u can be written in discrete form as follows [95, 96]:

$$\frac{\partial u}{\partial t} \cong \frac{\Delta u}{\Delta t} \cong \frac{u^i - u^{i-1}}{\Delta t}, \quad (3.24)$$

with u^i the value of u in the current iteration, u^{i-1} the value of u in the last iteration, and Δt the time step.

Therefore, transforming the integration variables by means of the Jacobian (\mathbf{J}), and considering the so-called *Galerkin method* according to which the weighting functions are equal to the shape functions [93,94], the global description in the domain Ω for the Schnakenberg model (Eq. (3.13)) can be discretized and written for a local subdomain Ω_e as follows [90,91,94]:

$$\mathbf{M}^{(e)} \frac{d\mathbf{u}}{dt} - \gamma(a\mathbf{R}^{(e)} - \mathbf{M}^{(e)}\mathbf{u} + v(u^2)\mathbf{R}^{(e)}) + \mathbf{K}^{(e)}\mathbf{u} = 0 \quad (3.25a)$$

$$\mathbf{M}^{(e)} \frac{d\mathbf{v}}{dt} - \gamma(b\mathbf{R}^{(e)} - v(u^2)\mathbf{R}^{(e)}) + \mathbf{K}^{(e)}\mathbf{v} = 0, \quad (3.25b)$$

with the following equivalents for the matrices and vectors:

$$\mathbf{M}^{(e)} = M^{ij} = \int_{\Omega_e} N^i N^j d\Omega_e \quad (3.26a)$$

$$\mathbf{K}^{(e)} = K^{ij} = \int_{\Omega_e} \frac{\partial N^i}{\partial x} \frac{\partial N^j}{\partial x} d\Omega_e \quad (3.26b)$$

$$\mathbf{R}^{(e)} = R^i = \int_{\Omega_e} N^i d\Omega_e \quad (3.26c)$$

Since the integrals in Eq. (3.26) are expressed in normalized coordinates as the right-hand side of Eq. (3.22), it is possible to conduct the integration by applying the *Gaussian quadrature method* [94]. According to this method, the integration of a function in the range $[-1,1]$ can be obtained by a weighted sum of function values calculated at the so-called *Gaussian points*. Using this method, Eq. (3.22) and Eq. (3.26) can be expressed in a complete discrete form similar to the following expression:

$$\int_{-1}^1 \int_{-1}^1 f(x(\xi, \eta), y(\xi, \eta)) |\mathbf{J}(\xi, \eta)| d\xi d\eta = \sum_{i=1}^{GP_x} \sum_{j=1}^{GP_y} f(\xi_i, \eta_j) |\mathbf{J}(\xi_i, \eta_j)| W_i W_j \quad (3.27)$$

where GP_x and GP_y are the number of Gaussian integration points, ξ_i and η_j are the evaluation points for the function $f(x, y)$ written in normalized coordinates, and W_i and W_j are the weight coefficients [94].

The notation shown in Eq. (3.26) and completed by Eq. (3.27) applies to all the subdomains Ω_e within the domain Ω . Therefore, the elemental solutions must be finally *assembled* to account for the complete set of unknown punctual values of the variables u and v throughout Ω . This assembling process leads to the construction of the *stiffness matrix* $\mathbf{AMATRIX}$ and the *right-hand side residual vector* \mathbf{RHS} , needed to obtain the following expression:

$$(\mathbf{AMATRIX})_u \Delta \mathbf{u} = \mathbf{RHS}_u \quad (3.28a)$$

$$(\mathbf{AMATRIX})_v \Delta \mathbf{v} = \mathbf{RHS}_v \quad (3.28b)$$

where $\Delta \mathbf{u} = (\Delta u^1, \Delta u^2)^T$ and $\Delta \mathbf{v} = (\Delta v^1, \Delta v^2)^T$ for the elemental case. This system is similar to the system finally obtained when solving partial differential equations by the *Newton-Raphson method* [95,97]. Using this method to calculate the final solution to the problem, the stiffness matrix $\mathbf{AMATRIX}$ contains the derivatives of the unknown variables, and the

residual vector \mathbf{RHS} is equal to $-\mathcal{F}$. Therefore, it holds true for the elemental case that $\mathbf{RHS}_F = -(F^1, F^2)^T$ and $\mathbf{RHS}_G = -(G^1, G^2)^T$, and that:

$$\mathbf{AMATRIX}_u = \mathbf{M}^{(e)} \frac{1}{\Delta t} - \gamma((-1 + 2uv)\mathbf{M}^{(e)}) + \mathbf{K}^{(e)} \quad (3.29a)$$

$$\mathbf{AMATRIX}_v = \mathbf{M}^{(e)} \frac{1}{\Delta t} - \gamma(-u^2\mathbf{M}^{(e)}) + \mathbf{K}^{(e)} \quad (3.29b)$$

3.5 Numerical implementation

The system of algebraic equations shown in Eq. (3.29) is implemented in an user subroutine written in Fortran and solved using the commercial FEM software Abaqus 6.6 [97]. A similar discretization process as shown with the Schnakenberg model is followed for the implementation of the glycolysis and chemotaxis models, with further implementation details and results as follows:

3.5.1 Schnakenberg model

This model was first implemented in the one-dimensional domain $[0, 1]$. Results are shown in Fig. 3.3 and 3.4. The following parameters were used during the computational implementation: $a = 0.1$, $b = 0.9$, $d = 10$, and $\gamma = 789$ [77, 91]. The initial condition were selected as a perturbation of 5% around the steady-state given by $u_s = 1.0$, $v_s = 0.9$ [83]. The boundary conditions were all zero. Simulation was performed for 1000 iterations with a time step of $\Delta t = 0.005$. The mesh consisted of 300 quadratic patches defined by Lagrangian elements and 601 nodes. The arrows in Fig. 3.3 and 3.4 indicate the direction of movement.

An additional implementation in the bi-dimensional domain $[0,1] \times [0,1]$ allows the formation of spatial temporal patterns as shown in Fig. 3.5. The parameters used in this case were: $a = 0.1$, $b = 0.9$, $d = 9.1676$, and $\gamma = 176.72$ [77, 91]. A total of 1000 iterations were needed, using a time step $\Delta t = 0.05$. The mesh is the same as for the one-dimensional implementation. The initial condition is given by a perturbation of 5% around the steady-state, as shown in Fig. 3.5a. The boundary conditions are in all cases equal to zero.

The results of the model for both the one-dimensional and bi-dimensional implementation show the formation of spatial-temporal patterns around the steady-state (initial condition). The results obtained in 1D show a 180 °C phase shift between the chemical activator concentration and the chemical inhibitor. This shift indicates that the suppression of latter stimulates the synthesis in the former [83, 87]. Since this same shifting behaviour is observed in the two-dimensional implementation, and for the sake of simplicity, the chemical inhibitor concentration is not displayed. Additionally, both implementations show that small perturbations of the steady-state are needed for the formation of spatial-temporal patterns [77, 79, 82]. This is verified by using as initial conditions the exact values of the steady-state for both u and v , condition that results in the inhibition the spatial-temporal pattens. Finally, numerical results obtained using the FEM implementation are in agreement with the results reported elsewhere using other numerical techniques [77, 79, 91].

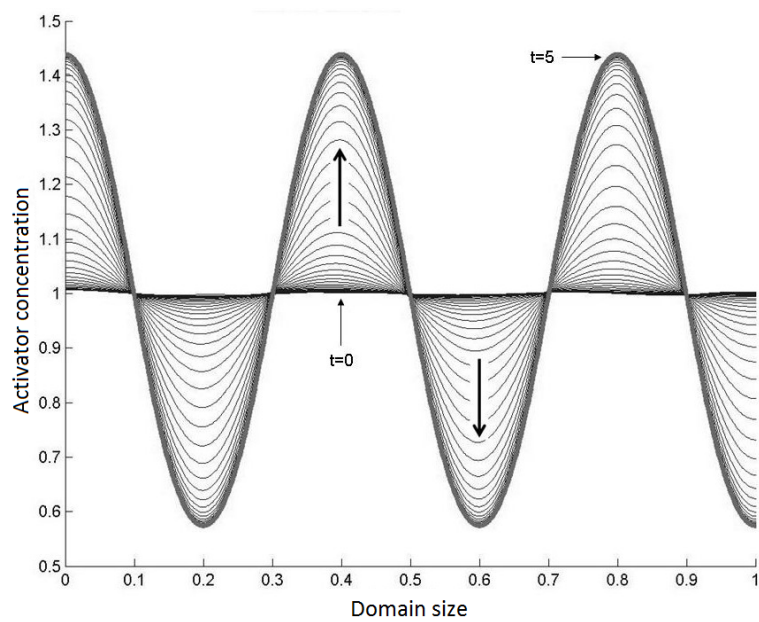


Figure 3.3: Schnakenberg model in 1D. Chemical activator concentration.

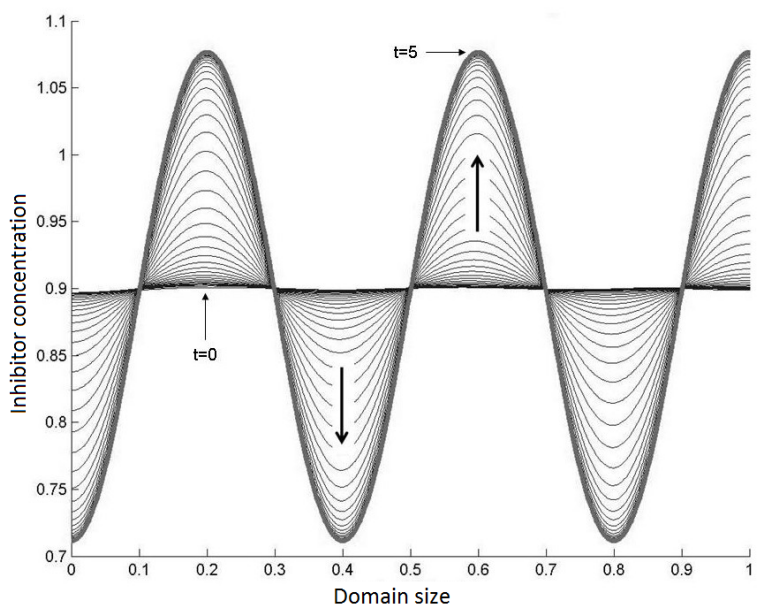


Figure 3.4: Schnakenberg model in 1D. Chemical inhibitor concentration.

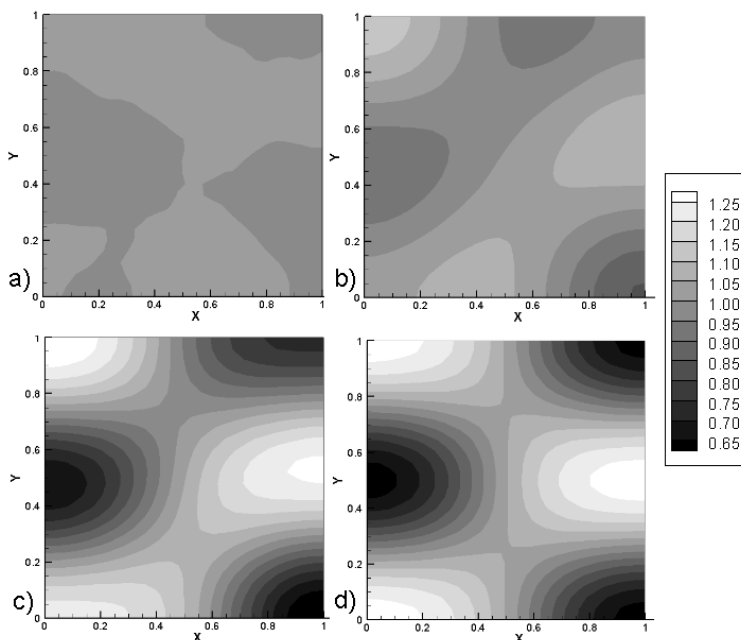


Figure 3.5: Schnakenberg model in 2D. Chemical activator concentration. a) Initial condition, b) $t=1$, c) $t=2$, d) $t=5$.

3.5.2 Glycolysis Model

The model described by equations Eq. (3.6) was implemented for the bi-dimensional domain $[0, \pi] \times [0, \pi]$. Results are shown in Fig. 3.6 and 3.7. Numerical parameters used in this implementation were as follows: $D_u = 1.0$, $D_v = 0.0518$, $\delta = 1.75$, and $k = 0.05$ [77, 86]. The solution was obtained after 25000 iterations with a time step $\Delta t = 0.1$. The mesh consisted of 2500 quadrilateral patches defined by Lagrangian bilinear elements and 2601 nodes. The initial condition is given by a perturbation of 5% around the steady-state $u_s = 0.5622$, $v_s = 1.75$ [83], as shown in Fig. 3.6a and 3.7a. The boundary conditions are in all cases equal to zero.

Results show the formation of spatial-temporal patterns similar to those obtained with the Schnakenberg model in 2D (Fig. 3.5). The presence of the 180°C phase shift between the concentrations of glucose and pyruvate numerical reproduces the production-consumption relationship between the two chemicals. However, the final concentration of glucose after 2500 time units is about the 30% of the final concentration of pyruvate. This difference provides a numerical insight to the greater amount of glucose that is produced when compared to pyruvate production [78].

A second bi-dimensional implementation was performed using the domain $[0, 5\pi] \times [0, 5\pi]$. By keeping the same numerical parameter, meshing, initial conditions and boundary conditions as before, the model lead to the dot-like spatial-temporal patterns shown in Fig. 3.8. The magnitude of this spot-like patterns is similar to the magnitude obtained in the previous implementation (Fig. 3.6). This fact might suggest that the reaction kinetics needed for the formation of the spot-like patterns is slightly increased with respect to the previously implemented case by changing the length of the square domain.

A final implementation of this model was performed within the bi-dimensional domain

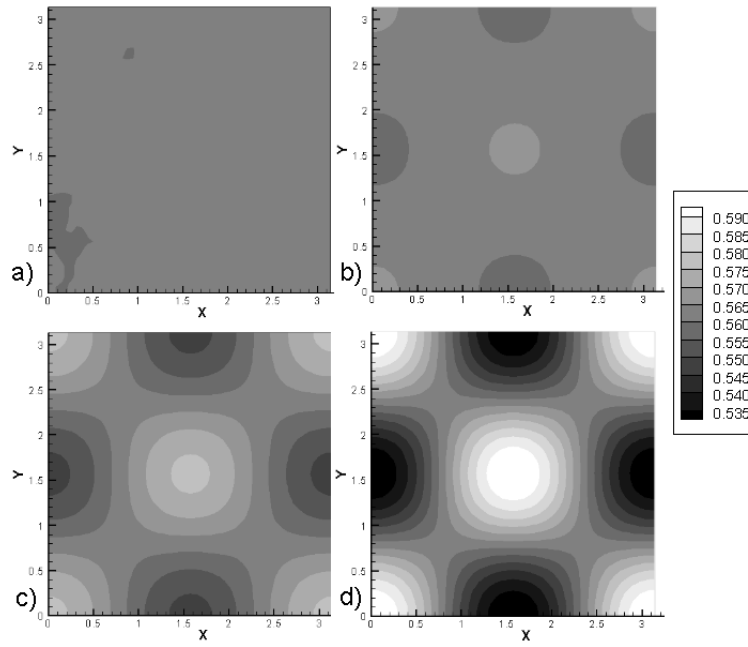


Figure 3.6: Glycolysis model in 2D. Glucose concentration. a) Initial condition, b) $t = 750$, c) $t = 1500$, d) $t = 2500$.

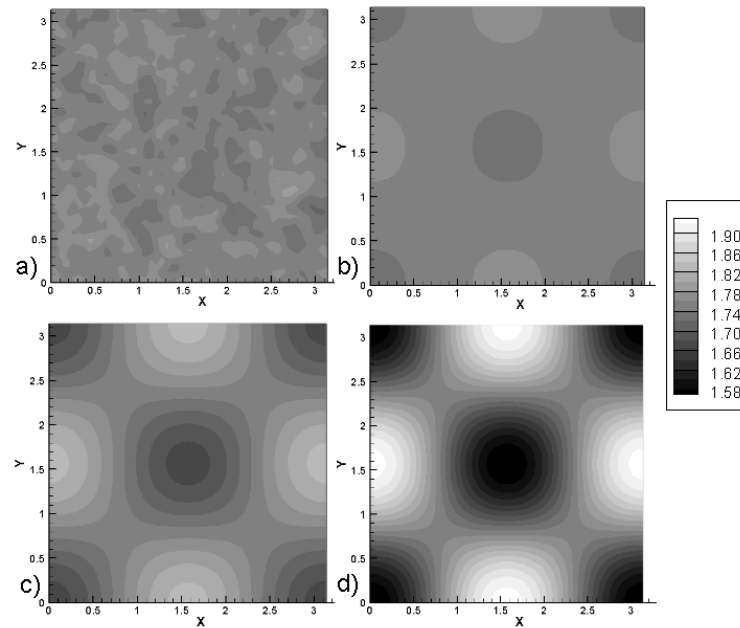


Figure 3.7: Glycolysis model in 2D. Pyruvate concentration. a) Initial condition, b) $t = 750$, c) $t = 1500$, d) $t = 2500$.

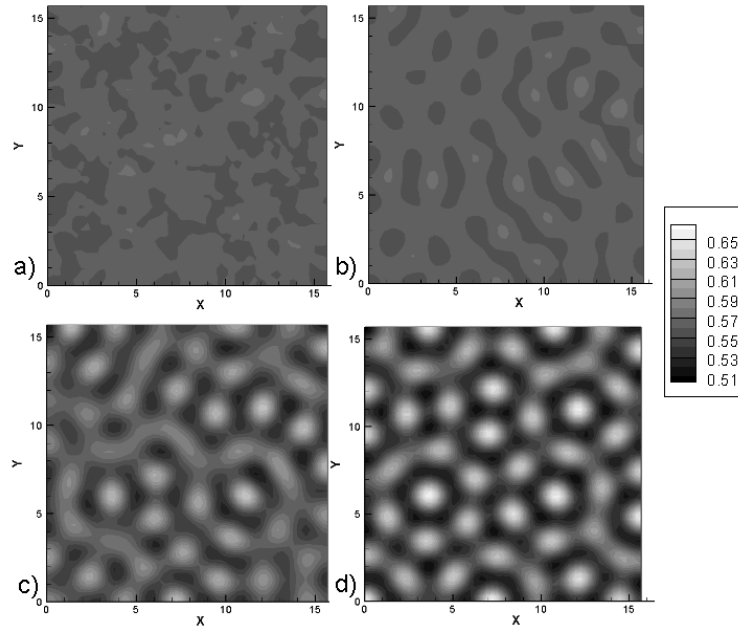


Figure 3.8: Glycolysis model in 2D. Spot-like patterns obtained for the glucose concentration.

a) Initial condition, b) $t = 750$, c) $t = 1500$, d) $t = 2500$.

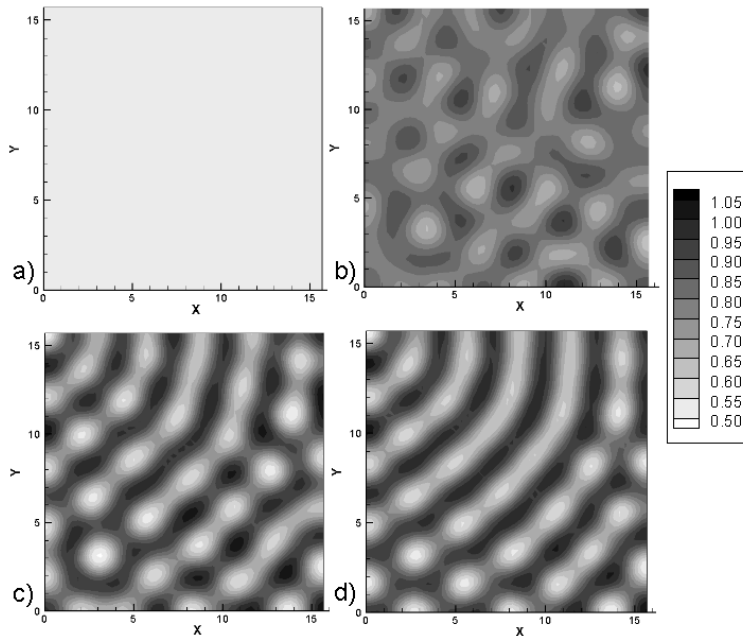


Figure 3.9: Glycolysis model in 2D. Stripe-like patterns obtained for the glucose concentration.

a) Initial condition, b) $t = 3000$, c) $t = 6000$, d) $t = 10000$.

$[0, 5\pi] \times [0, 5\pi]$, using the following set of numerical parameters: $D_u = 1.0$, $D_v = 0.08$, $\delta = 1.2$, and $k = 0.06$. Solution was obtained after 100000 iterations with a time step $\Delta t = 0.1$ for the same meshing as before. The initial conditions were given as a perturbation of 5% around the steady-state $u_s = 0.8$, $v_s = 1.2$. Results shown in Fig. 3.9 correspond to the formation of stripe-like patterns for the glucose concentration. An increase of almost twice the magnitude in the glucose concentration suggest that a significantly higher kinetic reaction between the chemicals is needed for the formation of stripe-like patterns. This fact is a consequence of the change in the parameters δ and k leading to changes in the production and consumption rates of both glucose and pyruvate (Eq. (3.6)).

3.5.3 Chemotaxis Model

The chemotaxis model was implemented using the bi-dimensional domain $[0,1] \times [0,1]$. The numerical parameters used were: $D_v = 0.005$, $\alpha = 2.0$, $\delta_u = 0.05$, $\delta_v = 0.05$, $\gamma = 0.001$, $p = 30$, and $r = 4$ [86]. The mesh consisted of 2500 quadrilateral patches defined by Lagrangian bilinear elements and 2601 nodes. Solution was obtained after 800 iterations with a time step of $\Delta t=0.01$.

Functions $f(u)$ and $g(v)$ have the form of activation/inhibition functions [82] and were calculated according to the following expressions [86]:

$$f(u) = \frac{u^p}{u^p + u_0^p} g(n) = \frac{\gamma n^p}{n^p + n_0^p}, \quad (3.30a)$$

where n_0 and u_0 are the threshold values of the variables u and v that start the activation/inhibition mechanism. In order to obtain a travelling wave-like spatial-temporal pattern, $n_0 = 0.01$ and $u_0 = 0.0195$ [86].

The initial conditions are given by the following rules:

$$\begin{aligned} n(x, y, 0) &= \begin{cases} n_i, & \text{if } x < x_i, y < y_i \\ 0, & \text{if } x \geq x_i, y \geq y_i \end{cases} \\ u(x, y, 0) &= u_i \end{aligned} \quad (3.31)$$

where $n_i = 1.0$, $x_i = 1.0$, and $u_i = 0.2$ [86]. Boundary conditions are zero in all cases. Results of the simulations are shown in Fig. 3.10 and 3.11, which are consistent with the results obtained elsewhere using the finite difference method [86] and represent the cell migration wave-like front obtained in response to the presence of the chemical signaling [82].

A final implementation was performed to couple the glycolysis model with the chemotaxis model. The aim of this approach is to obtain the formation of spot-like spatial-temporal patterns in combination with the travelling wave-like cell migration front. Accordingly, both the glycolysis and chemotaxis models are coupled as follows:

$$\frac{\partial q}{\partial t} = \gamma n u - \beta n q, \quad (3.32)$$

where u is the concentration of the chemical activator from the glycolysis model, n is the cell density from the chemotaxis model, and $\gamma = 0.05$ and $\beta = 0.05$. This coupled model is solved for the bi-dimensional domain $[0,1] \times [0,1]$ with a mesh of 2500 quadrilateral patches and Lagrangian bilinear elements with 2601 nodes. The numerical solution is obtained after 25000 iterations with a time step $\delta t = 0.1$. Initial and boundary conditions are zero in all

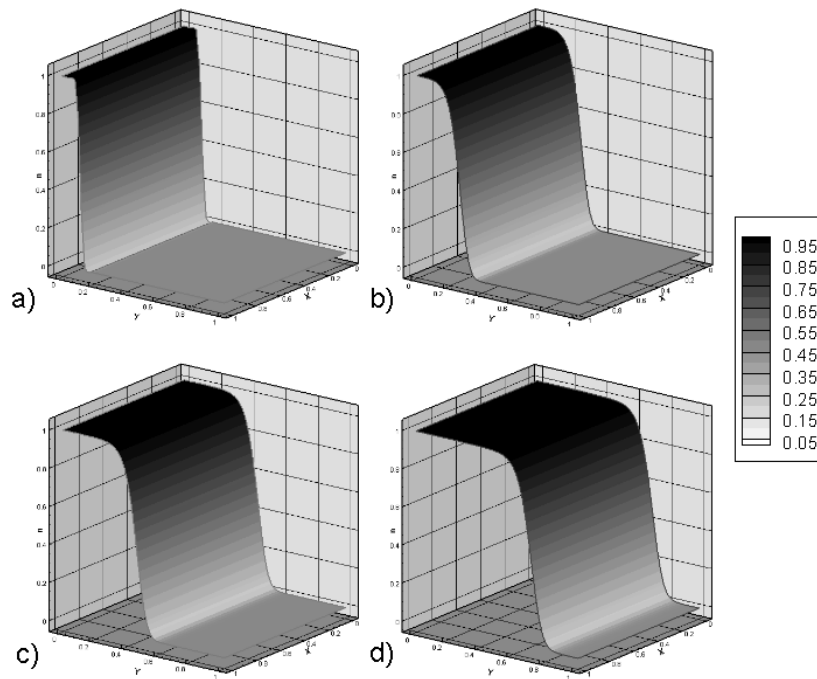


Figure 3.10: Chemotaxis model in 2D. Cell density. a) Initial condition, b) $t= 2.5$, c) $t= 5$, d) $t= 8$.

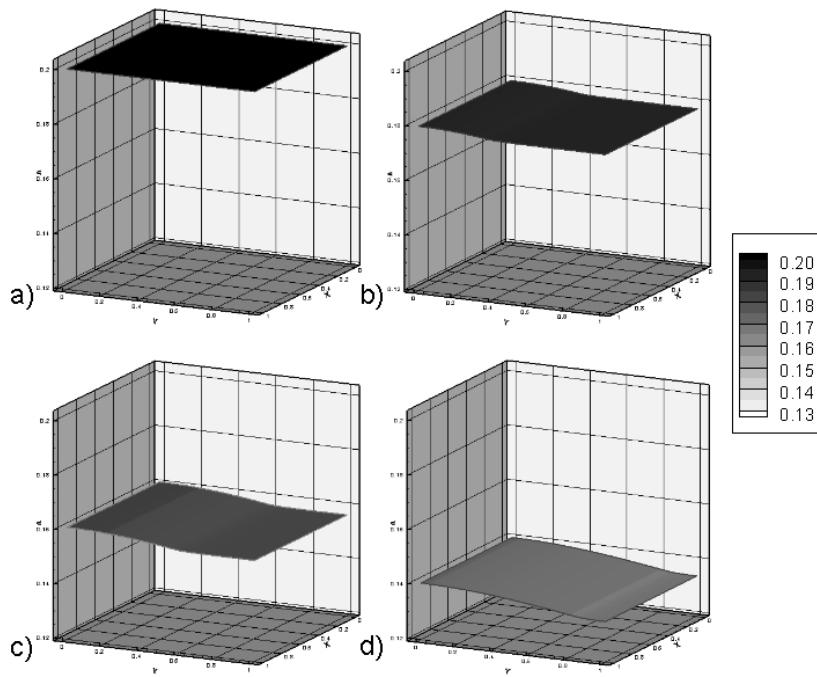


Figure 3.11: Chemotaxis model in 2D. Concentration of chemoattractant. a) Initial condition, b) $t= 2.5$, c) $t= 5$, d) $t= 8$.

cases. Since simulation times for the glycolysis and chemotaxis models are not the same, a time-adjusting strategy was used to synchronize the spot-like pattern formation with the travelling wave-like front. Accordingly, the glycolysis model is solved first and the coupling scheme is delayed to the proper iteration given by the chemotaxis model.

Results displayed in Fig. 3.12 show the appearance of the spot-like patterns concomitant with a wave-like cell migration front travelling from right to left in the x-axis. The magnitude of the spot-like formation is the same as found for the solution of the glycolysis model alone. This fact suggests that coupling the spot-like formation with a travelling cell migration maintains unaffected the spot-like formation although the appearance throughout the domain is controlled by the position of the cell migration front.

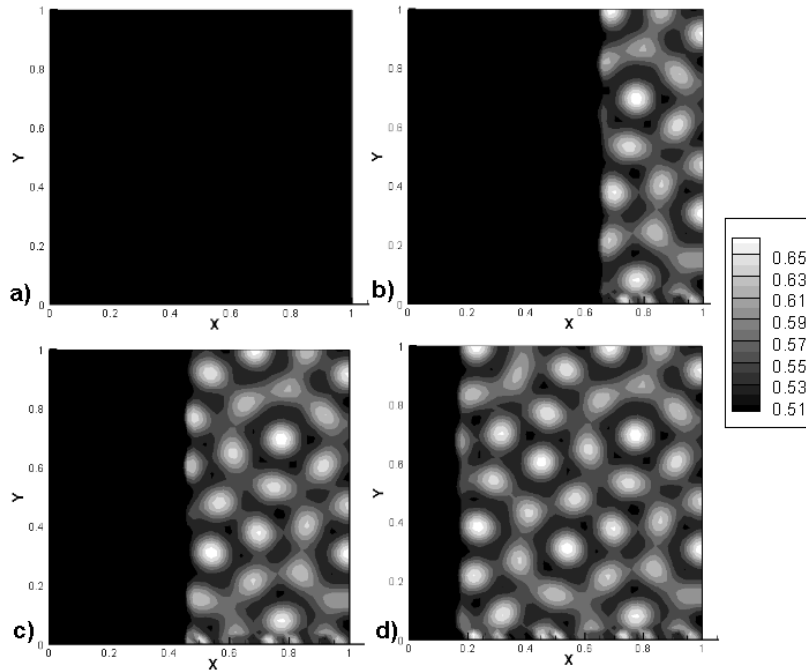


Figure 3.12: Glycolysis-chemotaxis coupling model. a) Initial condition, b) $t=750$, c) $t=1500$, d) $t=2500$.

3.6 Characteristics of the solutions

The numerical results show that the reaction-diffusion equations are suitable to describe features of some biological systems as the formation of spot and stripe patterns that appear in the skin of many animals, and the cell migration process [79, 86]. According to the numerical implementation, the formation of the expected spatial-temporal patterns depends on small perturbations of the steady-state used as initial conditions. These perturbations cause instabilities in the model that cause the formation of the patterns in response to the Turing-driven instabilities [90].

Furthermore, the selection of the numerical parameters must be consistent with the expected response. It has been observed that variations in parameter values lead to variations

in the solution. Moreover, numerical results show that modifications in the solution domain also affect the spatial-temporal patterns [77].

A first one-dimensional implementation of the Schnakenberg model show the interaction of both the activation and inhibition effects controlling the pattern formation (Fig. 3.3 and 3.4). Accordingly, a half-a-cycle phase shift was observed between the two chemical concentrations involved that respond to the non-linear terms present in the production and consumption mechanism of both chemicals (Eq. (3.5)). Similar shifted mechanisms have been observed in several pairs of biological agents, such as predator-prey populations, growth-feeding mechanism, epidemiological distributions within an environment, among many others [81].

With the bi-dimensional implementation, it is concluded that the numerical technique is suitable to be used in a more complex geometry since the shifted mechanism is conserved (Fig. 3.5). Furthermore, the magnitude of both chemical concentrations during the one-dimensional is preserved during the bi-dimensional implementation, in such a way that the results for the one-dimensional case can be considered the solution over a particular line crossing the bi-dimensional domain. In fact, this holds true when the parameters are the same for both implementations [78, 83].

More evidence of the influence of the numerical parameters and the domain dimension is obtained from the implementation of the glycolysis model. In this case, three different types of spatial-temporal patterns are obtained, as shown in Fig. 3.6 - 3.9. The formation of different spatial-temporal patterns according to changes in both the numerical parameters and the domain is a well known fact of the reaction-diffusion models [77, 90]. Furthermore, the lack of knowledge to select the adequate set of parameters might be an inconvenience for the validation a mathematical model against the real biological problem. As a consequence, mathematical models should be understood as tools providing approximate solutions whose accuracy depends on the availability of experimental (real) data to confront the numerical findings. Furthermore, changes in the numerical parameters or the solution domain may lead to a larger number of iterations (and smaller time steps) as in the case of the stripe-like patterns shown in Fig. 3.9, starting to be visible only after 60000 iterations. Nevertheless, the solution is stable for the formation of a fibrillar network and together with the results shown in Fig. 3.6 - 3.8, the glycolysis model can be associated with the formation of pigmentation patterns for applications in morphogenesis [79, 86], an also to mathematically describe growth events such as bone formation and fibers formation [68, 78].

The model of chemotaxis, in turn, can be considered a mathematical description suitable to represent cellular movement transport phenomena. The travelling wave-like spatial-temporal pattern obtained is similar in behaviour to the cell migration mechanism observed towards a chemical stimulus, in this case, the chemoattractant signal [82, 86]. According to the numerical results, there is a balance between the production term for the cells (mitosis) and the cell death (Eq. (3.7)a). This balance leads to the appearance of a constant density of cells in the migration front during the complete simulation. This implies a constant chemical consumption as observed in Fig. 3.11 that can be maintained because of a secondary balance between the chemical production and degradation terms (Eq. (3.7)b) [98]. The presence of these numerical balanced terms provides an homogeneous pattern formation throughout the domain that preserves the wave-like nature shown in Fig. 3.10.

In regard of the numerical results, the implementation of the biological models using the FEM approach described here allows to obtain solutions similar to those reported elsewhere using different techniques [77, 78, 86, 87]. Therefore, the numerical approach is suitable to be used to obtain the solution of complex mathematical models, providing accurate results

with lower computational cost in the cases where the numerical parameters, the meshing conditions and the time restrictions are well described. Nevertheless the limitations, both the mathematical models and the solution technique shown in this chapter can be used for the formulation and implementation of mathematical descriptions dealing with tissue formation and cell behaviour in applications related to wound healing and growth. A first approximation to this regard is shown in Fig. 3.12, where two specific pattern formations (spots and waves) are coupled to obtain a mixed pattern formation able to reproduce features of tissue growth as canaliculi formation in bone [37]. Further applications of this type of coupled-pattern mechanisms will be presented in the chapters 4 to 6.

4.1 Introduction

Cell movement and speed are biased by a static electric field. Cells exposed to a static electric field migrate parallel to the electric field lines in response to an effect called *galvanotaxis* or *electrotaxis*. Electrotaxis depends on the strength of the applied stimulus [5, 60] and on the presence of molecular activators [99, 100]. Since a static electric field induces reorientation of cell surface and signaling molecules [60, 99], the application of this kind of stimulus appears to be more important for cell migration than chemical and haptotactic signals [6, 60]. Indeed, it has been reported that an external electric field overrides other cell migration cues [5] and therefore it may be important for cell recruitment applications as wound healing and new tissues formation [1].

Several cell types change their initial direction of migration when an external electric field is applied and even change their current migration direction when the electric field is reversed in polarity [6, 100], supporting the fact that the electrical stimulus exerts higher control on cell migration than chemical guidance. Nevertheless, it has been also found that cells derived from the same tissue can migrate in opposite directions, and even cells from the same genotype may elicit same behaviour. Experiments conducted with rat calvaria and human osteogenic cells shown that although cell migration in both types of cells is increased in the presence of an external electric field, the direction of cell migration is opposed. Rat calvaria osteogenic cells were found to migrate towards the cathode whereas the human osteogenic cells migrated towards the anode [7]. This same difference in the direction of migration has been observed in other types of cells as fibroblasts, keratinocytes and endothelial cells [6]. Although it is clear that cell migration by electrotaxis is oriented towards a preferential electrode [6], the different cell migration directions resulting when an external electric field is applied could become a complication in the clinical treatment of a specific cell or tissue type. Therefore, cell migration and electrotaxis should be measured and quantify for specific tissues and cell types in order to define the electric performance that should be expected in the clinical applications.

Furthermore, the amount of cells recruited for cell migration depends on the strength of the applied external electric field [101]. Therefore, cell electrotaxis may be useful as a

way of not only directing cell migration but also as a means of controlling the number of cells arriving to a given surface. Moreover, the application of an electric field alters surface interactions between cells and materials and therefore cell colonization is improved [6, 59]. This leads to the hypothesis that an external static electric field may increase the number of cells arriving to a given substrate by increasing cell migration speed with the consequent increase in cell colonization dependent of the electric field strength. Several experimental approaches have provided data to this respect but to the best of our knowledge no effort has been made to quantify the increment on cell colonization over a surface. Since an experimental approach to this matter requires a rigorous set up and planning efforts in order to avoid unexpected outcomes [8], a computational simulation is to be suitable to overcome these difficulties [26, 98, 102].

This chapter is aimed at presenting a mathematical model of cell electrotaxis of osteogenic cells. The model is intended to obtain, by means of a numerical approach, additional information of the changes of cell migration and cell recruitment when an external electric field is applied. The results propose remarks about the relation between electric field, cell migration and surface colonization for osteogenic cells, and define a pathway for future applications regarding tissue formation and reduced healing times in wounds.

4.2 Mathematical model

The experimental evidence shows that cell migration due to electrotaxis deals with the interaction between the external electric potential and a biochemical pathway not well understood [5]. However, it is accepted that under physiological conditions an external electrical stimulus influence cell behaviour in different types of cells, including osteoblasts [7, 9]. It has been also stated that the electrical stimulus is an override signal for chemical stimulus [5] and that changes in osteoblasts activity due to an electrical stimulus may increase bone formation and reduce healing times [74, 103]. Therefore, we have simplified a typical electrotaxis set up for an osteoblasts cell-like culture into three model variables, namely, the osteogenic cells density $C_o(\mathbf{x}, t)$, the osteogenic chemical concentration $Q_o(\mathbf{x}, t)$, and the external electric potential $V_e(\mathbf{x})$. Other cell types and molecules that may be present during the cell culture, and other kinds of external stimulus, i.e. mechanical forces, are also avoided for the sake of simplicity.

Osteogenic cells

The flow of osteogenic cells is described as a random dispersion expression controlled by the presence of an osteogenic chemical [82, 86]. This is mathematically described as a linear diffusion term with coefficient D_{C_o} together with a linear chemotactic term with sensitivity coefficient H_{C_o} taken in the direction of the osteogenic chemical gradient. Electrotaxis is described as an additional transport term due to the gradient of the electric potential with an anisotropic electrical sensitivity coefficient E_{C_o} , with value different from zero only in the direction of the electric field. The negative sign indicates that osteogenic cells migrate towards the anode and in the opposite direction of the electric field vector [7]. Cell proliferation is modelled with a logistic linear term [86] with coefficient r_{C_o} and saturation C_i controlled by an activation function which threshold value W_{Q_o} corresponds to the minimum concentration of osteogenic chemical required to initiate cell migration [82, 86]. Parameter n refers to the

slope of the cell proliferation activation function. The equation is complemented by a term of cell death with coefficient δ_{C_o} .

$$\begin{aligned}
 \underbrace{\frac{\partial C_o}{\partial t}}_{\text{Time variation}} &= \nabla \cdot \underbrace{\left[\underbrace{D_{C_o} \nabla C_o}_{\text{Diffusion}} - \underbrace{H_{C_o} C_o \nabla Q_o}_{\text{Chemotaxis}} - \underbrace{E_{C_o} C_o \nabla V_e}_{\text{Electrotaxis}} \right]}_{\text{Diffusion}} \\
 &+ \underbrace{r_{C_o} C_o \left[1 - \frac{C_o}{C_i} \right] \left[\frac{Q_o^n}{Q_o^n + W_{Q_o}^n} \right]}_{\text{Proliferation}} - \underbrace{\delta_{C_o} C_o}_{\text{Death}}
 \end{aligned} \tag{4.1}$$

Osteogenic chemical

The random dispersion of the osteogenic chemical is represented as a linear diffusion term with coefficient D_{Q_o} . Since osteogenic chemical is released during the migration and proliferation of the osteogenic cells [36], its production is modelled as a linear term with coefficient r_{Q_o} given in function of the concentration of osteogenic cells and an independent term with coefficient r_{V_e} associated with the increased chemical production by the presence of the external electrical stimulus [8]. Chemical consumption is represented by a natural linear decay term with coefficient δ_{Q_o} and a nonlinear term with coefficient δ_{QC} representing the chemical consumed by the concentration of osteogenic cells.

$$\begin{aligned}
 \underbrace{\frac{\partial Q_o}{\partial t}}_{\text{Time variation}} &= \underbrace{D_{Q_o} \nabla^2 Q_o}_{\text{Diffusion}} + \underbrace{(r_{Q_o} + r_{V_e} V_e) C_o}_{\text{Production}} - \underbrace{(\delta_{Q_o} + \delta_{QC} C_o) Q_o}_{\text{Consumption}}
 \end{aligned} \tag{4.2}$$

Electrical potential

The electric potential satisfies Laplace's equation:

$$\underbrace{\nabla \cdot (\nabla V_e)}_{\text{Laplace equation}} = 0. \tag{4.3}$$

Since body cells have dielectric properties [4], the net charge inside a Gaussian surface enclosing the osteoblasts cell-like culture is zero. According to experimental reports on electrically mediated blood clotting and bone cells migration, the presence of a static electrical stimulus results in increased rates of cell activation [9, 104, 105]. Furthermore, as the effects of such kind of stimulus may last for hours, days and even weeks, it is believed that they influence long-lasting biological processes such as wound healing [1]. Therefore, only static potentials are considered for this model.

From literature reviews and from numerical results reported elsewhere [106], we obtained the values for the parameters of the model described by Eqs. (4.1) - (4.3). Table 4.2 resumes the values used in the simulations. A more details explanation on the origin of these values is available in the appendix.

Parameter	Value	Units	Reference
D_{C_o}	5.0×10^{-6}	mm^2/min	[14, 26]
H_{C_o}	5.0×10^{-4}	$(\text{mm}^2/\text{min})(\text{ml}/\text{mg})$	[14]
E_{C_o}	5.0×10^{-4}	mm^2/min	[5, 7]
r_{C_o}	3.57×10^{-3}	min^{-1}	[106]
δ_{C_o}	1.388×10^{-5}	min^{-1}	[106]
W_{Q_o}	1.0×10^{-3}	mm^2	[106]
D_{Q_o}	2.88×10^{-5}	mm^2/min	[14, 26]
r_{Q_o}	1.0×10^{-5}	min^{-1}	[26, 106]
r_{V_e}	5.0×10^{-5}	$(\text{V} \cdot \text{min})^{-1}$	N.E.*
δ_{Q_o}	2.0×10^{-3}	min^{-1}	[14, 107]
δ_{QC}	3.0×10^{-5}	$\text{min}^{-1} (\text{ml}/\text{cells})$	[26]
$ \bar{v} $	1.0×10^{-3}	mm/min	N.E.*

* N.E. = Numerical Experiment

Table 4.1: Parameter values for the mathematical model of electrotaxis

4.3 Description of the simulation

The proposed model was implemented for a two-dimensional domain representing an ideal 1 mm-side square cell culture dish. The mesh used consisted of 2500 quadrilateral bilinear elements and 2601 nodes. As initial condition, osteogenic cells were seeded in a 0.2 mm side square-shaped area centred with the mesh. The initial condition for the osteogenic chemical was assumed to be 5×10^4 mg/ml [14, 106]. An external electric field was applied to the lateral sides of the mesh as shown in Fig. 4.1. The direction of the electric field was chosen according to the simulation cases later described, with strength ranging from 0 to 10 V/cm [5, 7, 9]. In some of this cases, an osteogenic chemical boundary condition was applied to the right side of the domain (Fig. 4.1) [14, 106]. Simulation consisted of 1500 time steps each one equivalent to one minute real time.

The model was implemented using the finite element method for the spatial discretization and a *Backward Euler* implicit finite difference scheme for the temporal discretization. The solution of the resulting nonlinear system of equations was implemented using the Newton-Raphson method [95] and numerically solved using a Fortran user subroutine. The computational solution of the model was obtained using an OS/Windows desktop computer with Intel Core i7 3.4GHz and 8GB RAM. All simulations were successfully completed approximately in one minute.

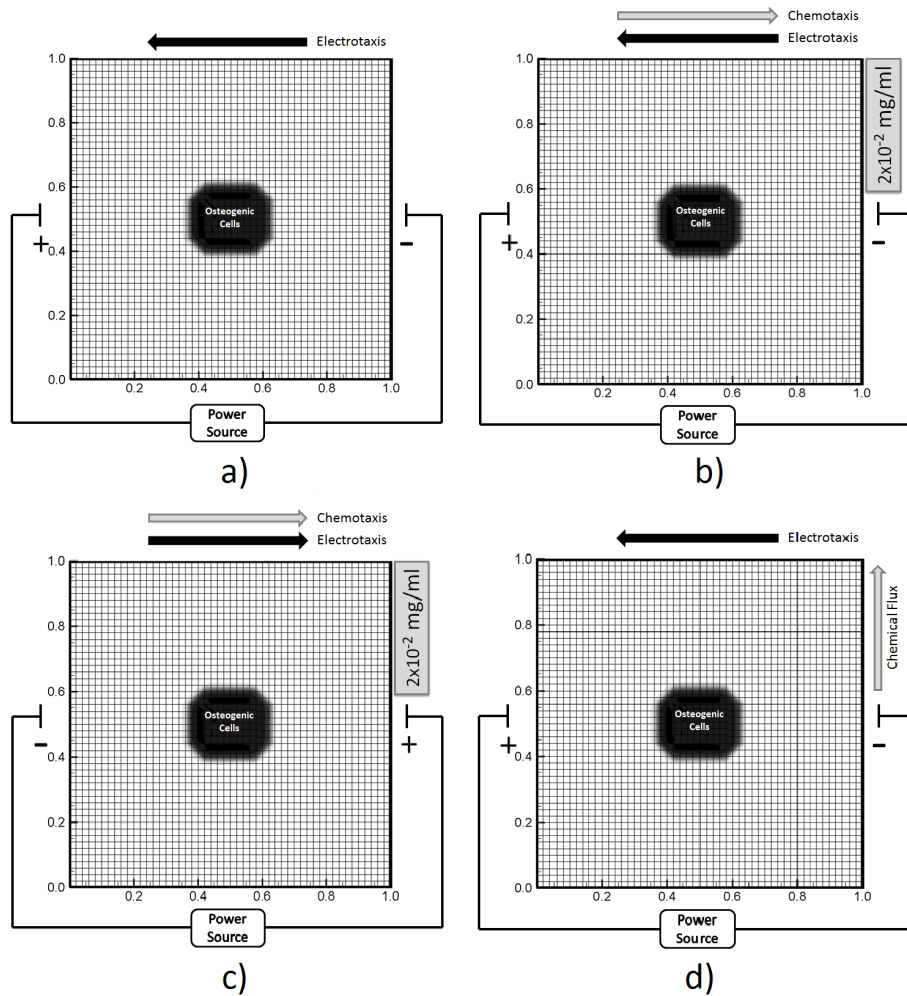


Figure 4.1: Mesh, initial and boundary conditions for the analysed cases. a) Electrical stimulus only. b) Chemical and electrical stimuli direct cell migration in opposite directions. c) Chemical and electrical stimuli direct cell migration in the same direction. d) Convective flux of chemical perpendicular to the electric field vector.

4.3.1 Analyzed cases

Four different experimental cases were extracted from the literature and numerically implemented (Fig. 4.1). The first case reproduced a situation where cells are exposed to a static electric field in order to assess their directional migration (Fig. 4.1a). The magnitude of the electric field varied in the range 0-10 V/cm and measurements for cell position were taken after 700, 1200 and 1500 minutes. As a control test, the electric field was replaced by a chemical stimulus of 2×10^{-2} mg/ml. Measurements for this control condition were also taken after 700, 1200 and 1500 minutes.

In order to evaluate cell migration response to changes in electric field direction, a complementary condition in which an electric field changes direction was also implemented [100]. Cells were initially concentrated in the middle of the domain and an electric field of 500 mV/mm was applied with the anode on the right side of the domain. After 500 minutes of exposure, the electric field changed direction and hence the anode was placed on the left side of the domain. Measurements for cell migration under these conditions were taken after 0, 500, 1000 and 1500 minutes of exposure.

The second case included a chemical stimulus in the right-side border of the domain and a static electric field that directed cell migration in the opposite direction of that of the chemical stimulus (Fig. 4.1b) [5]. The purpose of this condition was to assess the overriding effect of the electric field over the chemical stimulus. The magnitude of the electric field varied in the range 0-10 V/cm and the chemical stimulus varied in the range $(1-15) \times 10^{-2}$ mg/ml. Measurements for cell position were taken after 700, 1200 and 1500 minutes.

The third case attempted to evaluate changes in the cell migration profile when the electric field directs cell migration in the same direction of the chemical stimulus (Fig. 4.1c) [5]. In concordance to the abovementioned cases, the magnitude of the electric field varied in the range 0-10 V/cm and measurements for cell position were taken after 700, 1200 and 1500 minutes.

The fourth condition was intended to provide an additional support of the overriding effect of the electric field by excluding any possible involvement of chemotactic effects in the cell migration directed by the electric field. This was achieved by introducing a continuous cross flow of osteogenic chemical perpendicular to the electric field vector (Fig. 4.1d) [1, 5]. This flow was modelled by means of a convective term with velocity \bar{v} that modifies the osteogenic chemical equation in Eq. (4.3) as follows:

$$\underbrace{\frac{\partial Q_o}{\partial t}}_{\text{Time variation}} + \underbrace{\bar{v} \cdot (\nabla Q_o)}_{\text{Convection}} = \text{Diffusion} + \text{Production} - \text{Consumption} \quad (4.4)$$

For this latter case, electric field was fixed as 500 mV/mm and no osteogenic chemical boundary condition was applied. Measurements for cell position were taken after 700, 1200 and 1500 minutes.

Cell position was obtained in all cases by calculating the distance over an horizontal line crossing the centre of the domain between the middle point (maximal) of the cell contingent and its lateral borders with densities up to 5% the maximal value. Cell migration speed was calculated as net migration distance/duration of migration [60, 100]. Additional information for the number of osteogenic cells colonizing rather the anode side or the chemical stimulus (Fig. 4.1) was obtained by measuring the osteogenic cell density in the middle point of the corresponding domain boundary.

4.4 Results

4.4.1 First case: Electrotaxis

The effect of the electric field on cell migration has been assessed by applying different strengths of the static electric field to the osteogenic cells, without any additional chemical stimulus, as shown in Fig. 4.1a. Results show that cell migration depends on the strength of the electric field and that cell migration is directed towards the anode by electric fields above 100 mV/mm (Fig. 4.2). Below this threshold value for the electric field, cells are able to sense the electrical stimulus but with a less significant migration pattern, and a tendency of cells to remain in place is observed.

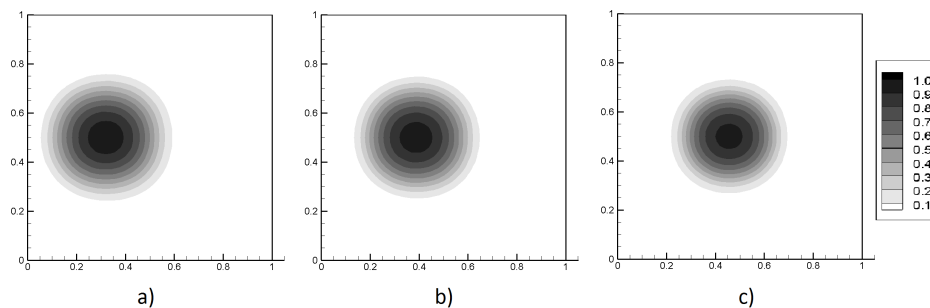


Figure 4.2: Osteogenic cell migration (in mg/ml) after 700 minutes of exposure to different strengths of electric field. a) $E = 500$ mV/mm. b) $E = 300$ mV/mm. c) $E = 100$ mV/mm.

Cell colonization of the anode is estimated by measuring the cell density over the anode side for different electric field strengths after 1500 minutes. Results show that the cell density and cell spreading over the anode side increases as the applied electric field is increased (Fig. 4.3). In this case, an electric field of 200 mV/mm allows cells to barely arrive to the anode, while an electric field of 300 mV/mm leads to an initial colonization and cell spreading that increases for electric fields up to 500 mV/mm.

In addition, the effect of a chemical stimulus without the application of an electrical field has been computed as a form of control. Osteogenic cells have been stimulated with an osteogenic chemical boundary placed instead of the positive electrode shown in Fig. 2.1a. Results after 1500 minutes show that cells under this condition move towards the applied chemical stimulus as shown in Fig. 2.4.

Measurements for cell migration were taken after 1200 minutes of exposure to the electric field (Fig. 4.2) and a linear relation was found between the cell migration speed and the electric field strength as shown in Fig. 4.5a. According to this relation, it was found that in the presence of an electric field osteogenic cells migrate towards the anode at a rate of 7.3150×10^{-9} mm²/(mV · s), and that for an electric field of 500 mV/mm cell migration speed due to electrotaxis is 3.6575×10^{-6} mm/s. Notice from Fig. 4.5a that without electric field there remains a small value for cell migration speed. This value was determined as 4.3842×10^{-7} mm/s and corresponds to the cell migration by the diffusive effect. Therefore, the total cell migration speed amounts to the sum of the electrotaxis and the diffusive effects being 4.0959×10^{-6} mm/s.

Results for cell colonization given in Fig. 4.3 reveals that there is a logarithmic relation

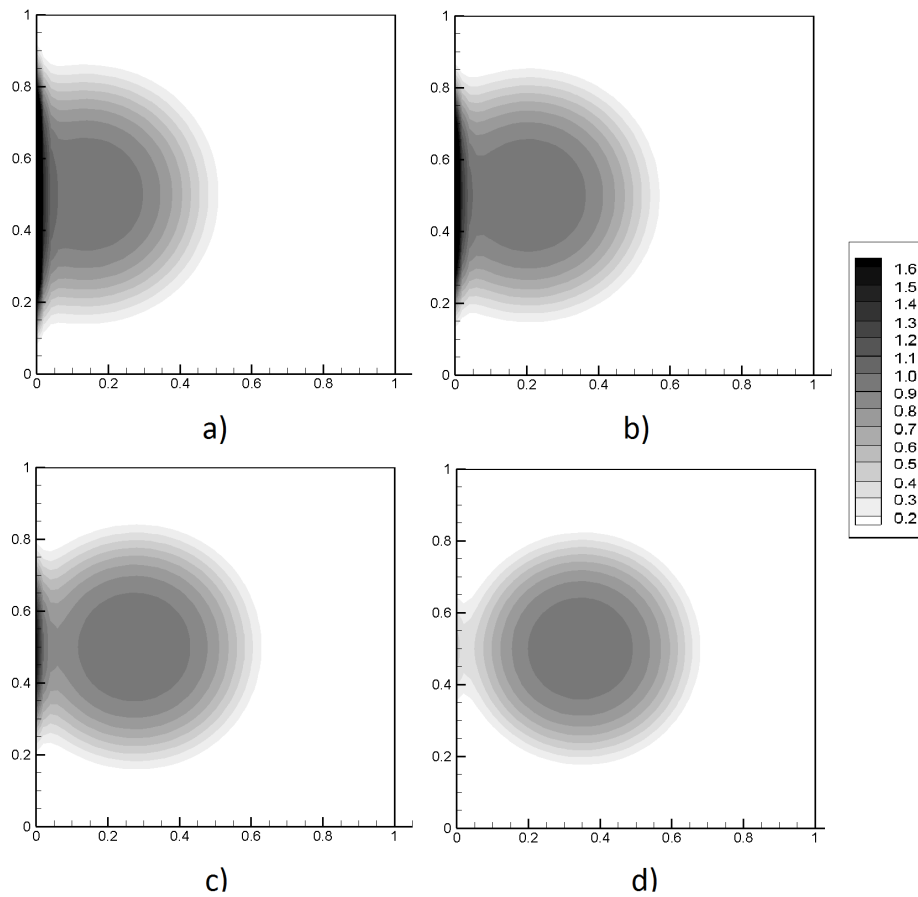


Figure 4.3: Osteogenic cells colonization (in mg/ml) of the anode after 1500 minutes of stimulation with different electric field strengths. a) $E=500$ mV/mm. b) $E=400$ mV/mm. c) $E=300$ mV/mm. d) $E=200$ mV/mm.

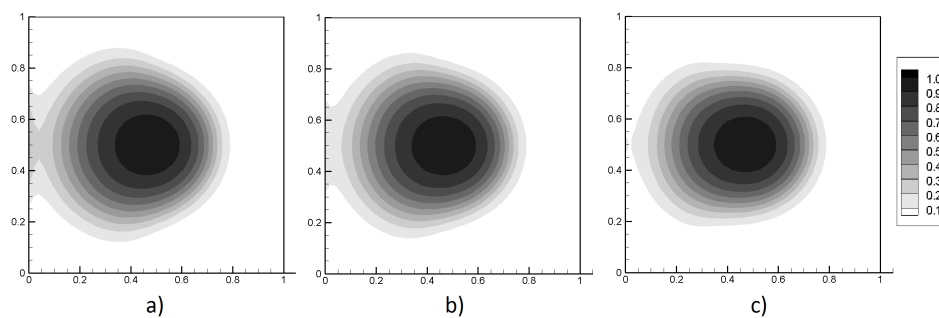


Figure 4.4: Osteogenic cells migration (in mg/ml) after 1500 minutes of exposure only to a chemical stimulus applied at the left side of the domain. a) $Q_o= 3 \times 10^{-2}$ mg/ml. b) $Q_o= 2 \times 10^{-2}$ mg/ml. c) $Q_o= 1 \times 10^{-2}$ mg/ml.

between the strength of the external electric field and the cell density colonizing at the anode side as shown in Fig. 4.5b. Using this relation it has been found that cells arrive to the anode if an external electric field of 172.6 mV/mm is applied. It has also been found that cell density at the anode side increases to reach the normalized concentration value when an external electric field of 242.3 mV/mm is applied. This means that for values below 172.6 mV/mm cells are not able to reach the cathode side and that for values over 242.3 mV/mm cells colonize the anode and begin to proliferate mostly over it.

Furthermore, and according to results for cell migration under a chemical stimulus (Fig. 4.4), a linear relation was found between the applied chemical stimulus and the net displacement of the cell contingent related to a control state with no chemical stimulus. However, by increasing the values for the chemical stimulus it has been found that after 1200 minutes the initial linear behaviour changes into logarithmic as shown in Fig. 4.5c. Using this relation it has been found that cells under a chemical stimulus of 2×10^{-2} mg/ml, given as the average osteogenic chemical concentration produced by cells under a numerical control test with no chemical and electrical stimuli [14,98], exhibit a migration speed of 9.6434×10^{-7} mm/s, which amounts to 23.54% of the speed obtained if an external electric field of 500 mV/mm has been applied, a value that is comparable with experimental observations [7,9].

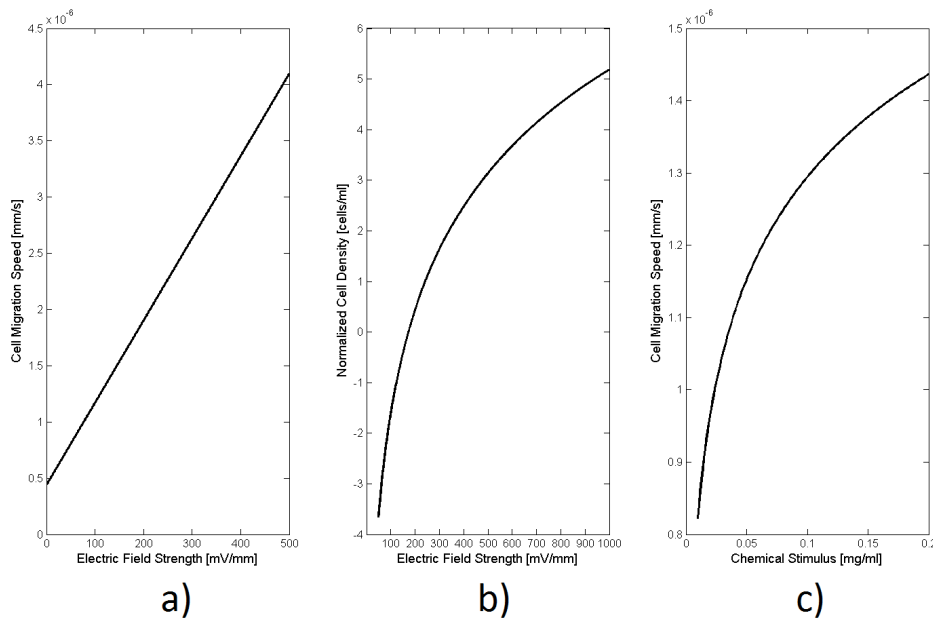


Figure 4.5: Numerical relations for cell migration directed by an external electric field. a) Relation between the distance covered by cells and the electric field strength. b) Relation between the electric field and cell colonization of the anode. c) Relation between the chemical stimulus and cell migration in the absence of electric field.

Finally, cell migration response to changes in the electric field direction has been assessed by implementing a complementary condition in which cells were exposed during 1500 minutes to an electric field of 500 mV/mm followed by 500 minutes of exposure with changed direction of polarization. According to results of this condition, the direction of the osteogenic cell

migration follows the direction of the electric field, as shown in Fig. 4.6. Therefore, changes in the direction of the electric field vector cause changes in the direction towards which cells migrate, in this case, towards the anode. However, it must be highlighted that changes in the direction of the electric field vector have no effect on cell diffusion and proliferation behaviours since the cell density keeps the growing rate and distribution even after the electric field changes direction (Fig. 4.6b-4.6c). Moreover, the distribution pattern after 1500 minutes of exposure (Fig. 4.6d) is equal to the case when the electric field remains unchanged (Fig. 4.3a), despite of the cell colonization process shown in the latter case. Measurements on cell migration after 500, 1000 and 1500 minutes of exposure revealed that cell migration speed including the diffusion effect are not influenced by with the change in the direction of the electric field. Only the cell migration direction, as explained by cell electrotaxis, is influenced. This independence of the cell migration speed from electric field direction can be qualitatively observed in the result shown after 1000 minutes of exposure (Fig. 4.6c) because the cell density is located again in the centre of the domain. Differences in the patterns obey only to the diffusion and proliferation terms as described in Eq. (4.1).

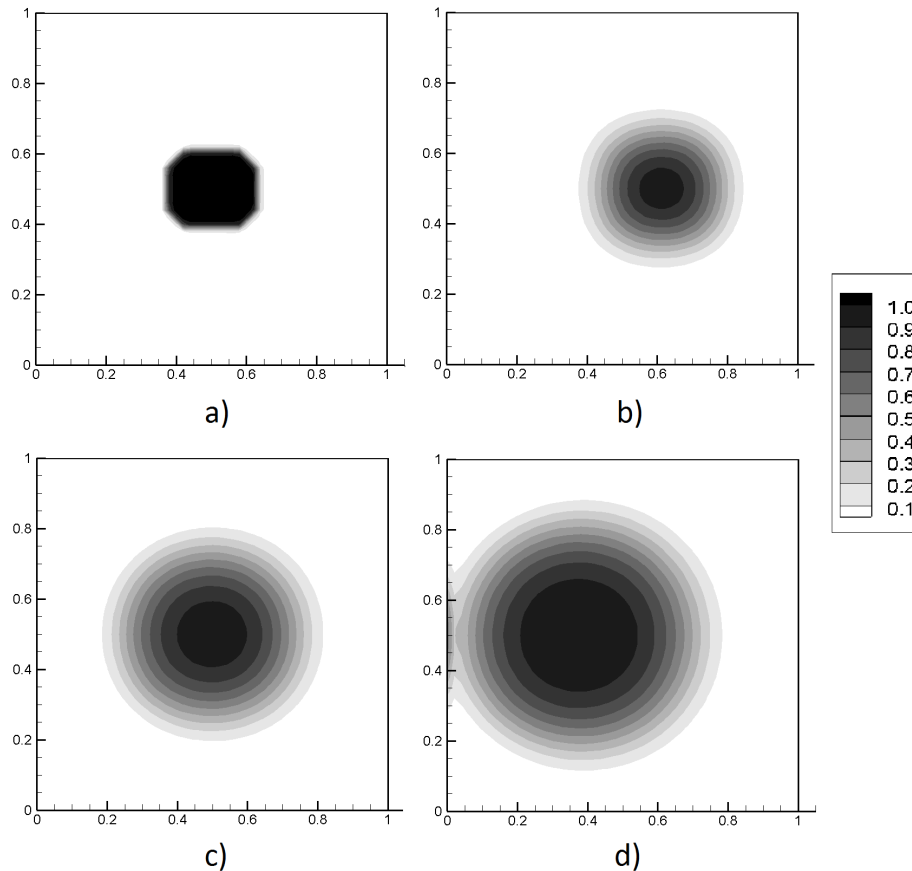


Figure 4.6: Osteogenic cell migration (in mg/ml) when the applied electric field changes direction. a) Initial condition, no electric field. b) $t=500$ minutes, anode at right side. c) $t=1000$, anode at left side. d) $t=1500$ minutes, anode at left side.

4.4.2 Second case: Chemotaxis opposed to electrotaxis

A second experiment has been performed to evaluate cell migration response when an external electric field and a chemical stimulus are simultaneously applied to cells but directing cell migration in opposite directions (Fig. 4.1b). Results show that osteogenic cells respond to both the electric and the chemical stimulus. However, above a certain threshold value, the electrical stimulus dominates and determines the direction of cell migration as shown in Fig. 4.7.

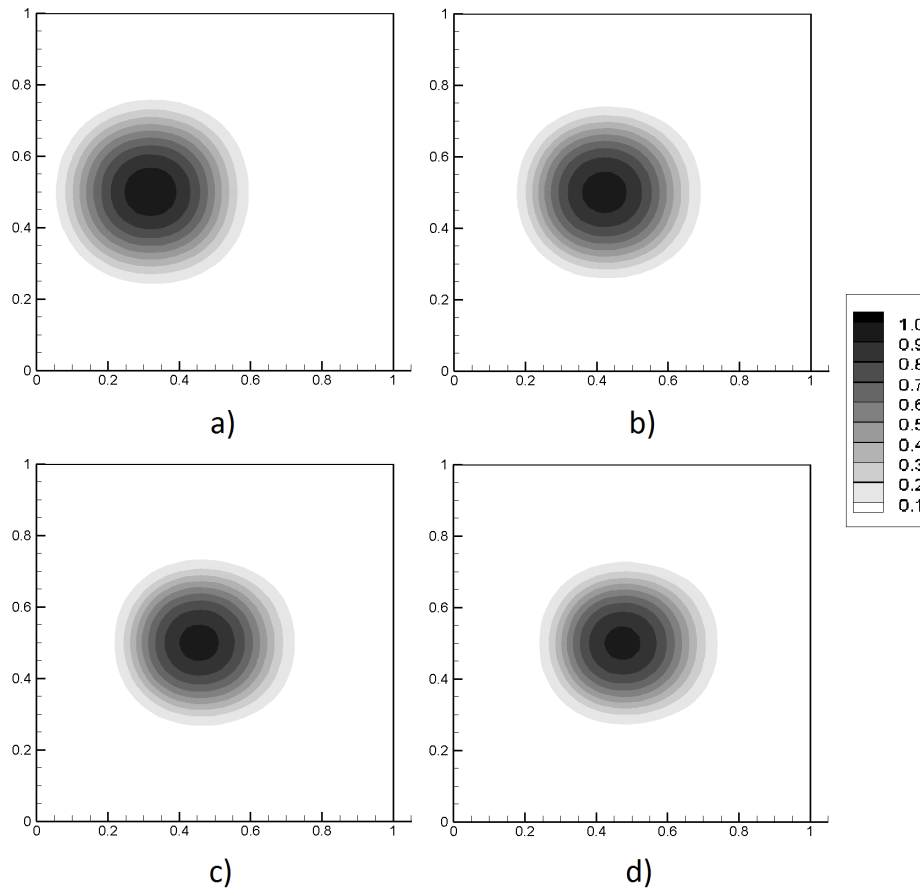


Figure 4.7: Osteogenic cell migration (in mg/ml) after 700 minutes of stimulation with different electric field strengths and a chemical stimulus directing migration in opposite direction. a) $E= 500$ mV/mm. b) $E= 200$ mV/mm. c) $E=100$ mV/mm. d) $E= 50$ mV/mm.

To calculate the electric field threshold strength directing cell migration towards the anode, the distance covered by cells after 1200 minutes of exposure to the electric field has been measured. A linear relation has been found between the position of the cell contingent and the electric field strength as shown in Fig. 4.8a. This relation shows that for very low strengths of electric field the cell migration is negative. This means that cell migration is mainly induced by chemotaxis and therefore directed towards the chemical stimulus source. On the other hand, for high strengths of electric field, cell migration is positive as it is mainly

controlled by the electrotaxis and therefore directed towards the anode.

By calculating the x-cross of this curve, it has been determined that the electric field strength that counteracts the chemical stimulus is 34.95 mV/mm. Interestingly, the test for this value showed that there is a deviation of the cell contingent from the initial condition towards the chemical stimulus. This deviation can be explained by the remnants of chemotaxis as shown in Figs. 4.9c - 4.9d. A measurement of cell contingent position after 1200 minutes shows that for the given threshold value of the electric field (Fig. 4.9c) cells move about $2\mu\text{m}$ towards the chemical stimulus and that when no electric field is applied (Fig. 4.9d) cells move $46\mu\text{m}$. Therefore, an electric field of 34.95 mV/mm counteracts the chemical stimulus and provides a threshold value for electric field strength above which osteogenic cells clearly respond to the electrical stimulus, an observation that is correlated with experimental observations [5].

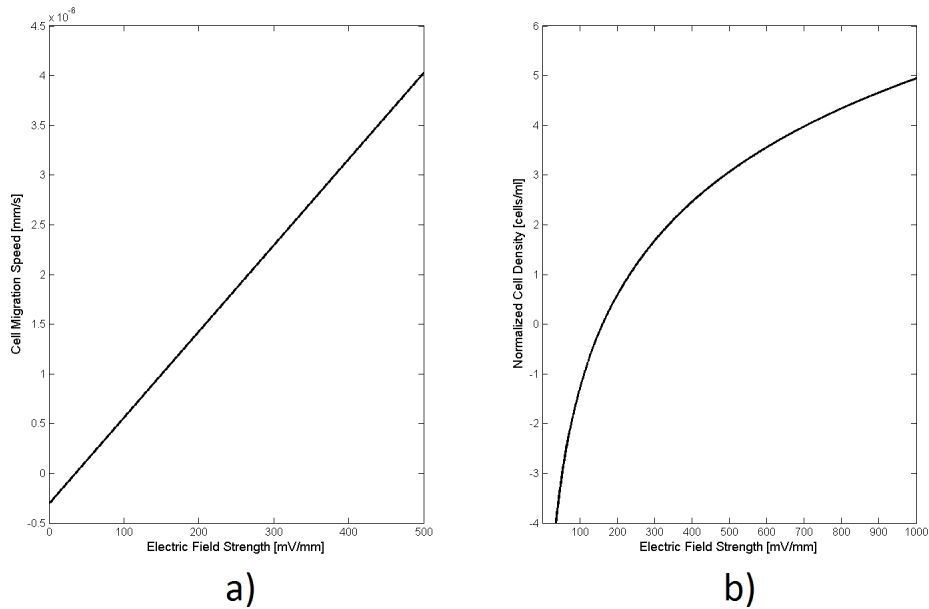


Figure 4.8: Numerical relations for cell migration directed by an electric field with an opposite-side chemical stimulus. a) Relation between the velocity (in mm/s) resulting from the movement of the osteogenic cells after the given exposure time, and the electric field strength. b) Relation between electric field and cell colonization of the anode.

Additionally, and using the linear relation shown in Fig. 4.8a, it has been possible to calculate the cell migration speed of the osteogenic cells under the conditions given in Fig. 4.1b. It has been found that osteogenic cells migrate by electrotaxis at a rate of $8.6273 \times 10^{-9} \text{ mm}^2/(\text{mV} \cdot \text{s})$, and that for an electric field of 500 mV/mm the cell speed is $4.313 \times 10^{-6} \text{ mm/s}$. However, when no electric field is applied, Fig. 4.8a exhibits a negative value for the cell migration speed. Together with the electrotaxis term a second term is causing the cell migration by chemotaxis and the diffusive effect shown in Fig. 4.5a. The negative sign indicates that cell migration is directed towards the chemical stimulus, i.e., opposite to electrotaxis. By subtracting the diffusive effect, it has been found that cells migrate by chemotaxis at $-7.3990 \times 10^{-7} \text{ mm/s}$. The total cell migration speed is given as the sum of the electrotaxis,

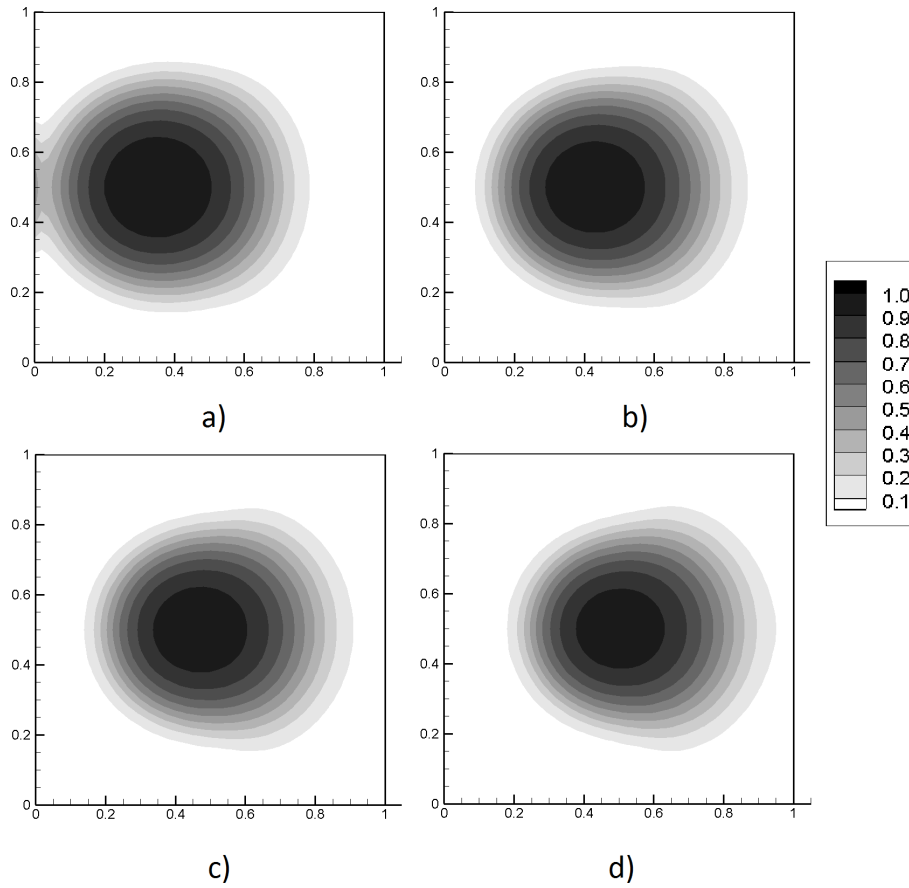


Figure 4.9: Osteogenic cell migration (in mg/ml) after 1500 minutes of stimulation with low strengths of electric field and a chemical stimulus directing cell migration in the opposite direction. a) $E = 200$ mV/mm. b) $E = 100$ mV/mm. c) $E = 34.95$ mV/mm. d) $E = 0$ mV/mm.

chemotaxis and diffusive effect and amounts to 4.0122×10^{-6} mm/s, a value that is close to the speed obtained when only the electrical stimulus is applied (Fig. 4.5a). This result also correlates with experimental data where a chemical stimulus opposite to the electric field vector reduces cell migration speed [5].

Finally, cell colonization of the anode is estimated. Results show that after 1500 minutes cell density and cell spreading exhibit a similar behaviour to that presented in Fig. 4.3 when no chemical stimulus is applied. Moreover, results show that there is also a logarithmic relation between the strength of the electric field and the cell density colonizing at the anode side as shown in Fig. 4.8b. Using this relation it was found that cells arrive to the anode if an external electric field of 162.5 mV/mm is applied. It was also found that the cell density at the anode side increases to reach the normalized concentration value when an external electric field of 236.1 mV/mm is applied. These values represent a difference of 5.85% and 2.63% with respect to the values obtained when only the electrical stimulus is applied, namely 172.6 mV/mm and 242.3 mV/mm respectively.

4.4.3 Third case: Electrotaxis aided by chemotaxis

A third experiment has been performed to evaluate cell migration when the electric field and a chemical stimulus both direct cell migration in the same direction (Fig. 4.1c). Results show that cells migrate towards the source of both electrical and chemical stimulus (Fig. 4.10), in a similar way as observed when the electric field is the only stimulus.

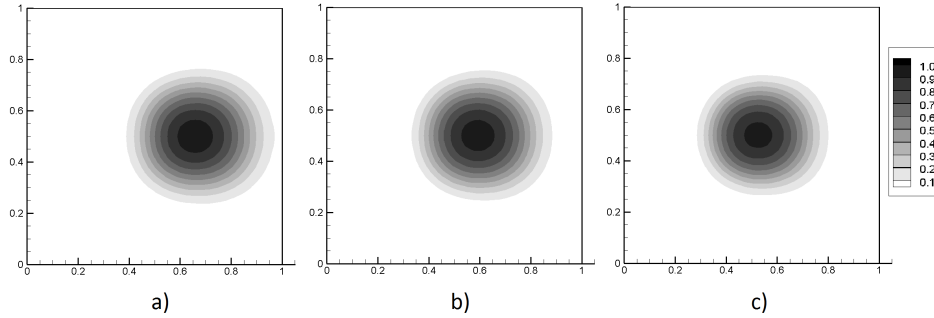


Figure 4.10: Osteogenic cell migration (in mg/ml) after 700 minutes of exposure to different strengths of the electric field and with a chemical stimulus directing cell migration in the same direction. a) $E = 500$ mV/mm. b) $E = 300$ mV/mm. c) $E = 100$ mV/mm.

Measurements for cell migration were taken after 1200 minutes of exposure to the electric field and a linear relation was found between the cell migration speed and the electric field strength as presented in Fig. 4.11a. This relation, as in Figs. 4.5a and 4.8a, also consists of two contributions. The first contribution is related to the electric field and leads to a cell migration rate by electrotaxis of 7.8362×10^{-9} mm²/(mV · s). Assuming an electric field of 500 mV/mm, cell migration speed amounts to 3.9181×10^{-6} mm/s. The second contribution accounts for the chemotaxis and diffusive effects. Therefore, subtracting the diffusion term found in Fig. 4.5a, the cell migration speed by chemotaxis is found to be 7.4108×10^{-7} mm/s. The total cell migration speed is obtained as the sum of the electrotaxis, chemotaxis and diffusion contributions and amounts to 5.0976×10^{-6} mm/s. This total cell migration speed is higher than the speed obtained in the case where only the electrical stimulus is applied (Fig. 4.5a). In fact, there is an increase of 19.65% when compared to the result shown in Fig. 4.5a and an increase of 18.65% when the value is compared to the case where the chemical stimulus directs cell migration in an opposite direction than the electric field does (Fig. 4.8a).

Cell colonization of the anode was measured after 1500 minutes of exposure to both the chemical stimulus and a variable electric field. Results obtained show that cell density and cell spreading over the anode side increases as the applied electric field strength is increased (Fig. 4.12). Although this behaviour equals that found when only the electrical stimulus is applied, differences should be considered in terms of the direction of the electric field (left to right) and the presence of a chemical stimulus that also directs cell migration towards the anode (right side of the domain), as depicted in Fig. 4.1c.

Figure 4.12a and 4.12b show that the cell density at the surface of the anode is higher and largely spread compared to the case in which no chemical stimulus is applied (Fig. 4.3a and 4.3b). Furthermore, from Fig. 4.12c and 4.12d it is found that cell colonization at the anode side is achieved for lower electric field strength than the case in which only the electrical stimulus is applied (4.3c and 4.3d). In fact, results provide a logarithmic relation between the

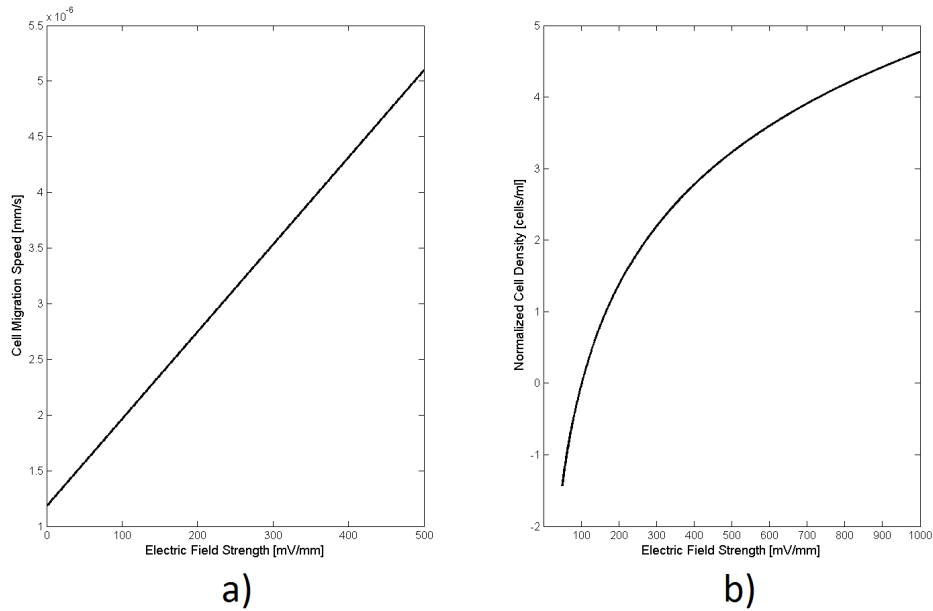


Figure 4.11: Numerical relations for cell migration directed by an electric field with a equal-sided chemical stimulus. a) Relation between the electric field and cell speed towards the anode. b) Relation between electric field and cell colonization of the anode.

electric field strength and the cell density colonization of the anode, as shown in Fig. 4.11b. According to this relation, it is found that cells arrive to the anode when an external electric field of 101.6 mV/mm is applied. It is also found that cell density at the anode increases to reach a normalized concentration value when an external electric field of 166.5 mV/mm is applied. These values represent a difference of 41.14 % and 31.28% with respect to the values obtained when only the electrical stimulus is applied (Fig. 4.3). This result suggests that when the chemical stimulus directs cell migration in equal direction than the electric field, lower electric field strength is needed for cells to reach the anode and colonize it up to a normalized cell density.

4.4.4 Forth case: Electrotaxis independent of chemotaxis

Results presented in Fig. 4.9 indicate that the electric field in the ranges of strength here used, provides an override signal for the chemical stimulus. A more detailed observation of the independence of the electrotaxis from any chemical cues has been implemented in this research following the same criteria as reported in the experimental protocols [1,5]. To this end, a forth simulation case was designed as shown in Fig. 4.1d. Results show that, even under a constant chemical flux perpendicular to the electric field vector, cells migrate towards the anode in response to the electrotaxis. This is presented in Fig. 4.13. Furthermore, measurements on cell migration after 1200 minutes yields that cell speed migration under the chemical flux equals to the case when no chemical is present, a result that can be observed when comparing the position of the cell contingent shown in Figs. 4.2a and 4.13a. Moreover, it was found that cell colonization and cell spreading over the anode after 1500 minutes (Fig. 4.13c) equals the

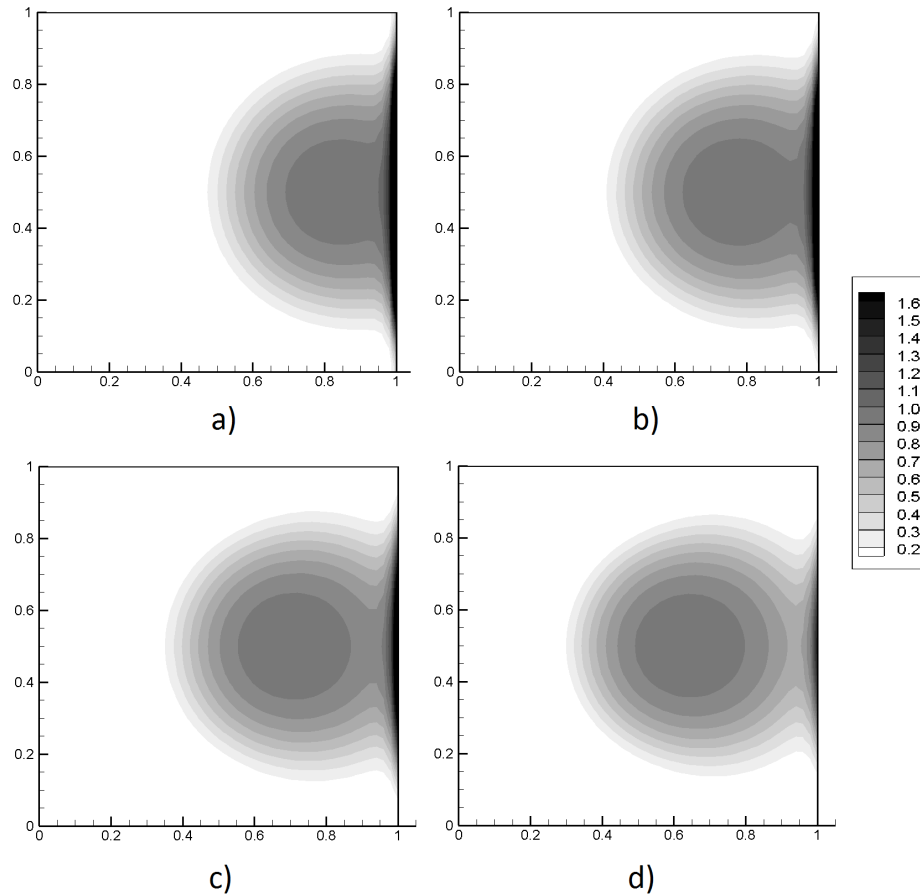


Figure 4.12: Osteogenic cell colonization (in mg/ml) of the anode after 1500 minutes of stimulation with different electric field strengths. a) $E=500$ mV/mm. b) $E=400$ mV/mm. c) $E=300$ mV/mm. d) $E=200$ mV/mm.

case where no chemical stimulus is applied (Fig. 4.3a). However, a slight movement of the cell contingent in the direction of the chemical flux was observed (Fig. 4.13c), that is caused by the drift force of the perpendicular osteogenic chemical flux.

4.5 Discussion

This paper presents a mathematical model to calculate the response of an osteogenic cells culture exposed to a static electric field. The model is based on an extension of the chemotaxis model representing cellular behaviour in the presence of a chemical signal [82, 86], and the Laplace equation for the static electric field [108]. This representation provides a framework to numerically reproduce the cell migration directed by an external electric field as experimentally observed [5, 7], in such a way that an increase in the strength of the electric field increases the rate of cell migration (Fig. 4.2). It has been numerically obtained that a change in the direction of the electric field vector changes the direction of cell migration in concor-

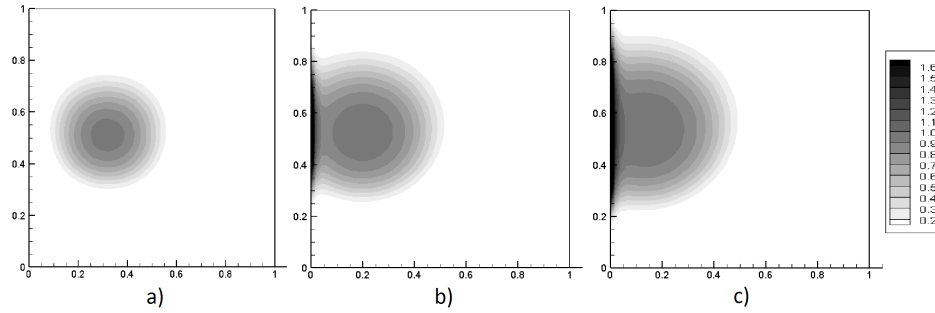


Figure 4.13: Osteogenic cell migration (in mg/ml) under a constant flux of osteogenic chemical perpendicular to the electric field vector. $E=500$ mV/mm. a) $t=700$ minutes. b) $t=1200$ minutes. c) $t=1500$ minutes.

dance with experimental reports and with the electrotaxis concept (Fig. 4.6) [1,5]. Therefore, by changing the sign of the electrotaxis term in Eq. (4.1), it is possible to reproduce cell migration towards the cathode side. This observation allow us to conclude that this behaviour may be suitable to extend the model to other biological configurations since the direction of cell migration due to electrotaxis depends on the cell type [6].

This model is based on two simplifications. The first simplification deals with an idealization of the osteogenic cells culture. As initial condition it is assumed that cellular confluence has been reached and that the cells are viable and fully differentiated into osteogenic cells. In vitro conditions such as temperature, humidity and gaseous interchange are not considered and therefore an ideal environment is assumed. The influence of the substrate on cell culture is neglected thus no cell-substrate interactions, like adhesion forces, are considered. The cellular medium is assumed to be homogeneous and no interactions between the individual cells are taken into account. This supports the simplification of the multiple proteins and growth factors needed to maintain the culture as a single osteogenic chemical signal to which cells respond.

The second simplification deals with the electrical behaviour of the osteogenic cells. It is assumed that the osteogenic cells respond to an external electric field by the mechanism of electrotaxis [5,6] and that a cellular excitation by the presence of the electric field leads to increased synthesis rates of chemical signals [8]. However, the electrical properties of the osteogenic cells and of the chemical signal are not considered in the model. Polarization effects over the cells and the chemical signal are neglected and therefore, the movement of proteins and other charged particles in the presence of the electric field is not included. It must be stated here that the main purpose of the model is to establish a numerical approach for the electric field effects on cell migration, a phenomenon well known from experimental reports [5,7,9]. Therefore, the model as described here is not intended to explore the underlying electrochemical mechanisms of electrotaxis and therefore electrical interactions of the osteogenic cells with the applied electric field are outside the scope of these work [109].

Nevertheless the abovementioned simplifications, it has been numerically found that there is an increment on cell migration speed when the osteogenic cells are exposed to a static electric field (Fig. 4.5a). In fact, it has been measured that the cell migration speed if no electric field is applied amounts to 23.54% of the speed obtained when an electric field of 500mV/mm

is applied. This value can be compared with experimental results in which differences in cell migration speed are about 50% [7]. However, it must be taken into account that the control state in the numerical approach is related to a condition where cell migration is directed by chemotaxis (Fig. 4.4) [86].

The reason for considering a control state without chemical and electrical stimuli is that we gain insight in the terms that account for cell migration as described in Eq. (4.1) and as a consequence cells remain in the centre of the domain throughout the entire simulation time. The chemical stimulus applied to the cells in the control state is taken as reference to the numerical chemical concentration produced by cells when no stimuli are applied at all [98]. Hence, the difference between the numerical and the experimental values for osteogenic cell migration speed migration when exposed to an electric field may be due to the average chemical stimulus applied to the cells. Further analysis of the chemical stimulus value may lead to changes in the chemical component of the total cell migration speed that may better correlate to the total migration pattern to the values reported elsewhere. However, and despite the differences in the cell migration rate, a control condition including a chemical stimulus should be considered as realistic as possible since cell migration is triggered by the presence of a physical stimulus inducing changes in cellular signaling mechanism [4, 110].

Another feature of the model is the reproduction of experimental observations according to which the electrical stimulus is an overriding signal for other guidance cues [5, 100]. By applying an electric field directing cell migration towards the anode together with a chemical stimulus that first directs cells migration opposite to the electric field (Fig. 4.7) and later in the same direction (Fig. 4.10), it is concluded that cell migration has a greater response to the effect of the electric field than to the chemical stimulus. Furthermore, numerical results shown in Fig. 4.7 and Fig. 4.9 yields that the electric stimulus is an overriding signal for the chemical stimulus on cell migration. This overriding effect of electrotaxis is numerically corroborated in the same way that is done in experimental research by introducing a constant chemical flux perpendicular to the electric field vector (Fig. 4.1d) [100]. The results of this implementation is as shown in Fig. 4.13 and leads to conclude using numerical support that the electrotaxis is not mediated by chemotaxis and that the electrical effects on cell migration act independently of local chemical gradients [100].

Nevertheless, it has been found that the overriding effect of the electric field is only complete when the electric field strength is higher than a certain threshold value, a behaviour shown in experimental reports and quantified for corneal epithelial cells [5, 100]. A numerical approach based on a relation found between the electric field strength and osteogenic cell migration speed (Fig. 4.8a) determines this threshold value being 34.95 mV/mm. This value is comparable in order of magnitude to the value of 12.5 mV/mm reported for corneal epithelial cells [5] and is lower than the minimal electrical stimulation value for sarcoma osteoblastic cells (SaOs-2) where this value is found to be 200 mV/mm [7]. Despite the differences, which may explained as differences between the physiology of corneal epithelial cells, SaOs-2 cells and the osteogenic cells requiring an additional adjustment of the numerical parameters of the model, results obtained are in the same order of magnitude and can be correlated to the threshold electric field strength that has been experimentally obtained

Furthermore, it has been found that the chemical stimulus has influence on the total cell speed migration towards the anode. Numerical results show that for an electric field of 500 mV/mm there is a reduction of 2% on cell migration if the chemical stimulus is opposed to the electric field. In contrary, an increase of 19.65% has been found if the chemical stimulus directs cell migration towards the anode, as resumed in table 4.5. These observations are

Stimulation	E.C. ($\times 10^{-6}$ mm/s)	C.C. ($\times 10^{-6}$ mm/s)	T.S. ($\times 10^{-6}$ mm/s)
Case 1	3.6575	0.96436	4.0959
Case 2	4.3136	-0.7399	4.0122
Case 3	3.9181	0.74108	5.0976

Table 4.2: Osteogenic cell migration speed components found for three different stimuli configurations after 1200 minutes of exposure to an 500 mV/mm electric field and a 2×10^{-2} mg/ml chemical signal. Total migration speed (T.S.) is calculated as the sum of the electrical (E.C.), chemical (C.C) and diffusive component.

in concordance with a similar behaviour observed in corneal epithelial cells [5] and provide quantification values for the change on cell migration due to the directness of the chemical stimulus, values that are not available in the reviewed literature. However, it is observed that a 2% change in the total cell migration speed when the electrical and chemical stimulus are opposed is not much significant (table 4.5) although the electrical component of cell migration speed is increased in 15.21% compared to the case when no chemical stimulus is applied. This means that osteogenic cells under this condition experience a higher electrotaxis effect than if the electric field is the only stimulus applied. Therefore, the reduced effect on the total cell migration speed up to the 2% previously mentioned is a consequence of the subtracting effect of the chemical component of the cell migration speed, opposed to the electrical component.

Despite this small difference, additional curiosity lead to use the numerical relations obtained for osteogenic cell migration speed in response to only the electric field (Fig. 4.5a) and later to only the chemical stimulus (Fig. 4.5b). The aim of these assays was to find the value for the chemical stimulus needed to impress a cell migration speed equal to that obtained when an electric field of 500 mV/mm is applied. After doing some calculations, the chemical stimulus needed is five orders of magnitude greater than the average chemical concentration used throughout the numerical simulations. Therefore, from a chemical stand point, there is no suitable way to move the cells at the same speed impressed by an electric field. Hence, the electrical behaviour of cells considered in terms of cell migration should be exploited as a possible way for reducing healing time and improving the formation of new tissues [74, 103]. Numerical simulations also provide an approach to this matter since the osteogenic cell density, when stimulated with an electric field, colonizes and spreads over a preferential electrode in a higher rate than when the cell migration is directed only by chemotaxis. This result can be observed from Figs. 4.3d and 4.4b, leading to the conclusion that an electric field strength below 200 mV/mm causes a similar colonization pattern of the anode than when an average chemical stimulus is applied.

Numerical results for cell colonization and spreading show however a reduction in the electric field strength needed for the cells to colonize the anode when an electric field is applied together with a chemical stimulus. It has been found that there is a reduction of 5.85% in the electric field needed for the osteogenic cells to reach the anode when the chemical stimulus is opposed to the electric field. There is also a reduction of 41.14% when the chemical stimulus

Stimulation	Arrival (in mV/mm)	Colonization (in mV/mm)
Case 1	172.6	242.3
Case 2	162.5	236.1
Case 3	101.6	166.5

Table 4.3: EF strengths found for the osteogenic cell to arrive and to colonize the anode side after 1500 minutes of exposure to three different stimuli configurations.

and the electric field direct cell migration in the same direction, as resumed in table 4.5. These differences can be explained considering the magnitude and direction of the electrical and chemical components of the total cell migration speed. When the chemical stimulus is opposed to the electric field, a higher electrical component of the total cell migration speed is obtained compared to the case when the only stimulus applied is the electric field. This means that there is a strong electrical effect on the osteogenic cells and therefore the electric field needed to reach the anode is lower. However, the additional load imposed by the opposed chemical stimulus reduces the total effect and in consequence the required electric field is reduced only in 6.22% (table 4.5). On the other hand, when both the chemical and electrical stimulus direct cell migration towards the anode, also a higher electrical component for the total cell migration speed is obtained. Since in this case the chemical effect increases the cell response, there is a strong total effect due to both the electrical and chemical stimulus (table 4.5) and therefore the electric field needed to colonize the anode, as resumed in table 4.5, accounts to 41.14% less than if the electric field is the only stimulus applied.

A similar behaviour reviewing the function of the chemical stimulus in the presence of an electric field has been experimentally addressed [5,100] although results are given for the total cell migration speed. The numerical approach allows splitting the total cell migration speed into three components or effects, namely the electrical, chemical and diffusive. This feature leads to better quantify the interaction between the electric field and the chemical stimulus since it has been found numerically that the electric field increases the electrical component of the total cell migration speed and therefore in may enhance cell motility in concordance with experimental observations [4,111]. Furthermore, it has been found that when the chemical stimulus is applied together with the electric field the chemical component of the total cell migration speed is reduced in 23.21% compared to the case when no electric field is applied, as resumed in table 4.5. This reduction may be considered as inhibition of chemotaxis by the electric field, a behaviour that has been also observed experimentally for bacterias [111]. Although no related effects have been reviewed for osteogenic cells behaviour, we have found that the electric field enhances the electrical component of the total cell migration speed and therefore the motility of the osteogenic cells [4]. We have also found that the chemical component of the total cell migration speed is reduced when an external electric field is also applied (table 4.5). We hypothesize that this behaviour is because the electric field increases the synthesis of signalling molecules but at the same time reduces the ability of the cell to sense the chemotaxis signalling [99]. Further research, however, from both numerical and experimental nature should be performed prior to conclude on this idea.

In addition to this results, numerical analysis has been conducted on the density of osteogenic cells colonizing the anode. The logarithmic relation found for cell colonization when no chemical stimulus is applied (Fig. 4.5b) shows a tendency for a saturation value that predicts that for an electric field of 1000 mV/mm the accumulation of osteogenic cells over the anode is a few more than five times its normalized value. Moreover, for this same electric field strength an considering a chemical stimulus opposed to the electric field, the predicted accumulation of osteogenic cells is nearly five times the normalized value (Fig. 4.8b) and when both chemical and electric stimulus orient cell migration in the same direction the accumulation is below five times the normalized value (Fig. 4.11b). According to this results, and since an electric field of 1000 mV/mm is near the maximum electric field suitable for the viability of osteogenic cells [9], the mathematical framework provides an insight to cell damage due to electric field exposure by considering that the amount of viable cells colonizing the anode is reduced when the electrical sensitivity of cells related to the electrical component of the total cell migration speed is enhanced with the activity of the chemical component. According to this, it is proven by using a numerical approach that the osteogenic cells have an *electrochemical response* because the application of an electric field increases their cell migration speed and a chemical stimulus may act a control to this increased cell migration speed, behaviour that has been observed experimentally [5, 103].

Despite the differences given by the presence and behaviour of the chemical effect, it has been found that an electric field increases cell colonization and cell spreading over the anode in the same way that cells colonize and spread over certain substrates due to its surface topography and biocompatibility [16, 20]. This effect, or osteoconduction, allows for tissue formation in direct contact with surfaces made of non-biological materials and is the base for wound healing and anchorage of implants [16].

Since the application of an electric field leads to an increment on cell density over the anode side and this cell density can be mediated by the strength of the electric field as shown in Figs. 4.5b, 4.8b and 4.11b, it is feasible to conclude that a so-called *electro-osteoconduction* phenomenon may increase the rate of tissue formation over a given substrate and therefore by using an electrical stimulus, it may reduce healing times and improve tissue formation around implants, as experimentally reported elsewhere [11, 112].

CHAPTER 5

MODELING BLOOD CLOTTING IN THE PRESENCE OF AN ELECTRICAL STIMULUS

5.1 Introduction

A successful osseointegration, i.e., the formation of stable and functional bone at the bone-implant interface, cannot be obtained in the absence of a proper initial stability of the implant [16,36]. Although mechanical factors dominate this initial stability, it is accepted that controlled bleeding and suitable formation of soft tissues at the interface keeps the implant in place [19,25]. Since the biological process of blood clotting comprises a chain of complex biomolecular events mediated by the presence of different types of cells and chemical molecules [48,49], the control of the blood clot formation is typically achieved by using chemical reactions that accelerate the clotting phase [113]. However, findings on the electrical behaviour of the blood elements have shown that blood clot formation can be also induced by the application of an external electric signal [104,114]. Therefore, it is possible to induce thrombus formation to occlude arteries, veins and vascular anomalies by applying a static electric field, a process known as *electro-thrombosis* [104]. It is also possible to count the number of available platelets in a blood sample by using an electrical stimulus as is done during the electrical aggregometry test [58].

Although most of the knowledge has been obtained using experimental assays, mathematical models and computational simulations have proved helpful in providing additional information on this type of interactions, especially during healing processes [15,68]. Accordingly, a mathematical formulation for the formation of the fibrillar network that finally detains the blood loss after the implant placement was previously introduced [68]. In that formulation, the Law of Mass Action was used to mathematically describe the kinetic reaction between thrombin and fibrinogen, the two most important blood proteins governing the conversion mechanism that creates the fibers of the final blood clot [48]. Based on that description, in this work we introduce a modified form of the mathematical formulation for the blood clot formation including terms that represent the influence of an external electrical stimulus in both the kinetic reaction between thrombin and fibrinogen, and the formation of the final

fibrillar network.

The formulation of these new terms is based on the hypothesis that due to the electrical charges of thrombin, fibrinogen and platelets, an external electrical stimulus increases the conversion of fibrinogen into fibrin [114] and might create a preferential site for an increased fibrin fibers formation [57]. Indeed, by considering a static electric field (EF) as the stimulus, fibrin formation is higher near the positive electrode [58]. Numerical results show that blood clot formation is increased near the positive electrode of the applied stimulus, in agreement with experimental observations [114]. Furthermore, the numerical results allow us to quantify the increase in blood clot formation in the presence of an EF. Accordingly, it is concluded that the blood clot density can be controlled not only by the concentrations of molecules and cells governing the clotting reactions [113], but also by the strength of the electrical signal [105].

5.2 Blood clotting and electrical stimulation

Blood clotting is part of the mechanism of haemostasis, which ensures the integrity of the vascular network even after an injury has occurred [48]. In such a case, blood loss triggers blood clotting together with the vasoconstriction of the damaged vessels to reduce the blood infiltration. In addition, the platelets present in the poured blood localize and aggregate forming an initial plug that also helps detain the blood loss [48, 49]. With the injury of a blood vessel a series of blood molecules, called *coagulation factors*, are activated [48]. The complex and organized reactions between the coagulation factors come together in a conversion mechanism which transforms the poured blood into a fibrillar network that in turn brings support to the aggregated platelets and completely stops the blood loss [50].

The reactions leading to blood clotting can be reduced into two pathways. The first one is the *intrinsic pathway*, which is activated when the blood transported by the vascular network gets in contact with the sub-endothelial environment [48]. The second is the *extrinsic pathway*, which is activated as a consequence of a vascular injury that in turn induces a biochemical response from the damaged tissues [12]. After a series of other chemical reactions, these two pathways converge at the so-called *common pathway* [48, 49], which is associated with the formation of the *fibrin clot* and depends on the conversion of *prothrombin* [50]. During this conversion, the inactivated blood plasma prothrombin is transformed into *thrombin*, which interacts with the plasma *fibrinogen* splitting off the molecule in a kinetic reaction to form small fibers of *fibrin*. These small fibers or monomers then aggregate and form larger fibers making up a fibrillar network that permeates the entire injured area [12, 50].

A number of conditions may influence the formation of the fibrin network. The activation/inhibition of the chain of reactions preceding the formation of fibrin monomers is by far the most observed [49, 115]. Accordingly, the inhibition of the prothrombin conversion and the inactivation of thrombin reduces fibrin formation, as used in anticoagulation applications [49]. Additionally, the activation of platelets releasing cytoplasmatic granules rich in fibrinogen [49] (yet another mechanism normally involved during blood clotting) can be affected by blood diseases which induce variations in the number of available platelets in the blood stream, as is the case of thrombocytosis and thrombocytopenia [116].

An additional controlling mechanism for fibrin formation is afforded by the application of an external electrical signal. It is known that the fibrinogen molecule has a negative charge [57] whereas the thrombin molecule has a positive charge [117]. Experimental reports show that platelets also have a negative charge and as a consequence, they accumulate (and aggregate)

at the surface of a positive charged electrode [104]. By connecting a direct power source to two electrodes in contact with a blood plasma sample, it was observed that most of the positive electrode was covered with a blood clot, whereas the negative electrode was clot-free [114]. Hence, the activation of the blood clot process, and the direction of migration of both thrombin and fibrinogen can be electrically controlled. We hypothesize that the kinetic reaction that converts fibrinogen into fibrin is electrically mediated in such a way that higher fibrin densities might be obtained at the positive electrode. This provides a preferential blood coagulation site and a possible control mechanism for blood clotting, the initial stage in the sequence which leads to wound healing and osseointegration of a dental implant.

5.3 Mathematical model

The blood clot process is simplified as the kinetic reaction between thrombin and fibrinogen [48]. Since the presence of an electrical stimulus increases the activity of the conversion reaction [58, 104], a mathematical description accounting for the electrical behaviour of the blood clotting process is introduced. The model comprises four variables: 1) the thrombin concentration ($T(\mathbf{x}, t)$), 2) the fibrinogen concentration ($F(\mathbf{x}, t)$), 3) the fibrin density ($f(\mathbf{x}, t)$) and 4) the electric potential ($V_e(\mathbf{x})$), with \mathbf{x} a position vector in the x, y plane, and t the time. Each one of these variables is mathematically described as follows:

Thrombin

The reaction-diffusion equation that describes the thrombin concentration reads

$$\frac{\partial T}{\partial t} = \nabla \cdot (D_T \nabla T - T E_T \nabla V_e) + k_1 P - k_2(V_e) T F^2 - k_3 T. \quad (5.1)$$

The flux of thrombin is considered as a random dispersal mechanism. It is modeled as a linear diffusion term with coefficient D_T . An additional term with anisotropic coefficient E_T (with value different from zero only in the direction of the applied electrical stimulus) accounts for the electrical dispersion of thrombin due to its electric charge [117]. Accordingly, the negative sign indicates migration towards the negative electrode. Since thrombin is obtained through prothrombin conversion [118], the production term with coefficient k_1 is related to the prothrombin concentration P . The transformation mechanism is given by a non-linear term with electric potential-dependent coefficient $k_2(V_e)$. This coefficient is expressed as $k_2(1 - c_1 V_e)$, where k_2 is the transformation parameter [68], and the term $(1 - c_1 V_e)$ mediates the electrically controlled transformation mechanism using the anisotropic coefficient for thrombin c_1 . The negative sign accounts for the reduced thrombin concentration in the areas for which the electric potential is positive, i.e., larger amounts of thrombin are used by the transformation mechanism near the positive electrode [114, 117]. A linear consumption term with coefficient k_3 complements the equation.

Fibrinogen

The reaction-diffusion equation used for the fibrinogen concentration reads

$$\frac{\partial F}{\partial t} = \nabla \cdot (D_F \nabla F + F E_F \nabla V_e) + k_2(V_e) T F^2 + k_3 T + k_4(V_e) G - k_5 F. \quad (5.2)$$

Fibrinogen is considered as a random dispersal substance with a linear diffusion term with coefficient D_F . The electrical dispersion due to the negative charge of fibrinogen is controlled by the anisotropic coefficient E_F . The positive sign indicates that the electrical attraction is towards the positive electrode. A nonlinear term with coefficient $k_2(V_e)$ controls the transformation mechanism. This coefficient is expressed as $k_2(1 + c_2 V_e)$, where k_2 is the transformation parameter [68], and $(1 + c_2 V_e)$ is the electrically controlled transformation mechanism mediated by the anisotropic coefficient for fibrinogen c_2 . The positive sign indicates an increase in the transformation reaction in the areas where the electric potential is positive, i.e., larger amounts of fibrinogen are available for the conversion into fibrin near the positive electrode [57, 114]. The fibrinogen production is associated with the presence of thrombin through the coefficient k_3 . An additional production term with coefficient $k_4(V_e)$ is related to the concentration of granules G released by the activated platelets that also contain fibrinogen [49]. Since platelet activation can be electrically controlled [58], the coefficient $k_4(V_e)$ is expressed as $k_4(1 + c_3 V_e)$, where k_4 is related to the fibrinogen released by the activated platelets [68, 118], and the term $(1 + c_3 V_e)$ is a secondary fibrinogen release mediated by the anisotropic coefficient c_3 related to the electrical activation of platelets and the consequent granules release [58]. Finally, the fibrinogen consumption is modeled by a linear term with coefficient k_5 .

Fibrin

The relevant equation is

$$\frac{\partial f}{\partial t} = \left[\frac{\alpha f_{max} [1 - e^{-(\alpha t + \beta f + \beta_e V_e f)}]}{1 - (\beta + \beta_e V_e) f_{max} e^{-(\alpha t + \beta f + \beta_e V_e f)}} \right] \left(\frac{W^p}{f^p + W^p} \right). \quad (5.3)$$

The kinetic reaction between thrombin and fibrinogen leads to the conversion of fibrinogen into a network of *fibrin fibers* [48, 50]. This conversion is modeled by means of an exponential term controlled by three coefficients. The coefficient α is related to the formation rate of fibrin fibers [50]. The coefficient β correlates the number of activated platelets and the concentration of fibrinogen released by them [119]. The coefficient β_e represents the accumulation and activation at the positive electrode of the negatively charged platelets when exposed to the EF between a pair of electrodes [104]. The amplitude of the exponential is controlled by the parameter f_{max} , viz., the experimental value of fibrin concentration [71]. The conversion pattern is transmitted from fibrinogen to fibrin by means of an activation function with threshold value W and slope p .

Electric potential

The electric potential must satisfy the Laplace's equation in Eq. (4.3). As in Chapter 4, the net charge inside the bone-dental implant interface is zero. This is realistic because cells and tissues show dielectric properties [4], and we neglect the endogenous currents and EFs

created by the disruption of the integrity of cells and tissues after an injury [1]. Similarly to the reason exposed in Chapter 4, only static potentials are considered for this model.

5.4 Description of the simulation

The numerical solution of Eqs. (5.1) - (5.3) is carried out by means of the finite elements method with a Galerkin approximation for the spatial discretization combined with the backward-Euler approach for the time discretization [95]. The solution was implemented in a bi-dimensional domain representing a section of the interface created between the implant surface and the host bone border [120], discretized into 9 132 quadrilateral patches and 9 350 nodes (Fig. 5.4).

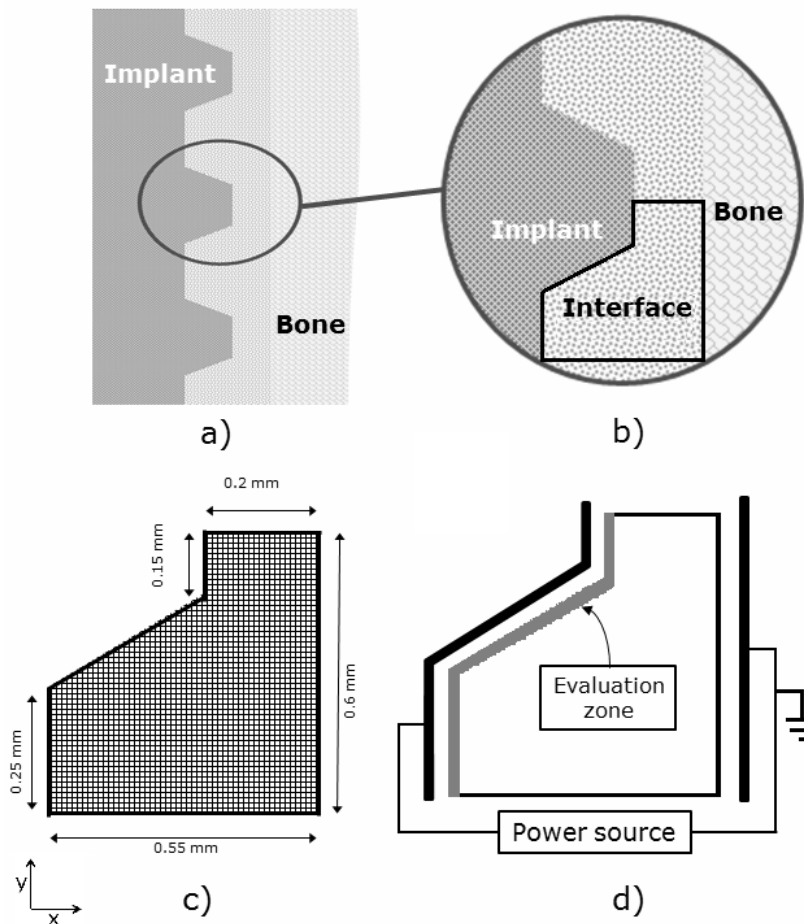


Figure 5.1: a) - b) The bone-dental implant interface. c) Simulation domain. d) Connection of the ideal power source and outline of the *evaluation zone*.

Eqs. (5.1) and (5.2) were implemented in a dimensionless form as described in the Appendix A.2.1. This was done to reduce the kinetic reaction between thrombin and fibrinogen into a modified form of the glycolysis model used in morphogenesis applications [82,98]. Thus, initial conditions for both thrombin and fibrinogen correspond to small perturbations of the

steady-state concentration observed for the variables of the glycolysis model [98]. The initial condition for fibrin is null since the fibrin network is a product of the kinetic reaction between thrombin and fibrinogen. The initial state for the electric potential is equal to zero.

Flux conditions at the contours of the domain for Eqs.(5.1) - (5.3) are set to zero. Accordingly, no blood influx into the domain is considered. Besides, the formation of the fibrin clot is assumed to be carried out only by the thrombin and fibrinogen transported by the blood which pours in the bone-dental interface from the moment the implant is inserted into the bone (breaking of the blood vessels) until the formation of the activated platelets plug which initially stops the blood loss [48].

Four scenarios were simulated, each one characterized by a different electric field (EF) strength, namely, 0, 250 mV/mm, 500 mV/mm and 750 mV/mm [7,9]. The EF stimulation was implemented assuming that an electrical device built inside the dental implant creates a static EF between the implant surface and the host bone surface which is connected to ground. To reproduce this, two ideal parallel electrodes are connected to an external power source, as shown in Fig. 5.4d. The electric potential is obtained by solving the two-dimensional problem described by Eq. (4.3) with the corresponding boundary conditions. Specifically, the potential at the boundary representing the host bone was set to zero, whereas at the boundary representing the implant surface it was set in each case to the desired EF strength times the lower width of the domain (0.55 mm). A so-called *evaluation zone* (Fig. 5.4d) was defined by considering all the elements located 5 μm away from the implant surface [68,121] to enable evaluating the fibrin formation at the different simulation scenarios.

The simulations were done for 1 000 time steps corresponding to a total real-time of ten minutes, i.e., the time needed for the fibrin network to consolidate the final plug at the bone-dental implant interface [51]. The values of the parameters used in Eqs. (5.1) - (4.3) were obtained from literature. In cases where no information was available, numerical experimentation was used to obtain consistent spatial-temporal patterns. Table 5.4 summarizes the values finally used in the simulations. Further information about these parameters can be found in Appendix A.2.2.

5.5 Results

A first simulation was performed to evaluate the model when no EF is applied. In this case, the fibrin network formation is the consequence of the transformation mechanism only. The results are shown in Fig. 5.5. Initially, there is no kinetic reaction and hence no fibrinogen has been converted into fibrin, as observed in Fig. 5.5a. After 2 minutes, the kinetic reaction has started, fibrin fibers are being assembled, and a fibrillar pattern appears throughout the domain (Fig. 5.5b). This assembling mechanism continues forming the fibrin fibers after 10 minutes (Fig. 5.5c). The concentration values shown correspond with values reported for the fibrin density of the fibrillar network up to a maximal value of 2.5 mg/ml [68,71].

Next, three different simulation scenarios have been implemented to evaluate the effect of the EF in the fibrin network formation. In the first scenario, an EF of 250 mV/mm is applied to the bone-dental implant interface. In this case, the fibrin network formation shows a similar time evolution pattern as in the case when no EF is applied. However, the density of the fibrillar pattern near the implant surface after 10 minutes exhibits a slight increase as shown in Fig. 5.5b, as compared to the case without EF (Fig. 5.5a). This increase is explained by the electrical activity of both thrombin and fibrinogen described by the complementary

Parameter	Value	Units	Reference
D_T	5.0417×10^{-4}	$\text{mm}^2 \text{ s}^{-1}$	[68]
D_F	5.647×10^{-5}	$\text{mm}^2 \text{ s}^{-1}$	[68]
E_T	1.8×10^{-3}	$\text{mm}^2 (\text{V s})^{-1}$	N.E.*
E_F	1.8×10^{-3}	$\text{mm}^2 (\text{V s})^{-1}$	N.E.*
k_1	2.0×10^{-3}	s^{-1}	[68]
k_2	1.7×10^{-3}	$(\text{s (mg/ml)}^2)^{-1}$	[68]
k_3	1.0×10^{-3}	s^{-1}	[68]
k_4	50×10^{-6}	s^{-1}	[68]
k_5	1.7×10^{-3}	s^{-1}	[68]
c_1	0.3636	V^{-1}	N.E.*
c_2	0.3636	V^{-1}	N.E.*
c_3	0.4627	V^{-1}	N.E.*
f_{max}	2.5	mg/ml	[71]
α	0.5	s^{-1}	[50]
β	0.37	$(\text{mg/ml})^{-1}$	[68]
β_e	0.02	$(\text{V mg/ml})^{-1}$	N.E.*

* N.E. = Numerical Experiment.

Table 5.1: Parameter values for the mathematical model of blood clotting

terms in Eqs. (5.1) and (5.2), and the additional platelet aggregation obtained with the presence of the EF [58].

These two effects are enhanced at higher EF strengths. Therefore, the application of an EF of 500 mV/mm (second scenario) yields a more conspicuous increase of the fibrin density near the implant surface after 10 minutes (Fig. 5.5c). An even higher fibrin density is observed for the third case when an EF of 750 mV/mm is applied (Fig. 5.5d). As a consequence of the higher fibrin density, the fibrillar pattern is denser near the implant surface. This means that the distance between the fibers is reduced and in consequence the individual fibers are no longer observable.

Additional results plotted in Fig. 5.5 attest the increased fibrin formation near the implant surface after 10 minutes. Fig. 5.5a shows the fibrin density along a straight line parallel to the bottom of the domain and crossing the vertical axis at 0.1 mm height. When no EF is applied, the fibrin density in the domain shows no clear trend and is around 1.7 - 1.8 mg/ml in average. However, when the EF is applied, the fibrin density near the implant surface increases with the EF strength. In fact, for an EF of 750 mV/mm, an exponential like pattern is obtained. For this case, a maximum density of 2.24 mg/ml is achieved 4 μm away from the implant

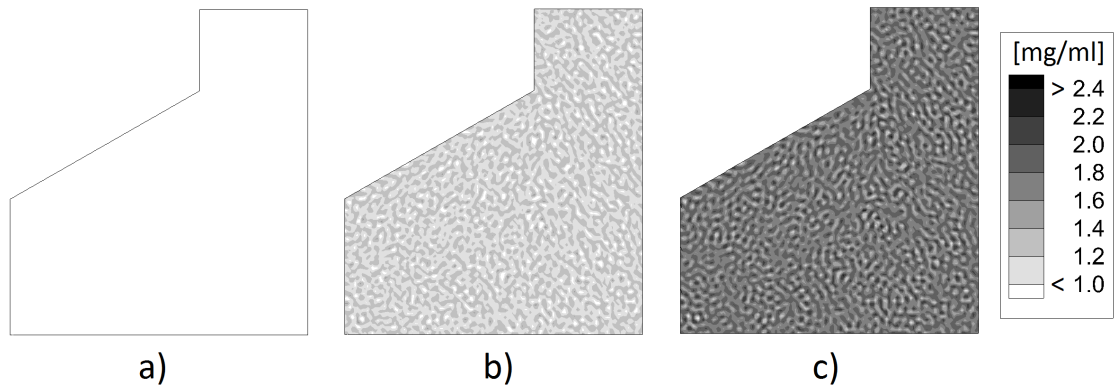


Figure 5.2: Fibrin network formation when no EF is applied. a) $t = 0$ min. b) $t = 2$ min. c) $t = 10$ min.

surface.

Interestingly, in all the four simulation scenarios, the fibrin density at the host bone surface (negative electrode) takes on a value around 1.8 mg/ml. This fact is an indication that the EF influences fibrin formation only near the positive electrode, as experimentally reported [114].

Furthermore, the influence of the EF in the fibrin network formation time was assessed by calculating at every time step the average fibrin density for the elements at the so-called *evaluation zone* (Fig. 5.4d). Fig. 5.5b shows the results. When no EF is applied, the time evolution of the fibrin network follows a damped exponential growth with a maximum value after 10 minutes of exposure equal to 1.7525 mg/ml. In addition, the fibrin density reaches a value of 1 mg/ml after 41 seconds. When the EF is applied, the same exponential behaviour is obtained although different maximum values and times are obtained. In the case of an EF of 250 mV/mm, the maximum fibrin density is 1.9791 mg/ml, which represents an increase of 13 % with respect to the case with no EF. Moreover, the time needed to reach a fibrin density of 1 mg/ml is reduced to 30 seconds, meaning that the application of an EF of 250 mV/mm speeds up the fibrin conversion rate by 27 %.

Similarly, when an EF of 500 mV/mm is applied, the maximum fibrin density is 2.1362 mg/ml whereas for an EF of 750 mV/mm the maximum value is 2.2453 mg/ml. These results represent increases of 22 % and of 28 % with respect to the case with no EF. In turn, the time needed by the fibrin density to reach 1 mg/ml is 24 seconds and 22 seconds respectively. Hence, the application of an EF of 500 mV/mm reduces the fibrinogen conversion time by 41 %, whereas an EF of 750 mV/mm by 46 %.

5.6 Discussion

Numerical results show that the blood clot formation at the bone-dental interface is a process than can be controlled by an electrical stimulus. The working hypothesis for the electrical interaction is validated by the results obtained for different EF strengths. It is demonstrated that higher EF strengths cause larger fibrin densities near the positive electrode, i.e., the implant surface (Fig. 5.5). It is believed that such increase may be accompanied by a higher fiber attachment to the implant surface. When immature bone cells start to migrate towards

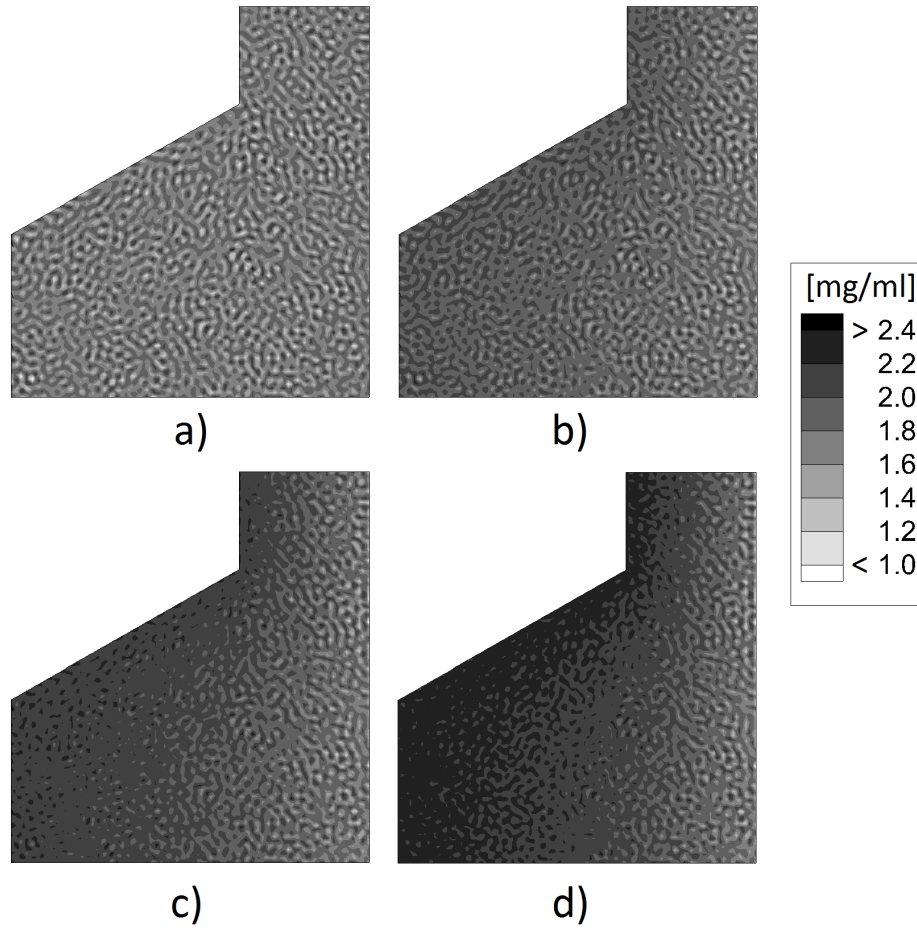


Figure 5.3: Fibrin formation after 10 minutes of exposure to different EF strengths. a) EF = 0. b) EF = 250 mV/mm. c) EF = 500 mV/mm. d) EF = 750 mV/mm.

the implant surface, they use the fibrillar network as support [12, 36]. Some of these fibers are attached to the implant surface allowing the cells to synthesize new tissue directly over it [36]. However, cell migration exerts a contractile force on the fibers that may detach some of these fibers from the implant surface. This condition creates a gap between the implant surface and the healing front causing implant failure due to the lack of osseointegration [20]. Numerical results demonstrate that the presence of an electrical stimulus at the bone-dental implant interface might be a way for reducing this gap by increasing the fibrin formation near the implant surface. Such increase may induce a larger number of fibers attached to implant which lead in consequence to an increased rate of bone formation at the interface, as experimentally reported [11, 61].

It is observed that with EFs of 500 mV/mm and 750 mV/mm, the fibrillar formation near the implant surface has a homogeneous pattern (Fig. 5.5). This can be understood as an increased fiber formation up to the point that the distance between two adjacent fibers is shorter than the mesh edge. A similar result is obtained when a higher-than-normal number of platelets typical of thrombocytosis (1×10^{12} cells/l) is used and no EF is applied [68]. Accordingly, a denser fiber network near the implant surface in the presence of an EF can

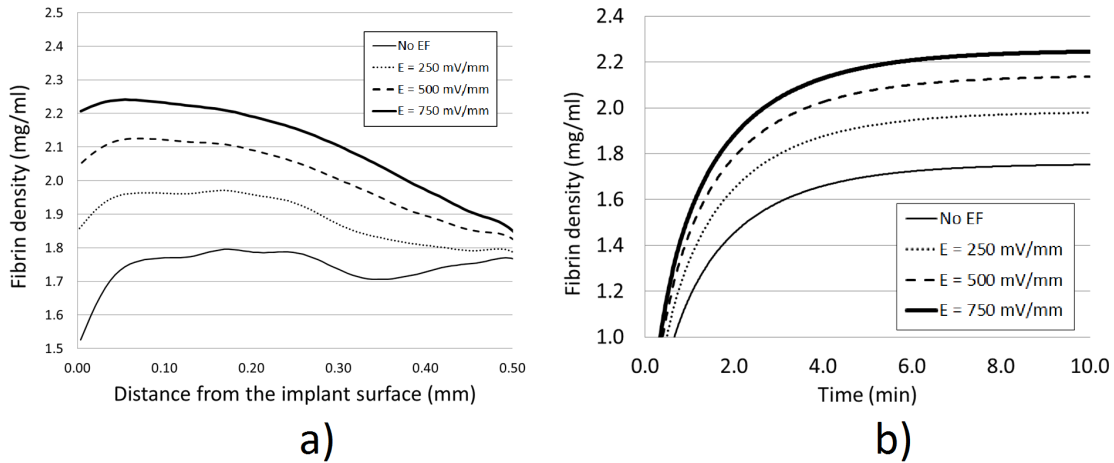


Figure 5.4: Fibrin formation when exposed to different EF strengths. a) Related to the distance from the implant surface, and b) related to time.

be correlated to a larger number of activated platelets. Since platelet activation is mediated by irregularities in the implant surface [122], numerical results lead to the conclusion that (near the implant surface) applying an EF during blood clotting produces the same biological outcome as a rough implant surface.

Furthermore, numerical results shown in Fig. 5.5b demonstrate that the electrical stimulation reduces the time of the fibrillar network formation. It is believed that a faster network formation may trigger a faster cell migration over it. A consequently faster formation of new tissues at the bone-dental implant interface may reduce the healing time and improve its osseointegration [61]. However, results also show that the time needed to form a fibrin network with a density of 1 mg/ml near the implant surface does not change much if the EF is increased from 500 mV/mm to 750 mV/mm (Fig. 5.5b). This behaviour suggests a saturation in the speed rate of the fibrin formation mechanism. The maximum value can be related to the physical limit to EF stimulation (close to 1 000 mV/mm), posed by the maximal EF strength that cells can withstand before being electroporated and dying [7]. Therefore, the numerical results show effects of the EF below the maximal strength, thus ensuring the biological relevance of the findings.

In conclusion, the model reproduces known features of the influence of an electrical stimulus in the blood clot formation and shows increments in the fibrin formation relative to the strength of the electrical stimulus [57, 117]. The numerical results make the model a suitable starting point for a general description of the biological process of bone formation at the bone-dental interface in the presence of an EF, which is presented in the next chapter.

CHAPTER 6

NUMERICAL SIMULATION OF ELECTRICALLY STIMULATED OSTEOGENESIS

6.1 Introduction

Based on initial researches conducted in the 1800's, it is recognized that biological tissues and especially bone have a characteristic electrical behavior [1]. In the presence of a compression load, bone response with an electronegative potential that stimulates new bone deposition. In contrast, when tension is applied, an electronegative potential inducing bone resorption is obtained [2]. The control of this EF-mediated osteogenic behavior is the base for bone electrostimulation [3]. It is known that EF modulates the activity of osteoblasts and osteoclasts, but also of keratinocytes, fibroblasts, myocytes, endothelial cells and nervous cells [60]. Therefore, the beneficial effects of electrostimulation observed in bone have also been observed in cartilage, ligament, muscle and skin [5, 8].

Since an electric field seems to replace the metabolic activity induced by the mechanical action of gravity and one's body weight, electrostimulation has useful applications for the prevention of bone loss during immobilization procedures, prolonged stays in bed, and space shuttle missions [24, 60]. Nevertheless, although there is no general consensus about the underlying biological and mechanical processes influenced by external electric stimuli, several electrostimulation devices are available on the market, and the use of electric-based treatments is common within health institutions [2].

Recently, mathematical models and numerical simulations have provided additional information about the interaction between proteins, cells, tissues and EF during the healing process concerning bone formation [14, 27, 106]. These models are able to describe and quantify cell migration and proliferation in the presence of chemical, mechanical and electrical stimulus, [14, 88, 106, 123].

This chapter is aimed at introducing a mathematical model for electrically stimulated bone formation or osteogenesis [2, 3] at the bone-dental implant interface. The model consists of a set of coupled partial differential equations which describe blood clotting, cell migration, granulation tissue formation and new bone matrix formation. The equations are solved

numerically using the finite elements method in a bi-dimensional domain which represents a section of the bone-dental implant interface. The numerical results describe the relation between the biological events, the implant surface and the EF leading to osteogenesis at the interface. They also represent a combination of computational mechanobiology [102, 106], with the electrical response of the new tissues at the healing site.

6.2 Mathematical model

Bone formation at the bone-dental implant interface is the result of complex biological, biochemical and mechanical events involving different types of cells and molecules [12, 13, 31, 37]. For the formulation of our model we rely on a simplified description of these events, which are detailed in Chapter 2. Accordingly, the biological process leading to bone formation is reduced to four successive stages [12, 31]: 1) bleeding and blood clotting, 2) fibrinolysis, 3) fibroplasia, and 4) osteogenesis.

Several biological mechanisms of the bone-dental implant healing process are known to be influenced by an EF. However, the mathematical description accounts only for the most significant elements (see Fig. 2.3). More specifically, the model first describes blood clot formation as the consequence of a kinetic reaction between *thrombin* ($T(\mathbf{x}, t)$) and *fibrinogen* ($F(\mathbf{x}, t)$) to produce *fibrin* ($f(\mathbf{x}, t)$) [48]. After formation of the fibrin network, the *osteogenic cells* ($C_o(\mathbf{x}, t)$) start migrating towards the implant surface. The assumption of a single cell contingent neglects the presence of different cell types during wound healing, especially macrophages, fibroblasts and osteoblasts [12, 36]. Cell migration is assumed to occur in response of an *osteogenic chemical* ($Q_o(\mathbf{x}, t)$), representing the complex set of growth factors, proteins and other molecules present during cell migration and proliferation [47]. As a consequence of cell migration, the fibrillar network is replaced by *granulation tissue* ($G(\mathbf{x}, t)$).

Since cell migration contracts the fibrillar network [13], the *displacement* ($U(\mathbf{x}, t)$) of the matrix is introduced in order to identify the possible detachment of fibers from the implant surface [36]. Then, the bone formation or *osteogenesis* ($B(\mathbf{x}, t)$) is started. Both direct and contact osteogenesis are implemented by considering the implant *surface roughness* as a numerical parameter (R_S) with extremal values equal to one (zero) to represent a rough (smooth) surface. The bone-dental implant interface is assumed to be placed between two plates connected to a DC power source. Therefore, the electrical stimulus is given as the electric potential ($V_e(\mathbf{x})$) across the interface.

The model equations are detailed in what follows. Some numerical parameters are considered as anisotropic, meaning that their values are different from zero only in the direction of the EF between the two plates. This assumption better models the influence of EF on cells and molecules during electrotaxis [5, 6].

Thrombin

The equations for thrombin and fibrinogen are a modified form of the glycolysis model used to represent stripe-like spatial temporal patterns [68, 83]. The thrombin concentration is modeled via a reaction-diffusion equation given as

$$\frac{\partial T}{\partial t} = \nabla \cdot (D_T \nabla T - T E_T \nabla V_e) + k_1 P - k_2 (V_e) T F^2 - k_3 T, \quad (6.1)$$

where D_T is the diffusion coefficient and E_T is the anisotropic electrical dispersion. The negative sign indicates migration towards the negative electrode, since thrombin carries positive electrical charge [117]. Thrombin production is modeled as the prothrombin P conversion into thrombin [118] with coupling coefficient k_1 . The non-linear term represents the transformation mechanism between thrombin and fibrinogen, with $k_2(V_e) = k_2(1 - c_1V_e)$ where k_2 is the transformation parameter [68], $(1 - c_1V_e)$ is the electrical mediation, and c_1 is the anisotropic electrical control coefficient for thrombin. Its negative sign accounts for lower thrombin concentration near the positive electrode, which can also be understood as a higher amount of thrombin used in the transformation mechanism [114,117]. Finally, thrombin decay is modeled by a linear term with coefficient k_3 .

Fibrinogen

Similarly to thrombin, the fibrinogen concentration is modeled via a reaction-diffusion equation that reads

$$\frac{\partial F}{\partial t} = \nabla \cdot (D_F \nabla F + F E_F \nabla V_e) + k_2(V_e) T F^2 + k_3 T + k_4(V_e) P - k_5 F, \quad (6.2)$$

where D_F is the diffusion coefficient and E_F is the anisotropic electrical dispersion. The positive sign represents the attraction towards the positive electrode in view of the negative electric charge of fibrinogen [57]. The non-linear term $k_2(V_e) = k_2(1 + c_2V_e)$ represents the transformation mechanism with k_2 the transformation parameter [68], $(1 + c_2V_e)$ the electrical mediation, and c_2 the anisotropic electrical control coefficient for fibrinogen. Its positive sign accounts for higher amounts of fibrinogen near the positive electrode [57, 114]. Fibrinogen production in the presence of thrombin is described through the coupling coefficient k_3 . Additional production is related to the fibrinogen contained in the granules P released by the activated platelets [49]. More precisely, $k_4(V_e) = k_4(1 + c_3V_e)$, k_4 related to the fibrinogen released by the activated platelets [68, 118], $(1 + c_3V_e)$ the electrical mediation, and c_3 the electrical control coefficient for platelet activation [58]. Finally, fibrinogen decay is modeled by a linear term with coefficient k_5 .

Fibrin

The conversion of fibrinogen creates a *fibrin fibrillar network* [48, 50]. The formation of this network is modeled by using the exponential mechanism

$$\frac{\partial f}{\partial t} = \left[\frac{\alpha f_{max} [1 - e^{-(\alpha t + \beta f + \beta_e V_e f)}]}{1 - (\beta + \beta_e V_e) f_{max} e^{-(\alpha t + \beta f + \beta_e V_e f)}} \right] \left(\frac{W_F^n}{f^n + W_F^n} \right), \quad (6.3)$$

where α is the fibrin activation rate [50, 68], β the blood quality factor related to the number of activated platelets and the concentration of fibrinogen released by them [49], and β_e the electrical blood factor related to the activation of the negatively charged platelets that accumulate near the positive electrode [104]. f_{max} is the maximum fibrin concentration [71]. W_F and n are the threshold and the slope of the activation function transmitting the fibrinogen transformation pattern to the fibrillar formation.

Osteogenic cells and chemical

The osteogenic cell migration in response to both chemical and electrical stimuli is modeled by using a modified form of the chemotaxis model [86, 123], namely,

$$\begin{aligned} \frac{\partial C_o}{\partial t} = & \nabla \cdot [D_{C_o} \nabla C_o - H_{C_o} C_o \nabla Q_o - E_{C_o} C_o \nabla V_e] \\ & + r_{C_o} C_o \left[1 - \frac{C_o}{C_i} \right] \left[\frac{Q_o^n}{Q_o^n + W_{Q_o}^n} \right] - \delta_{C_o} C_o, \end{aligned} \quad (6.4)$$

$$\frac{\partial Q_o}{\partial t} = D_{Q_o} \nabla^2 Q_o + (r_{Q_o} + r_{V_e} V_e) C_o + r_{QD} \left(\frac{f^n}{f^n + W_f^n} \right) - (\delta_{Q_o} + \delta_{QC} C_o) Q_o, \quad (6.5)$$

where D_{C_o} and D_{Q_o} are the diffusion coefficients for both the cells and the chemical, H_{C_o} is the chemotactic sensitivity of the cells, and E_{C_o} is the anisotropic electrical sensitivity coefficient [123]. Its negative sign indicates cell migration towards the positive electrode [7]. Cell proliferation is modeled assuming a logistic growth [86] with coefficient r_{C_o} . C_i is the cell saturation value [86]. W_{Q_o} and n are referred to the threshold and slope of an activation function for cell migration in the presence of a minimum chemical stimulus [86]. r_{Q_o} and r_{QE} refer to the chemical production, the former being the chemical released by the cells during migration and proliferation [36], and the latter the increased chemical production in the presence of the EF [124]. Finally, r_{QD} refers to the chemical released by the activated platelets [48], which accumulate at higher fibrin formation sites [49].

Granulation tissue

The fibrin network replacement into granulation tissue is modeled using the reaction equation

$$\frac{\partial G}{\partial t} = [r_G F + r_{GE} G V_e - \delta_G G] \left[\frac{C_o^n}{C_o^n + W_{C_o}^n} \right]. \quad (6.6)$$

Since the fibrin fibrillar network is transmitted from fibrinogen, and new tissue is formed along the fibrin fibers [12, 13], the granulation tissue formation is initiated with the presence of fibrinogen, coupled with the coefficient r_G . An increased tissue formation observed during EF exposure [60, 125] is modeled as a linear term with coefficient r_{GE} . Tissue degradation is coupled via the coefficient δ_G . W_{C_o} and n are the threshold and the slope of an activation function related to the minimum cell density needed to produce the granulation tissue.

Displacement of the matrix

The displacement of the fibrillar network due to cell migration [36] is modeled by using the viscoelastic properties of fibrin [71] and the equilibrium force equation given by

$$\nabla \cdot \left\{ \left[\frac{E}{1+\nu} \left(\mathbf{e} + \frac{\nu}{1-2\nu} \Theta \mathbf{I} \right) \right] + \left[\mu_1 \frac{\partial \mathbf{e}}{\partial t} + \mu_2 \frac{\partial \Theta}{\partial t} \mathbf{I} \right] + \left[\frac{\tau_{C_o} C_o}{1 + \lambda_{C_o} C_o^2} \mathbf{R} \right] \right\} = 0, \quad (6.7)$$

where E and ν are Young's and Poisson's moduli for fibrin, μ_1 and μ_2 are Lamé's coefficients, and \mathbf{I} is the identity tensor. $\Theta = \nabla \cdot \mathbf{U}$ represents the dilation of the matrix, and $\mathbf{e} = \frac{1}{2}(\nabla \mathbf{U} + \nabla \mathbf{U}^T)$ the local deformation [88]. Cell traction force over the matrix is represented by an *EF-controlled cell density* saturation function with τ_{C_o} the individual cell traction and λ_{C_o} the saturation value [88].

Since an applied EF (assumed oriented along the $\hat{\mathbf{z}}$ -axis) elongates the cells in a direction perpendicular to the EF vector (say along $\hat{\mathbf{x}}$ -axis), and squeezes them in the parallel direction (along the $\hat{\mathbf{z}}$ -axis) [5,9], it is assumed that cells exposed to the EF change their assumed initial spherical shape into an ellipsoid [6,9]. This is accounted for by the geometric tensor \mathbf{R} [9,126]

$$\mathbf{R} = \left[\frac{a}{a_o} \hat{\mathbf{x}} \otimes \hat{\mathbf{x}} + \frac{b}{a_o} \hat{\mathbf{y}} \otimes \hat{\mathbf{y}} + \frac{c}{a_o} \hat{\mathbf{z}} \otimes \hat{\mathbf{z}} \right], \quad (6.8)$$

where a is the cell radius in the direction of elongation, b is the cell radius in direction of squeezing, c is the cell radius in the transversal direction, and a_o is the radius of the undeformed cell. In addition, it is assumed that the cell volume is preserved during the deformation. Accordingly, by considering $\det \mathbf{R} = 1$ as the relation between the volume of the deformed cell and the initial cell, the bidimensional implementation of Eq. (6.8) requires that the transversal change in cell shape (along the $\hat{\mathbf{y}}$ axis) be equal to that in the squeezing direction, i.e., $c = b$.

Furthermore, the cell shape is a function of both EF strength and exposure time [9,126]. Accordingly, both higher EF strength and longer EF exposure times cause increased cell elongations [9,126]. Therefore, by considering linear relations between EF exposure, time and cell elongation, and following the conservation of cell volume after elongation, the cell radii a and b can be expressed as

$$a = \begin{cases} a_o + \frac{a_{max} - a_o}{t_{max}} t, & \text{if } 0 \leq t \leq t_{max}, V_e \neq 0 \\ a_{max}, & \text{if } t_{max} < t, V_e \neq 0 \\ a_o, & \text{if } V_e = 0, \end{cases} \quad (6.9)$$

$$b = \begin{cases} \frac{a_o}{\sqrt{1 + \frac{a_{max} - a_o}{a_o t_{max}} t}}, & \text{if } 0 \leq t \leq t_{max}, V_e \neq 0 \\ \frac{a_o}{\sqrt{\frac{a_{max}}{a_o}}}, & \text{if } t_{max} < t, V_e \neq 0 \\ a_o, & \text{if } V_e = 0. \end{cases} \quad (6.10)$$

where a_{max} is the maximal elongation depending on the EF strength [9,126] and t_{max} is the exposure time to reach the maximal elongation [126]. In Eqs. (6.9) - (6.10), the dependence of the necessary cell elongation on time is explicit, whereas the dependence on the EF strength is complemented by an implicit linear function represented by the coefficient a_{max} . The derivation of this function is explained in Appendix A.3.

Osteogenesis

The percentage of new bone formation by osteogenesis is modeled by using a tissue replacement equation given by

$$B = \left[1 - e^{(-r_{BC}(V_e)C_o - r_{BQ}(V_e)Q_o)} \right] \left[\frac{W_U^n}{U^n + W_U^n} \right], \quad (6.11)$$

where $r_{BC}(V_e)$ and $r_{BQ}(V_e)$ are control parameters related to cell adhesion and proliferation [106]. Both processes are increased when the cells are exposed to the EF [6, 125]. Accordingly, $r_{BC}(V_e) = r_{BC}(1 + c_4V_e)$, and $r_{BQ}(V_e) = r_{BQ}(1 + c_5V_e)$, with r_{BC} and r_{BQ} the control coefficients for cell adhesion and cell proliferation [106], and $(1 + c_4V_e)$, $(1 + c_5V_e)$ the electrical mediation. c_4 and c_5 are the electric coefficients for both cell adhesion and cell proliferation. W_U and n are the threshold and the slope of an activation function related to the maximum displacements allowed for formation of new bone over the implant surface [16, 36].

Electric potential

The electric potential must satisfy the Laplace's equation in Eq. (4.3). In this model, similarly to the models described in Chapters 4 and 5, the net charge inside the bone-dental implant interface is assumed to be zero, the endogenous EFs and currents present after an injury and during wound healing are avoided [1], and only static potentials are considered.

6.3 Description of the simulation

The mathematical model given by Eqs. (6.1) - (6.11) and Eq. (4.3) has been implemented for a bi-dimensional domain that represents a section of the bone-dental implant interface [68, 106] (Fig. 6.3a). The width of the interface was obtained from experimental observations [21, 121] for both the thickness of the layer of proteins attached to the implant surface, and the volume of necrotic tissue left behind by the insertion procedure (Fig. 6.3b).

The initial conditions are zero for fibrin, osteogenic cells, granulation tissue, matrix displacement and new bone. Initial values for thrombin and fibrinogen correspond to small perturbations of the steady-state of a modified form of the glycolysis model [68, 83]. The initial condition for the osteogenic chemical concentration is 5×10^4 mg/ml [14]. For the osteogenic cell density $C_o(\mathbf{x}, t)$, we assume a density of 1×10^6 cells/ml [14] at the host bone side. However, this boundary condition is equal to unit for the sake of obtaining a cell density within the range [0-1] (normalized but non-dimensionless), which allows us to overcome the differences in the initial cell seeding number found among experimental protocols. For the same reasons, the cell saturation value C_i is set to one [86]. Boundary conditions are also implemented for the displacement $U(\mathbf{x}, t)$. Accordingly, we allow displacement along the x -axis at the top and bottom edges of the interface.

Moreover, for the solution of the osteogenic chemical $Q_o(\mathbf{x}, t)$ in Eq. (6.5) and the displacements $U(\mathbf{x}, t)$ in Eq. (6.7), we used an *injury area* $5 \mu\text{m}$ thick as measured from the implant surface (Fig. 6.3c). This area corresponds to the contact zone between the tissue in formation and the implant surface [121]. Accordingly, for the elements within this area, the reactive term of the osteogenic chemical equation $Q_o(\mathbf{x}, t)$ is modified as

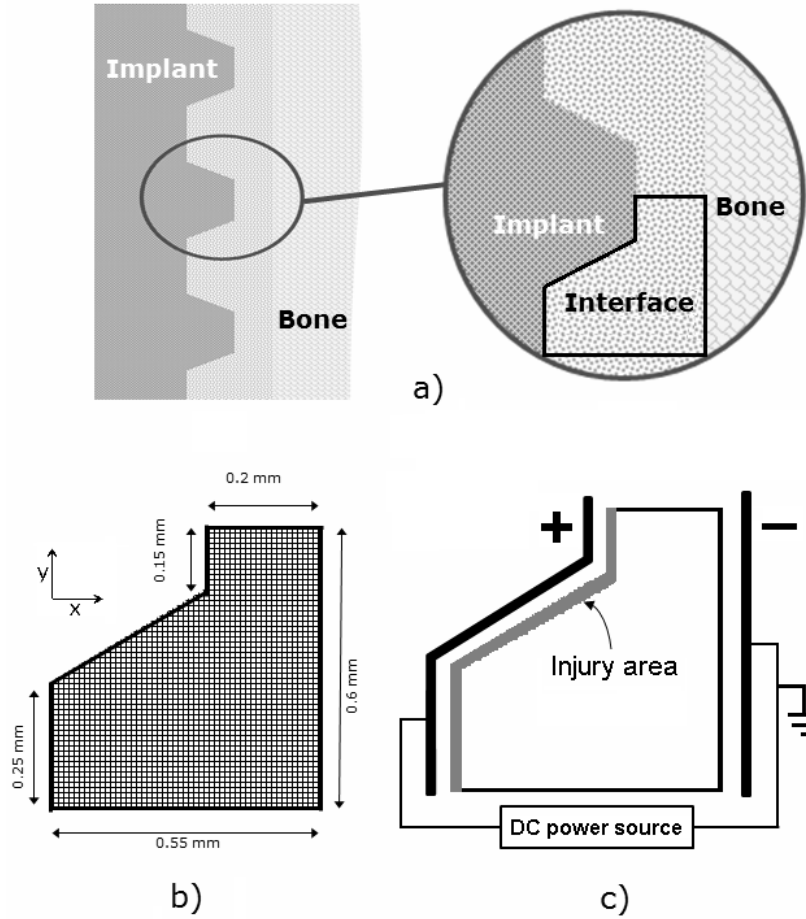


Figure 6.1: a) Sketch of the bone-dental implant interface. b) Dimensions used for the bi-dimensional domain. c) Sketch of the electrostimulation at the bi-dimensional domain.

$$\frac{\partial Q_o}{\partial t} = D_{Q_o} \nabla^2 Q_o + r_{QI} R_s + r_{Q_o} C_o + (r_{QE} C_o + r_{QEIf}) V_e - (\delta_{Q_o} + \delta_{QC} C_o) Q_o, \quad (6.12)$$

where r_{QI} refers to the osteogenic chemical concentration that is released by the platelets activated when in contact with the surface irregularities [122]. Since platelets accumulate near the positive electrode [104], the additional production term with coefficient r_{QEIf} accounts for the electrical activation of platelets and the consequent electrically mediated chemical release [58].

Bone formation depends on the displacement of the fibrillar matrix [20, 36]. This displacement depends on the mechanical properties of the fibers [71]. However, such properties can be changed by the presence of surface irregularities in the dental implant that modify the physiological conditions needed for fiber formation [36, 71, 122]. Electrical stimulation also affects the mechanical properties of the fibers, making a stronger bone-implant interface [127]. Therefore, in order to account for the changes in the mechanical properties of the fibrillar network, Young's and Poisson's moduli at the injury area are expressed as

$$(E, \nu) = \begin{cases} (E_{max}, \nu_{max}), & \text{if } R_S = 1, \quad V_e = 0 \\ (E_{min}, \nu_{min}), & \text{if } R_S = 0, \quad V_e = 0 \\ h_U f V_e \left(\frac{f^n}{f^n + W_{fh}^n} \right) \left(\frac{V_e^n}{V_e^n + W_{Veh}^n} \right) (E_{max}, \nu_{max}), & \text{if } V_e \neq 0, \end{cases} \quad (6.13)$$

where (E_{max}, ν_{max}) and (E_{min}, ν_{min}) are chosen to model the fact that the higher the surface roughness ($R_S=1$) the lower the displacement of the fibers [122, 128]. Otherwise ($R_S=0$) the displacement is intense enough to create a gap between the healing front line and the implant surface that prevents the osseointegration [36, 129]. However, in the presence of the electrical stimulus ($V_e \neq 0$), the increased (denser) fibrin formation due to both the electrical drift of the blood components and the electrical activation of platelets [58, 104] is coupled with the maximal Young's and Poisson's moduli via the coefficient h_U , to reduce the displacement of the matrix.

Since the effect of the electric stimulus also affects the elements outside the injury area by changing the physiological conditions for fibrin formation [71], the variation for Young's and Poisson's moduli throughout the rest of the domain is

$$(E, \nu) = \begin{cases} (E_{max}, \nu_{max}), & \text{if } V_e = 0 \\ \left[1 + h_U f V_e \left(\frac{f^n}{f^n + W_{fh}^n} \right) \left(\frac{V_e^n}{V_e^n + W_{Veh}^n} \right) \right] (E_{max}, \nu_{max}), & \text{if } V_e \neq 0. \end{cases} \quad (6.14)$$

The numerical solution of Eqs. (6.1) - (6.11) and Eq. (4.3) is performed by using the finite elements method with a *Galerkin approach* in combination with a *backward Euler* implicit finite difference scheme for the time discretization. The spatial mesh consists of 9132 quadrilateral patches and 9350 nodes with as many linear elements associated. The numerical implementation is performed by using an Intel Fortran user subroutine customized so as to be executed by the commercial software Abaqus 6.11 [97]. Numerical values of the parameters are obtained from literature and are detailed in Appendix A.3. The simulation corresponds to the first 21 days of healing at the bone-dental implant interface [31, 47]. Simulation time is adjusted in such a way that the first 10 minutes correspond to the fibrin network formation [51]. Then, using the fibrin network as support, the osteogenic cell migration is started 3 days after injury [31, 47], taking 5 days to cover the bone-dental implant interface. The formation of the granulation tissue starts 4 days after injury [12, 13], and lasts 3 days. The displacements of the matrix are simulated for the last three days of cell migration. The final 14 days are for the new bone formation [31, 47]. Actual simulation time is 2 hours on a double-core 2.3 GHz, 2-GB-RAM laptop PC.

6.3.1 Analyzed cases

The mathematical model is applied to a smooth ($R_S = 0$) and a rough surface ($R_S = 1$). In the smooth surface case, the platelet activity at the injury area is reduced, which leads to a lower osteogenic chemical concentration near the implant surface [36, 122]. Therefore, a lower cell density is obtained at the injury area with a corresponding reduced bone formation [20, 41]. On the other hand, the rough surface activates platelets at the injury area [122], which in

turn increase the chemotactic signal near the implant surface. These facts enhance the bone formation near the implant surface, allowing contact osteogenesis [36, 122].

Furthermore, electrostimulation influences bone deposition at the bone-dental implant interface [11], and this influence is believed to depend on the strength of the electrical stimulus [5, 11, 127]. Therefore, it is assumed that an electrical device, built inside the dental implant, provides a static EF within the bone-dental implant interface, devised similarly to the bipolar induction screw system (BISS) [130]. Such EF is numerically reproduced by assuming two electrodes connected to an external power source as shown in Fig. 6.3c. Four different cases were used to evaluate four different EF strengths: 0, 0.25 V/mm, 0.5 V/mm and 0.75 V/mm, respectively [7, 9]. The EF distribution in each case is obtained by solving the two-dimensional boundary value problem for the electric potential as in Eq. (4.3). The boundary conditions are chosen in such a way that the host bone is the ground electrode ($V_e = 0$). The boundary corresponding to the implant surface follows the expression $V_B = EL$, where V_B is the potential at the boundary, E is the expected EF strength, and L is the lower width of the bone-dental implant interface (0.55 mm) (Fig. 6.3b). EF exposure is maintained throughout the simulated 21 days, reproducing experimental protocols in which the bone formation induced by an static EF is evaluated during several weeks and months [2, 76].

6.4 Numerical results

Formation of the fibrin network

Fibrin density in the presence of EF is higher near a preferential electrode [58]. Fig. 6.4 shows the numerical results for the first 10 minutes after the implant insertion. The stripe-like pattern resembles the blood clot fibrillar network covering the entire interface [12, 71]. The dimension of the fibers is comparable with the width and length of fibrin fibers formed under experimental conditions [50, 71]. When no EF is applied (Fig. 6.4a), the fibrillar formation is uniform throughout the interface, with a maximum value below the maximal fibrin density found experimentally, i.e., 2.5 mg/ml [71].

When the EF is applied, the fiber density increases near the positive electrode [104, 114]. Therefore, the fibrin formation is attracted and increased in the vicinity of the positive electrode. In contrast, formation near the negative electrode remains unchanged, since no fibrin is attracted to it (Fig. 6.4b - 6.4c) [114]. Furthermore, the fibrin attraction depends on the EF strength [105, 114], as demonstrated by evaluating the fibrin formation at the evaluation zone (Fig. 6.3c). Specifically, no EF exposure yields a maximal fibrin density at the injury area of 1.75 mg/ml, whereas exposure to an EF of 750 mV/mm leads to a maximal density of 2.25 mg/ml. Values computed for EFs of 250 and 500 mV/mm are 1.98 and 2.14 mg/ml respectively.

Osteogenic cells migration

The fibrin fibrillar network supports cell migration, a process depending on both the surface roughness (R_s) and the EF strength [5, 41]. Fig. 6.4 shows the results for the cell migration pattern 5 days after injury. In all cases, the migration pattern is directed from the host bone surface (right) toward the implant surface (left). When no EF is applied (Fig. 6.4a) and a smooth surface is assumed, the lower-left side of the interface has almost no cells, and the

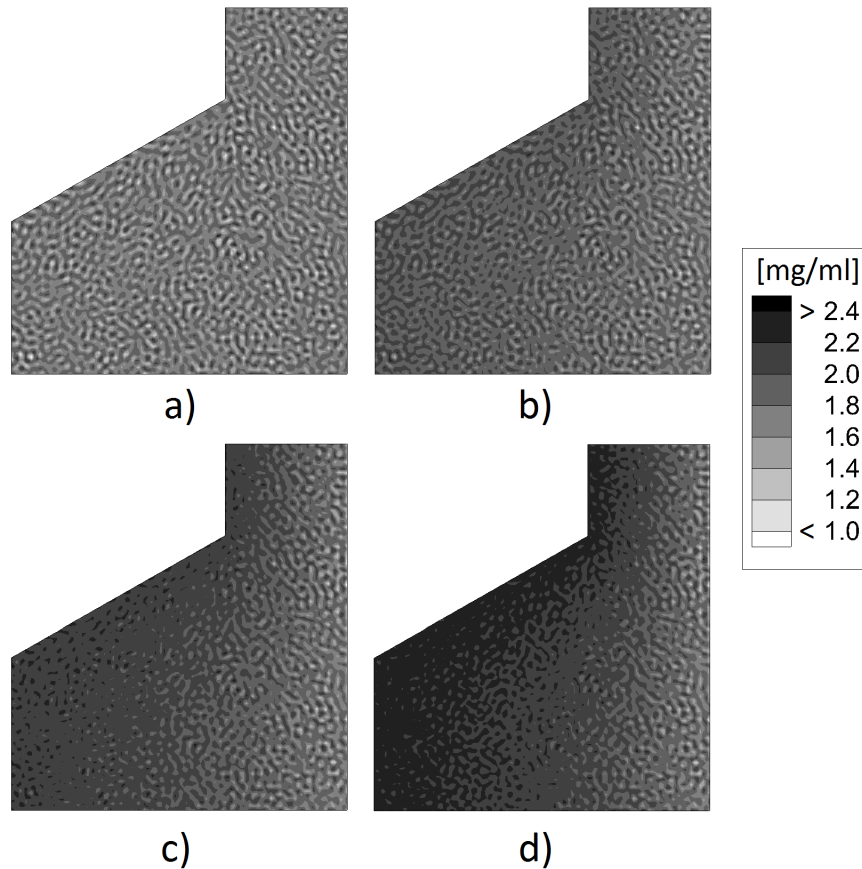


Figure 6.2: Fibrin formation after 10 minutes of exposure to different EF strengths. a) $EF = 0$. b) $EF = 250$ mV/mm. c) $EF = 500$ mV/mm. d) $EF = 750$ mV/mm.

higher cell density, equal to the normalization value, originates at the bone surface. When a rough surface is assumed (Fig. 6.4b), the dispersion pattern formation is accelerated and some cells start to accumulate at the implant surface.

A similar accumulation and spreading pattern is obtained when an EF of 250 mV/mm is applied (Fig. 6.4c - 6.4d). For this case, the EF increases the cell spreading so that cell accumulation is started even over a smooth surface. Therefore, a smooth surface with a 250-mV/mm EF leads to a cell migration profile with better cell spreading and higher cell accumulation at the implant surface than the one observed with a rough surface implant and no EF (Fig. 6.4b). Additional increases in the cell spreading and cell accumulation are also observed when using EFs of 500 and 750 mV/mm (Fig. 6.4e - 6.4h).

An observation to the EF-mediated cell spreading and cell accumulation at the implant surface 7 days after injury is obtained by evaluating the cell density along a straight line running parallel to the x -axis and crossing the y -axis at 0.1 mm (see Fig. 6.3b). Results plotted in Fig. 6.4 show that the application of an EF of 250, 500 and 750 mV/mm increases by 25, 65 and 110 %, respectively, the cell accumulation over a smooth surface as compared to that obtained without EF (Fig. 6.4a). A similar behaviour with cell accumulations of 27, 61 and 92 % higher than the one in the case of no EF is obtained for a rough implant surface

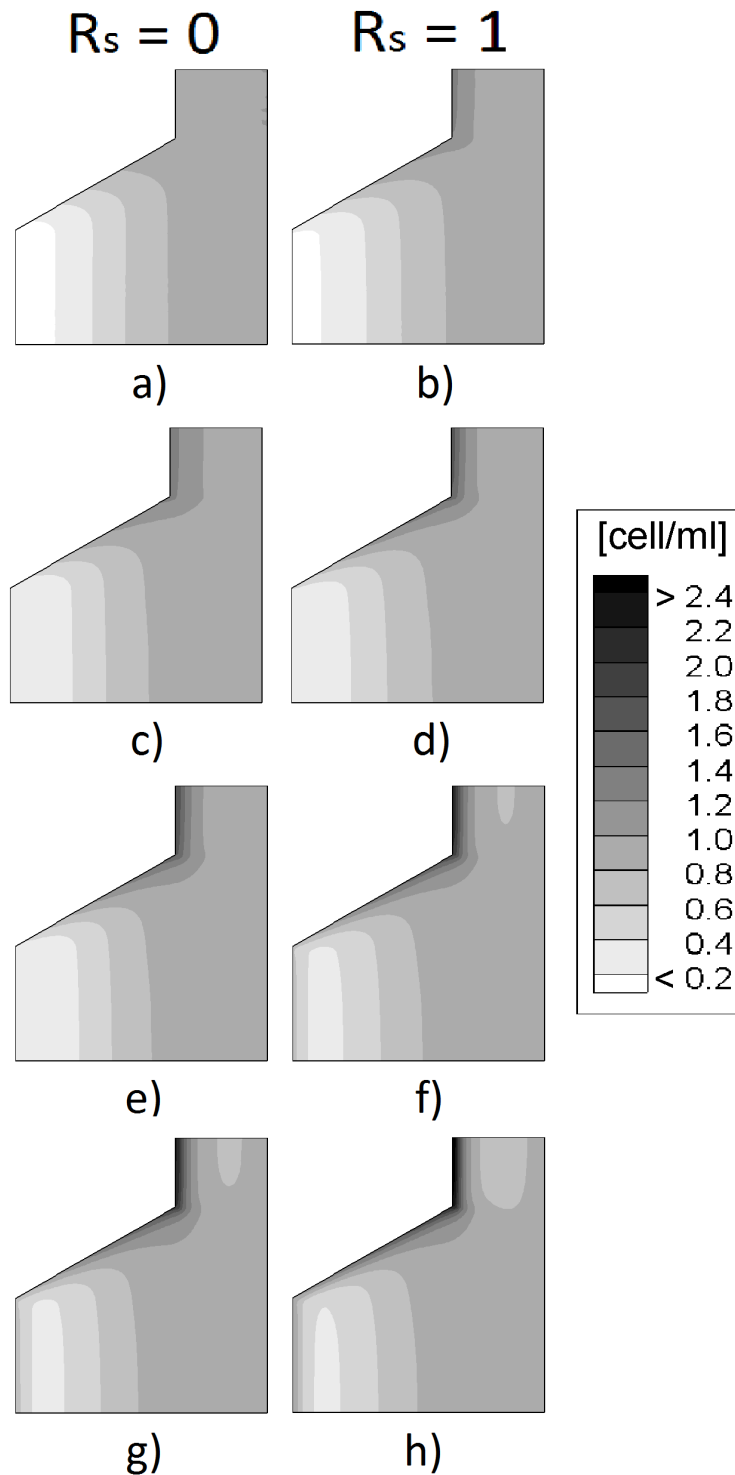


Figure 6.3: Osteogenic cells density profile (in 10^6 cells/ml) 5 days after injury. Left column: smooth surface. Right column: rough surface. a), b) EF = 0. c), d) EF = 250 mV/mm. e), f) EF = 500 mV/mm. g), h) EF = 750 mV/mm.

and the same EFs strengths.

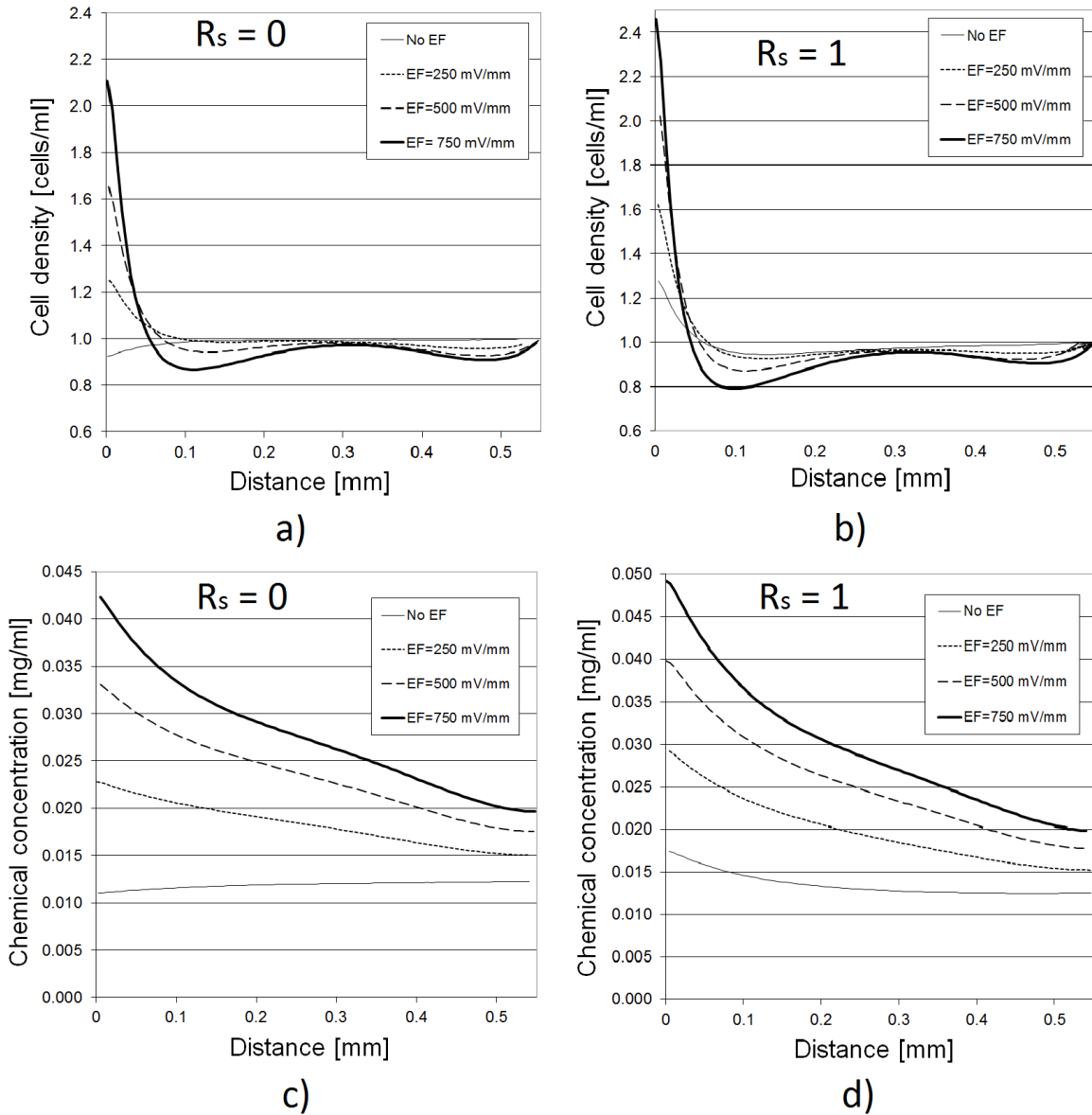


Figure 6.4: Osteogenic cell density (in 10^6 cells/ml) and osteogenic chemical concentration (in mg/ml) along the bone-dental interface, 7 days after injury.

Cell migration is activated by the presence of both electrical and chemical signaling [5]. While the electrical signal is constant and depends only on the applied electric potential, the chemical signal varies due to the surface roughness and the synthesis of osteogenic chemical by the migrating cells due to the presence of the electrical stimulus [8, 124]. Figs. 6.4c - 6.4d show the variations 7 days after injury computed 0.1 mm above the bottom-line of the domain. Since both the surface irregularities and the EF induce higher platelet activation

with consequent higher release of chemical signaling, the chemical concentration is greater near the implant surface and decays exponentially due to diffusion. Furthermore, since the EF stimulates the cells to synthesize signaling molecules [124], the chemical concentration depends on the EF strength for both the smooth (Fig. 6.4c) and the rough (Fig. 6.4d) surfaces.

Numerical results indicate that without EF, surface irregularities lead to a 1.4-fold increase in the osteogenic chemical concentration directly at the implant surface. This result is in agreement with experimental observations in surfaces with topographical irregularities of 1 μm [131]. Moreover, a 1.9-fold increase in the chemical concentration near the implant surface is observed for a smooth surface with a 250-mV/mm EF. This shows that even a low EF strength induces a chemical activation higher (but comparable) to that observed in a rough surface with no EF [41, 131]. A smooth surface and EFs of 500 mV/mm and 750 mV/mm lead to a 2.7-fold and 3.5-fold increase, respectively, as compared to the case without EF. Likewise, a rough surface with EFs of 250, 500 and 750 mV/mm respectively, shows 1.7-, 2.3-, 2.8-fold increases in the chemical concentration over the implant surface with respect to the case without EF.

Granulation tissue formation and displacement of the fibrillar matrix

The replacement of the fibrin network with granulation tissue starts with the migration of the osteogenic cells [12]. Fig. 6.4 shows the numerical results, where the dependence on both the fibrin and osteogenic cells spatial-temporal patterns (See Eq. (6.6)) is observed. Specifically, the granular tissue inherits the fibrillar appearance of fibrin together with the pattern of the osteogenic cells (Figs. 6.4a - 6.4c). Since fibrin formation is unaffected by the surface roughness, and in Eq. (6.6) the cell accumulation over the implant surface is reduced to an activation function controlled by a threshold in the cell density, the formation of granulation tissue is the same for both smooth and rough implant surfaces.

However, the presence and the intensity of the EF increases the granular tissue density near the implant surface. 5 days after injury, the exposure to EF strengths of 250, 500 and 750 mV/mm (Fig. 6.4d - 6.4f) increases the granular tissue formation which inherits the EF-dependent fibrin formation shown in Fig. 6.4. Since the EF speeds up the cell accumulation over the implant surface (Fig. 6.4), the formation of granular tissue directly over the implant surface is accelerated at higher EF strengths. Therefore, when an EF of 750 mV/mm is applied, granulation tissue appears over the lower part of the implant surface. This is possible because the accumulated cells start producing new tissue even before the arrival of the formation front [36]. An insight into this increment can be observed in Fig. 6.4h, where the average granulation tissue density is measured 6 days after injury along a line which crosses the interface at $y = 0.1$ mm.

Moreover, the contraction forces exerted by the migrating cells cause displacement of the fibrillar matrix, as shown in Fig. 6.4. When no EF is applied, an implant with smooth surface leads to displacements up to 750 μm directly over the implant surface (Fig. 6.4a). With a rough surface, the displacements have the same distribution as in the smooth surface, but the amplitude directly over the implant surface decreases to a maximal of 300 μm (Fig. 6.4b). An additional reduction in the intensity of the displacements, not only over the implant surface but on the rest of the interface as well, is observed when the EF is applied. Interestingly, an EF of 250 mV/mm reduces the displacements over a smooth surface to a maximal of 200 μm (Fig. 6.4c), and to 130 μm over a rough surface (Fig. 6.4d). In consequence, the EF reduces

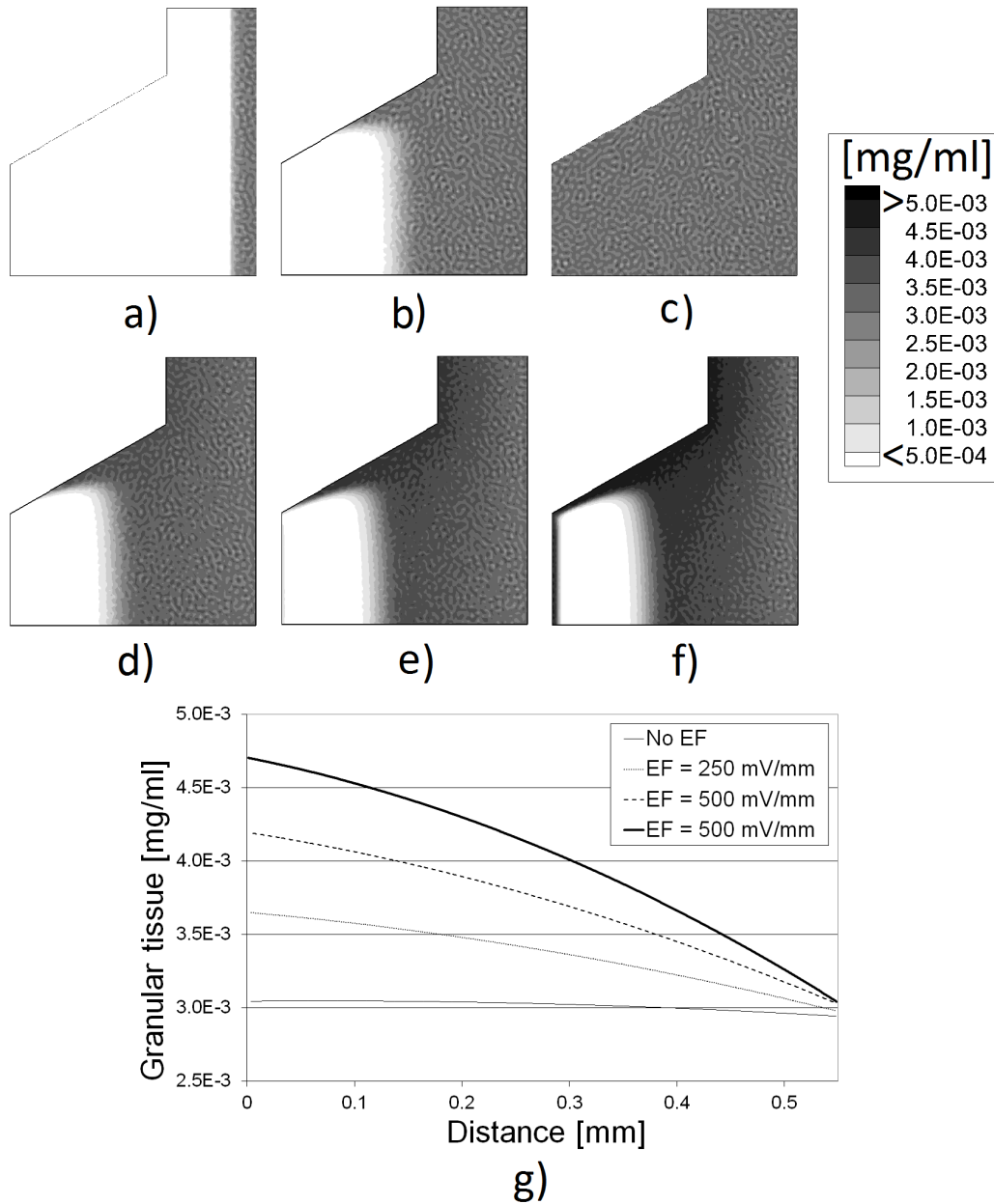


Figure 6.5: Granulation tissue formation (in mg/ml) a-c) 4, 5 and 6 days after injury respectively, with no EF; d-f) with EFs of 250, 500 and 750 mV/mm respectively, 5 days after injury; g) (average) along the bone-dental implant interface, 6 days after injury.

the displacements of the matrix as the surface irregularities do, but more effectively. This same behaviour is observed when using EFs of 500 and 750 mV/mm, according to which the displacements in both the smooth and rough surface cases (Fig. 6.4e - 6.4h) decrease to 125, 75 μm , and 100, 60 μm respectively.

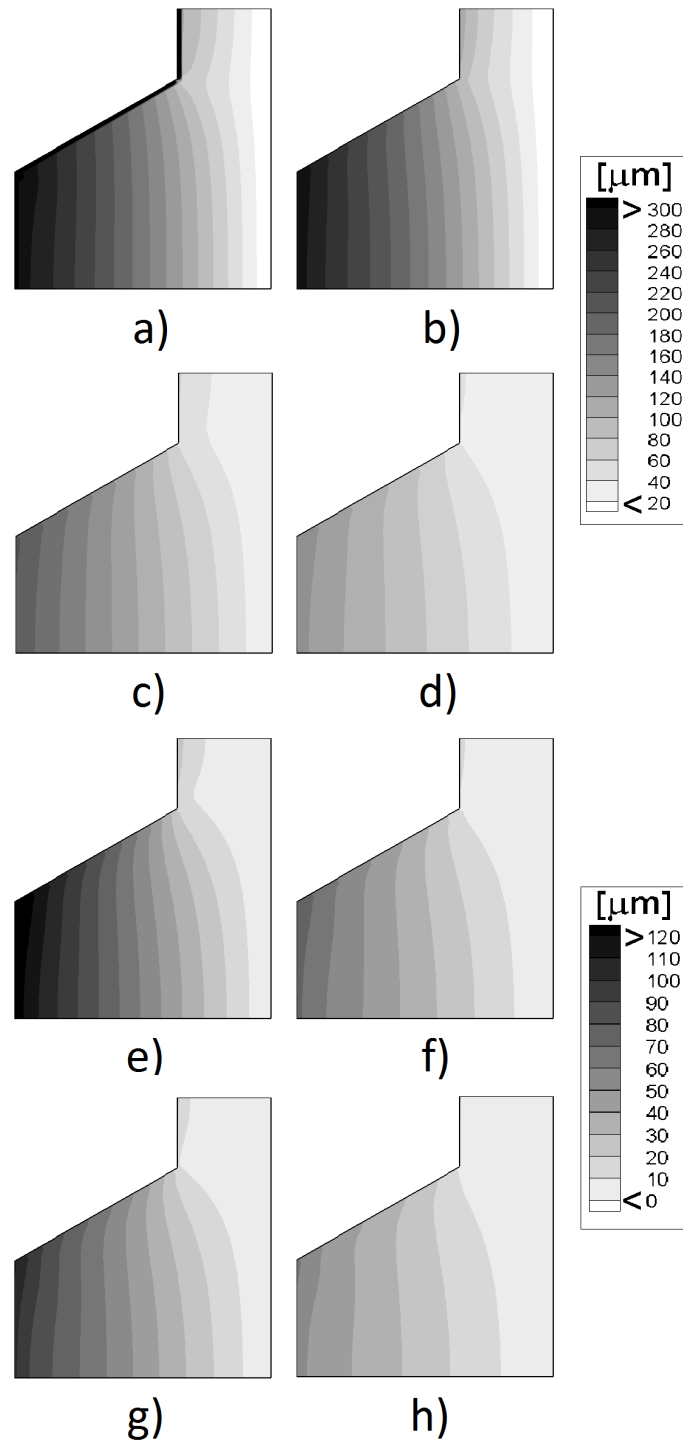


Figure 6.6: Displacement of the fibrillar matrix (in μm) 7 days after injury. Left column: smooth surface. Right column: rough surface. a), b) $EF = 0$. c), d) $EF = 250 \text{ mV/mm}$. e), f) $EF = 500 \text{ mV/mm}$. g), h) $EF = 750 \text{ mV/mm}$.

New bone formation

Bone formation is the consequence of both the osteogenic cell density and the chemical concentration mediated by the displacements of the matrix. It is also affected by both the EF strength and the surface roughness. Fig. 6.4 summarizes the numerical results. When no EF is applied, the bone formation 14 days after injury over a smooth implant surface is about 60 % (Fig. 6.4a), and almost 80 % over a rough surface (Fig. 6.4b). Interestingly, 21 days after injury these values have evolved to null and almost 90 % over the smooth and rough surface, respectively. In fact, a smooth surface allows direct osteogenesis only, conditioned by the displacement of the matrix which within enough time creates a gap that prevents bone formation directly over the implant surface (Fig. 6.4c). In contrast, a rough surface enables both direct and contact osteogenesis, with a consequent bone formation over the surface in concordance with the percentage expected for a successful implant osseointegration, i.e., more than 80 % [16].

When the EF is applied, the bone formation over both a smooth and a rough surface increases with time in response to both direct and contact osteogenesis, meaning that the EF facilitates osteoinduction and osteoconduction even over smooth surfaces [59, 132]. Accordingly, the presence of EFs of 250, 500 and 750 mV/mm lead to average bone formation percentages 14 days after injury above 85 % in the domain (Fig. 6.4a - 6.4b). This value increases to 90-95 % 21 days after injury (Fig. 6.4c - 6.4d). In these three cases, the bone formation directly over the implant surface is higher than near the host bone, and it is maximal when the 750-mV/mm EF is applied.

6.5 Discussion

Numerical results show that the biological events activated during wound healing at the bone-dental interface can be electrically controlled. For a start, numerical evidence shows that EF exposure increases the fibrin density at the positive electrode in agreement with experimental reports [105, 114]. Since an electrical stimulus induces formation of a thicker network of fibrin and blood components directly over a metallic surface [58, 133], the stripe-like fibrin pattern near the implant surface plotted in Figs. 6.4b - 6.4c reproduces fibers thicker than those obtained without EF (Fig. 6.3c). This in turn corresponds to larger [133] and denser [114] fibrin fibers. As a consequence, the distances between individual fibers may be smaller than the mesh edge and hence, individual fibers are not clearly identifiable. This explains the homogeneous spot-like fibrin concentration near the implant surface observed in Fig. 6.4b - 6.4c.

Regarding osteogenic cell migration, numerical results well represent the idea of electro-taxis or cell migration guided by an EF [5], with cell migration along the interface, and accumulation rates depending on the EF strength [123]. Accordingly, the cell density over the implant surface increases with the EF as shown in Fig. 6.4, with the surface roughness being a mediator for an even larger increase. Comparing the cell accumulation over the implant surface for the smooth and the rough surfaces for the three EF strengths shows that the average maximal increase in cell accumulation achievable with the rough surface is 25 % of the value obtained with the smooth surface, a value similar to the one observed experimentally [134]. Therefore, according to the results shown in Fig. 6.4, higher cell accumulation over the implant surface can be obtained by using electrostimulation, in the light of the increased cell

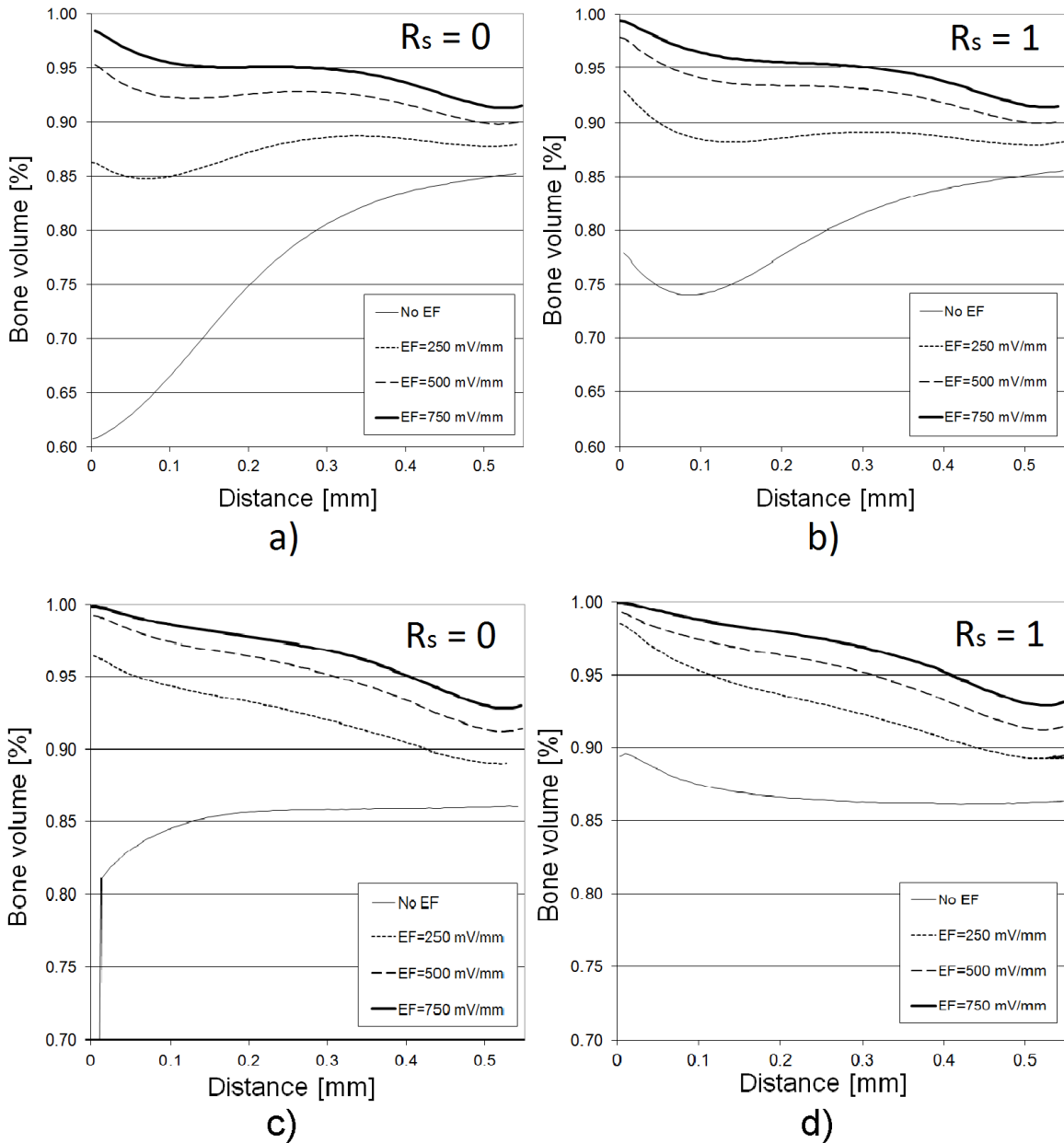


Figure 6.7: Bone formation (in %) 14 days (a-b) and 21 days (c-d) after injury.

adhesion effects [4,59]. Nevertheless, the electrically-mediated increment in cell accumulation leads to reduced cell density spots located about 0.1 mm away from the implant surface for both the smooth and the implant surface (Figs. 6.4 - 6.4).

These spots are created by the strong electrotaxis effect combined with the irregular surface which induce (by both electrical and chemical stimulation) such cell accumulation over the implant surface that even cells that are not part of the migration front line are forced to migrate further away from their position and towards the implant. However, the

time evolution for EFs of 500 and 750 mV/mm shows that these spots are totally filled if cell migration is allowed to last 10% longer than initially conceived. This extra time represents the additional time required by the cells to proliferate and replace the removed cells, and has no consequences on the subsequent modeling stages.

As for the osteogenic chemical concentration, the increments observed when using a rough surface are mainly due to platelet activation [122]. As a consequence, the migration of osteogenic cells at the host bone is activated by a gradient of osteogenic chemical originated at the implant surface [49]. This same principle applies to the EF-mediated increment since platelets can be electrically activated. Therefore, platelets aggregating over the positive electrode release their cytoplasmic granules and create a EF-mediated gradient of chemotactic signaling for cell migration [58, 133]. Moreover, the increase observed in the smooth surface case with different EF strengths is consistent with the EF having a stronger effect on cell migration than the surface irregularities [132]. This effect has been found to depend on the EF strength, which leads to higher cell migration rates [132].

Further interest in the numerical results for both cell density and chemical concentration motivates the following calculations. From Fig. 6.4, the values over the implant surface obtained for a rough surface without EF were subtracted from those obtained for a smooth surface without EF. This yields the net increments due to the surface roughness only. These values are then added to the values obtained over the implant surface when both a smooth surface and the three different EFs were used, which can be considered as the net increments due to EF only. Hence, the addition of the separated surface and EF effects leads to a difference of less than 1 % in the cell migration over the implant surface as compared to that obtained when the two effects are combined. For the osteogenic chemical concentration, the calculated difference is about 4 %. Therefore, the effect that both surface roughness and EF have on the osteogenic cell density and the osteogenic chemical concentration is found to be additive, as experimentally found during corneal cells alignment in the presence of EF and surface grooves [132].

Numerical results also show increments in the granular tissue formation alike to those reported in the literature for soft tissue repair with and without EF [60, 74]. Accordingly, the tissue density when no EF is applied is almost constant around 3 μm (Fig. 6.4h). In contrast, the application of EFs of 250, 500 and 750 mV/mm causes increases of 23, 40 and 57 % respectively, which are comparable with increments of about 20-50 % in the production of collagen-like matrices stimulated by an EF [60, 74].

The ability of an implant surface to retain the fibrillar network during the contraction exerted by the migrating cells is critical for the cell colonization of the surface [36]. An optimal surface design plays a major role in this retention [36, 41], although an EF is also useful. Fiber detachment may be avoided if the implant has surface irregularities as large as the displacements [53], which enhance the bonding capacity of the surface [21, 128]. However, this bonding capacity is also reinforced by an EF which influences both the integrins and the focal contacts intervening in cell adhesion [4].

Numerical results show the effect of EF in reducing the displacement of the matrix well below 500 μm , the highest tolerable displacement lest an implant loosen [129]. Besides, the reduction increases with the EF strength and is induced even over the smooth surface. These results can be explained by the EF-induced polarization of both the smooth and rough surfaces. The polarization induces a surface electric charge that mediates the absorption of biomolecules needed for cell adhesion directly over the implant surface [59]. In addition, it is believed that EF induces adhesion forces similar to those found at molecular level during cell

adhesion and tissue contraction [75]. Therefore, it is plausible to consider a reduction in the contractile forces over the fibrillar matrix as due to a counteracting electro-mechanical force.

Furthermore, since a denser fibrin network is created directly over the implant surface in the presence of an EF, the matrix contraction produced during cell migration might not detach a number of fibers large enough to completely prevent cell colonization of the implant surface. Thus, the application of an EF might reduce the displacements in the matrix also by increasing the number of available fibers attached to the surface.

The effect of both EF and surface roughness in the osteogenic cell density and the osteogenic chemical concentration causes changes in the bone formation profile, as shown in Fig. 6.4. Numerical results confirm that bone formation near the implant surface is also affected by displacements of the matrix above 200 μm . Interestingly, when no EF is applied, the bone formation is similar for both smooth and rough surfaces when observed from the host bone towards the implant surface, but up to 0.02 mm away from it (Fig. 6.4). Therefore, the reduced bone formation observed in the smooth surface indicates the presence of direct osteogenesis only (Fig. 6.4a - 6.4c), while the increased percentage over the rough surface indicates the presence of both direct and contact osteogenesis (Fig. 6.4b - 6.4d). In addition, 21 days after injury the smooth surface loses the amount of bone that had been bone deposited over it after day 14 (Fig. 6.4c). This loss is related to the displacement of the matrix observed at day 21, which is above the maximal value allowed for osseointegration, i.e., 500 μm , and is related to the formation of a gap between the new bone and the implant surface [129]

Moreover, similarities in the shape of the curves for both smooth and rough surfaces are also observed for bone formation when an EF is applied, although in the three scenarios the bone formation near the implant surface follows contact osteogenesis. In consequence, the presence of EF induces contact osteogenesis in both smooth and rough surfaces. This is accomplished by the EF effect on the osteoconduction (and osteoinduction) of the surface [10, 123, 135]. Furthermore, since bone formation along the interface exposed to EF is higher than 80 % 14 days after injury, numerical results show that the accepted osseointegration rate of 80 % [16] is reached in less time in the absence of EF, regardless of the type of implant surface. This result is in agreement with experimental observations on bone formation and osseointegration of dental implants, indicating higher bone deposition rates in shorter times when electrostimulation is applied [10, 11, 61]. Moreover, the increase in the bone percentage found numerically in the presence of an EF is comparable with values reported for EF-induced osteogenesis in rabbit mandible, where percentages of bone mineral density as high as 90 and 94 % were measured after 10 and 20 days of EF exposure [76].

In addition, implant movements of more than 150 μm , which are related to displacement of the fibrillar network and formation of a gap with the new bone front, inevitably leads to the formation of soft tissue instead of bone [16]. Since the EF-mediated surface osteoinduction and osteoconduction lead to higher fibrin formation and cell colonization, the reduction of the matrix displacements down to 50 μm for a rough surface with a 750-mV/mm EF indicates a reduction of the chances of implant motion. Therefore, an EF seems to be a suitable means for improving the primary stability of the implant [129], leading to a higher osseointegration rate in a shortened healing time [10, 76].

This thesis presents a numerical framework for the computational analysis of the influence of electrostimulation in the osseointegration of a dental implant. The numerical results obtained are in good agreement both with the numerical expectations and published experimental findings. Nonetheless, since the mathematical formulations adopted rely on a few simplifying assumptions, further work is required to make the results even more accurate.

In the case of modeling cell electrotaxis, the numerical framework allows to reproduce biological features observed in osteogenic cells when exposed to an EF. Even though the favorably agreement of the numerical results with relevant experiments, a better description of the EF should be used in order to account polarization effects, especially the drift of ions and charge particles inside the cells that may influence the cell migration profile [4]. Such description might deal with the presence of dipole moments which contain the information related to the polarization of the cells. By calculating the equivalent dipole moment at each cell, a cell contingent can be electrically represented in terms of the contributions to the EF by the total equivalent dipoles. These contributions might be helpful in understanding the influence of surrounding cells on the intracellular EF distribution at each cell. Furthermore, such approach might explain localized changes of the transmembrane potential [99, 136] and the localized activation of signaling mechanisms in cells exposed to EFs, especially the calcium signaling pathway [4, 7].

In addition, osteogenic cells should be considered as individual cells rather than a contingent of cells. A discrete cell implementation may be suitable to determine the particular behaviour of single cells when exposed to both electrical and chemical stimuli. Moreover, cell differentiation should be included in the cell dynamics representation in order to extent the model to other biological scenarios. Both requirements can be addressed by implement an electrical description of the cells based on the equivalent dipole moments.

Since cell migration is highly dependent on chemical stimulation, a better indication for the chemical stimulus other than a boundary condition (Chapter 4) or the cell synthesis (Chapters 5 and 6) should be used. Specifically, for the implementation of the cases analyzed by the model of cell electrotaxis described in Chapter 4 (Figs. 4.1b-4.1c, the chemical stimulus was assumed as a boundary condition with value 2×10^{-2} mg/ml. Although this value is consistent with experimental and numerical literature [7, 9, 14], variations to this term lead to changes in

both the response of cells and the cell migration profile [86]. As a consequence, the numerical implementation creates a simulated scenario that may change if the chemical stimulus is modified.

A mechanism for the chemical stimulus to vary might be EF dependence, since EF influences the chemical gradients in-vitro. Therefore, the electrical stimulus influences cell migration not only due to electrotaxis, but also due to an electrically-mediated chemotaxis [137], which might be considered as an EF-driven increase of the chemical stimulus. Such scenario may lead to variations in the cell migration speed that better correlate to the experimental reports stating that the preferential response of cell exposed to electrostimulation could be affected by the presence of an electrically-activated chemical stimulus [101].

Finally, the logarithmic nature of the relations found for cell colonization (Fig. 4.5) show a tendency for a saturation value. This saturation might be related to an EF strength at which no more cells are recruited and are able to proliferate, similar to the cell apoptosis due to the irreversible electropermeabilization of the cell membrane [136]. In consequence, a saturation profile may be obtained for the EF dependent cell migration schemes (Fig. 4.3) with the application of EF strengths higher than 1000 mV/mm. A proper numerical validation of this saturation hypothesis should deal with a refinement of the mathematical description to address the cell behaviour at higher EF strengths, especially those inducing cell electropermeabilization. Such scenario may be useful to analyze the adequate EF dosimetry needed to ensure cell migration and electro-osteoconduction, and to better identify the influence of the EF in cell damage [74, 103].

Likewise, regarding the model of blood clotting in the presence of electrostimulation, special attention should be paid to the molecular interactions prior to the activation of the common clotting pathway. These interactions can be considered as activators/inhibitors for the underlying kinetic reaction and the fibrinogen-fibrin conversion mechanism.

Furthermore, a more detailed description of the platelet density at the bone-dental implant interface may increase the ability of the model to better reproduce experimental findings on electro-haemostasis [58]. Although numerical evidence supports the implementation of the platelet density as a numerical parameter [68], the approach presented in this thesis does not consider the platelet dynamics, which comprises activation by the implant surface. Platelets may reach and adhere to the implant surface, undergoing activation and releasing their cytoplasmatic content rich in fibrinogen [12, 122]. Such increase in the fibrinogen concentration increases the formation and anchorage of fibrin fibers at the bone-dental implant interface [36]. Additional extension of the mathematical description should also deal with the properties of the implant surface and the differences in the fibrin formation mechanism caused by the surface irregularities [122].

Reported evidence also supports that wave-form and frequency of the applied signal may affect the blood clotting profile [58]. Since no experimental or clinical reports were found for the evaluation of the adequate electric stimulus needed to induce blood clotting, the model was implemented for a static stimulus only, whose intensities are comparable to those inducing cell migration by electrotaxis [5]. Nevertheless, a further step for the model should be the implementation of different electrical signals rather than static EF.

As for the model of electrically stimulated osteogenesis, a first modification should include the bone remodeling stage started after the formation of the primary bone, around day 21 after injury [12, 24]. During this stage, the new bone matrix undergoes constant replacement due to hormonal and physical stimuli to acquire the same biomechanical integrity as the host bone [24]. Therefore, in order to ensure bone formation rates above 80 % and a long-time EF-

induced osseointegration, a biological description for the tug-of-war between bone deposition and bone resorption, observed during bone remodelling, should be implemented together with a convenient description of the physical environment.

Furthermore, additional work should be done to investigate the EF influence over the implant surface but at a molecular scale. Such an approach might be useful to assess the EF-induced cell adhesion, the retention of EF-guided molecules, and the electric surface charge activity, all processes affecting the osteoinduction and osteoconduction of the implant surface.

Additional consideration is related to the description of the electrical stimulus applied to the bone-dental implant interface. The assumption of a static electrical stimulus is based on experimental results showing increased cell responses in bone cells that may influence wound healing at the bone-dental implant interface [7,9]. However, other reports show increased bone formation at the interface when applying time-dependent electric signals [11], a strategy widely common in many electrostimulation protocols, especially those used in physical therapy [2].

Similarly, a few comments are in order as regards the numerical parameter values listed in the Appendix. Some of them were extracted directly from the reviewed literature, others were adapted, and a few have been numerically estimated. The difficulty to obtain suitable parameters from experimental evidence is a weakness that the numerical framework presented in this thesis shares with other works in the area of computational modelling of biological phenomena.

Therefore, in the interest of obtaining realistic numerical simulations, it is considered of paramount importance to undergo an adequate validation of the numerical parameters. In concordance, predictions obtained from mathematical models justify lines of experimental work aimed at obtaining complementary data for biological processes described by the mathematical formulations. Accordingly, specific experimental protocols should be used to validate the quantitative numerical results on cell migration speed, cell colonization, blood clotting and osteogenesis as reported in this thesis.

Such experimental approach(es) is(are) needed to further validate the numerical observations. An experimental validation of the specific numerical results may reinforce the suitability of the mathematical models to be used as a prediction tools aimed at reducing time, effort and resources during experimental setups. Specially in the case of modeling blood clotting (Chapter 4), such validation is in fact needed throughout, since the lack of experimental evidence poses limits to the validation of both the numerical results and the parameters. Even though the findings of the model can be correlated to experimental observations on the electrical behaviour of specific blood clotting molecules [57,114], to the best of our knowledge there has been no attempt to measure the effect of an electrical signal in the formation (and density) of a blood clot. Nonetheless, and despite these limitations, it should be highlighted that the parameter values and numerical results used in this thesis are correlated with experimental evidence, making them and the mathematical models, feasible from a biological standpoint.

In conclusion, the numerical framework presented in this thesis is suitable to be used for the prediction of the electrically stimulated wound healing and bone formation at the bone-dental implant interface. The agreement between numerical results and experimental evidence, makes the framework suitable to be used in applications regarding different types of cells and tissues, and in other different clinical scenarios. Among the future applications that are being considered for the models here presented are the extension to time-harmonic EFs, and a better characterization of the electrical behaviour of cells at the individual level in order to provide further insight on the interaction between biology and EFs.

APPENDIX A

LIST OF PARAMETERS

A.1 Parameters for the model of cell electrotaxis (Chapter 4)

The parameters used in the mathematical model of cell electrotaxis (4) were adapted from the available literature and from a previous numerical simulation reported elsewhere [106], involving the density of osteogenic cells and the concentration of osteogenic chemical.

- D_{C_o} : The diffusion constant of the osteogenic cells was estimated as 5.0×10^{-4} mm²/min according to numerical results reported by other authors [14, 26] and the experimental evidence reviewed by them.
- H_{Q_o} : The chemotactic sensitivity coefficient was estimated as 6.95×10^{-4} (mm²/min)(ml/mg) [14]. However, this value was adjusted by numerical experimentation and the value finally used was 5×10^{-4} (mm²/min)(ml/mg).
- E_{C_o} : The electrical sensitivity coefficient was estimated as the cell velocity without electrical stimulus over the maximum field strength for osteogenic cells to migrate. Cell velocity without electrical stimulus was estimated from experimental reports [5, 7] to be around 2×10^{-4} mm/min. Maximum field strength for osteogenic cells movement was assumed to be 12 V/cm, since the application of this field strength lead to cell death [7]. Therefore, and after numerical adjustment, the value for the parameter was 5×10^{-4} mm²/(V · min).
- r_{C_o} : The cellular proliferation rate was adjusted from [26] and taken directly from [106]. The value was 3.57×10^{-3} min⁻¹.
- δ_{C_o} : The cell death coefficient was adjusted from [102] and also taken directly from [106]. The value was 1.388×10^{-5} min⁻¹.
- C_i : The cell saturation coefficient was assumed to be the unit (in cells/ml) based on the assumption that cell density is normalized [86].

- W_{Q_o} : The activation function for cell proliferation due to osteogenic chemical is better described elsewhere [106]. The threshold value for this activation function was 1×10^{-3} (mg/ml).
- n : This parameter is related to the slope of the cell proliferation activation function which is controlled by the chemical threshold value W_{Q_o} . The value used in the simulations was 10.
- D_{Q_o} : The diffusion constant of the osteogenic chemical was estimated from numerical results [14, 26] and taken from [106]. The value was 2.88×10^{-3} mm²/min.
- r_{Q_o} : The osteogenic chemical production rate was estimated through numerical experimentation using as starting point the value 5×10^{-5} min⁻¹ [26, 106]. After adjustments, the value used in the simulations was 1×10^{-5} min⁻¹.
- r_{V_e} : There was not information found for the osteogenic electro-chemical production rate although it is known that electrical stimulation induce synthesis of osteogenic chemical [8]. Since chemical production is dependent of the strength of the electric field, this parameter is related to the magnitude of the electric field vector. By numerical experimentation, the value needed to obtain the desired spatial-temporal patterns was 5.0×10^{-5} (V · min)⁻¹.
- δ_{Q_o} : The decay coefficient of osteogenic chemical was determined from the mid-life of some growth factors [107] and an elsewhere reported value [14]. By numerical adjustments the parameter was set to 2×10^{-3} min⁻¹.
- δ_{Q_C} : The coefficient of osteogenic chemical consumption by osteogenic cells was calculated from the rate of cell proliferation r_{C_o} and a concentration of reference for the osteogenic chemical [26]. Here the parameter was adjusted to 3×10^{-5} min⁻¹ (ml/cells).
- \bar{v} : The magnitude of the convection velocity used in equation (4.4) accounting for the constant flux of osteogenic chemical was calculated from the value used by [5, 138] when performing a similar experiment. By numerical experimentation the value finally used was 1×10^{-3} mm/min.

A.2 Parameters for the model of blood clotting (Chapter 5)

A.2.1 Dimensionless form of the kinetic reaction equations

Equations (5.1), (5.2) are cast into dimensionless form using reference values for time, space, thrombin and fibrinogen concentrations, and the electric potential [68]:

$$t = \bar{t} \cdot t_{ref} \tag{A.1}$$

$$\mathbf{x} = \bar{\mathbf{x}} \cdot L_{ref} \tag{A.2}$$

$$T = u \cdot T_{ref} \tag{A.3}$$

$$F = v \cdot F_{ref} \tag{A.4}$$

$$V_e = v_e \cdot V_{ref}. \tag{A.5}$$

Plugging (A.1), (A.5) into (5.1) and (5.2), the dimensionless values yields the dimensionless form of the kinetic reaction equations for thrombin and fibrinogen including the electrical effect:

$$\frac{\partial u}{\partial t} = \nabla \cdot (D_u \nabla u - u H_u \nabla v_e) + \delta - (1 - \gamma_1 v_e) u v^2 - k u. \quad (\text{A.6})$$

$$\frac{\partial v}{\partial t} = \nabla \cdot (D_v \nabla v + v H_v \nabla v_e) + (1 + \gamma_2 v_e) u v^2 + k u + (1 - \gamma_3 v_e) \gamma - v. \quad (\text{A.7})$$

Equations (A.6), (A.7) are a modified form of the glycolysis model used in morphogenesis applications [82, 98]. Therefore, the values of the parameters observed in these equations correspond to the values needed to obtain spatial-temporal patterns resembling fibers permeating the simulation domain. Numerical experimentation was employed to determine the dimensionless values involved in the new terms. Accordingly, the dimensional values can be obtained as follows:

$$D_u = D_T \frac{t_{ref}}{L_{ref}^2} = 1.0 \quad (\text{A.8})$$

$$D_v = D_F \frac{t_{ref}}{L_{ref}^2} = 0.08 \quad (\text{A.9})$$

$$H_u = E_T \frac{t_{ref} V_{ref}}{L_{ref}^2} = 2.0 \quad (\text{A.10})$$

$$H_v = E_F \frac{t_{ref} V_{ref}}{L_{ref}^2} = 2.0 \quad (\text{A.11})$$

$$\delta = k_1 \frac{t_{ref} P}{T_{ref}} = 1.2 \quad (\text{A.12})$$

$$k = k_3 t_{ref} = 0.06 \quad (\text{A.13})$$

$$k = k_3 \frac{t_{ref} T_{ref}}{F_{ref}} = 0.06 \quad (\text{A.14})$$

$$\gamma = k_4 \frac{t_{ref} G}{F_{ref}} = 0.03 \quad (\text{A.15})$$

$$\gamma_1 = c_1 V_{ref} = 0.2 \quad (\text{A.16})$$

$$\gamma_2 = c_2 V_{ref} = 0.2 \quad (\text{A.17})$$

$$\gamma_3 = c_3 V_{ref} = 0.2545 \quad (\text{A.18})$$

$$1 = k_2 t_{ref} F_{ref}^2 \quad (\text{A.19})$$

$$1 = k_2 t_{ref} T_{ref} F_{ref} \quad (\text{A.20})$$

$$1 = k_5 t_{ref}. \quad (\text{A.21})$$

To reconcile the double representation available for k_2 and k_3 (as given in Eqs. (A.13), (A.14) and (A.19), (A.20)), it results convenient to adopt the following convention:

$$T_{ref} = F_{ref} = C_{ref}. \quad (\text{A.22})$$

Additionally, assuming a prothrombin concentration equal to the concentration of granules released by activated platelets [68], it is possible to reduce the concentrations of prothrombin and of the released granules to a single parameter as follows:

$$P = G = C_{ref}. \quad (\text{A.23})$$

A.2.2 Parameters of the model

- t_{ref} : This parameter was taken from a previous numerical approach for the coagulation of the bone-dental implant interface [68] as 10 minutes.
- L_{ref} : This is the maximum distance between the host bone border and the implant surface. Considering the region of necrotic tissue after implant placement 0.2 mm wide [121], and a screw type dental implant with threads 0.35 mm deep, the value of the parameter is 0.55 mm.
- C_{ref} : The reference concentration is selected from [68] as 1 mg/ml.
- δ : This parameter is obtained by implementing the glycolysis model for stripe-like spatial-temporal patterns [98] as 1.2.
- γ : This parameter also comes from the implementation of the glycolysis model and has the value 0.06.
- D_T : The diffusion constant for thrombin is obtained from Eq. (A.8) as $5.0417 \times 10^{-4} \text{ mm}^2 \text{ s}^{-1}$ [68]. The value for $D_u = 1$ is obtained from the glycolysis model.
- D_F : The diffusion constant for fibrinogen is calculated from Eq. (A.9) as $4.0333 \times 10^{-5} \text{ mm}^2 \text{ s}^{-1}$, a value close to that obtained by using the Einstein's equation [68]. $D_v = 0.08$ is obtained from the glycolysis model.
- E_T, E_F : The sensitivities for the electrical dispersion of both thrombin and fibrinogen are calculated based on numerical experiments performed to find suitable values for H_u and H_v . Accordingly, it was found that the dimensionless parameters may have values within the range [0.5 - 2.0]. However, to obtain the desired spatial-temporal patterns, both values were fixed to 2.0. Hence, the dimensional parameters are $1.8 \times 10^{-3} \text{ mm}^2 (\text{V} \cdot \text{s})^{-1}$.
- c_1, c_2 : The parameters controlling the electrical activation of the kinetic reaction between thrombin and fibrinogen were calculated as 0.3636 V^{-1} using 0.2 as the dimensionless value for both γ_1 and γ_3 .
- c_3 : Assuming that the activation of platelets by the presence of an EF is similar to the activation during a thrombocytosis case [68], and considering the maximal EF that can be applied to the bone-dental implant interface as 750 mV/mm [7, 9], the parameter

controlling the electrical activation of platelets is calculated as 0.4627 V^{-1} , using 0.2545 for γ_3 .

- f_{max} : According to experimental observations [71], a blood clot formed by the conversion of fibrinogen reaches a fibrin concentration of 2.5 mg/ml, assumed here as the maximal value of fibrin concentration.
- α, β : These values are taken from a previous numerical implementation [68] as 0.5 s^{-1} and $0.37 \text{ (mg/ml)}^{-1}$.
- β_e : The solution of Eq. (5.3) is conditioned to the following inequality:

$$1 - (\beta + \beta_e V_e) f_{max} > 0. \quad (\text{A.24})$$

Accordingly, and considering $V_e = 750 \text{ mV/mm}$ as the maximal EF to be applied to the bone-dental implant interface, the value of the parameter β_e must be lower than $0.072 \text{ (V mg/ml)}^{-1}$. By numerical experimentation, the value finally used is $0.02 \text{ (V mg/ml)}^{-1}$.

- W, p : The threshold for the fibrin activation function W is 1, whereas the slope of this same function is controlled by $p = 10$.

A.3 Parameters for the model of osteogenesis (Chapter 6)

Most numerical parameters were obtained from previous simulations [68, 106]. Additional values were extracted from the available literature and in the cases where no related information was found, numerical experimentation was adopted to arrive at suitable values.

Thrombin, fibrinogen and fibrin

D_T, D_F : The thrombin diffusion constant is set to $5.0417 \times 10^{-4} \text{ mm}^2/\text{s}$ [68]. The fibrinogen diffusion constant is $5.647 \times 10^{-5} \text{ mm}^2/\text{s}$ as in [68].

$k_1 - k_5$: The set of parameters involved in the reaction terms are calculated from a dimensionless form of Eqs. (6.1) - (6.2) which corresponds to a modified glycolysis model [68, 83]. The values are $2.0 \times 10^{-3} \text{ s}^{-1}$, $1.7 \times 10^{-3} \text{ (s (mg/ml)}^2)^{-1}$, $1.0 \times 10^{-3} \text{ s}^{-1}$, $50 \times 10^{-6} \text{ s}^{-1}$, and $1.7 \times 10^{-3} \text{ s}^{-1}$, respectively.

E_F, E_T : No information was found for the electrical dispersion of both thrombin and fibrinogen. Therefore, the values are calculated from numerical experiments so as to obtain spatial-temporal patterns which are biologically meaningful. Accordingly, the value $1.8^{-3} \text{ mm}^2 \text{ (V} \cdot \text{s)}^{-1}$ is set for both parameters.

c_1, c_2, c_3 : The electrical control coefficients for thrombin and fibrinogen c_1, c_2 are both set to 0.3636 V^{-1} using numerical experimentation. The electrical control for platelet activation c_3 is calculated assuming that platelets (in the presence of a 750-mV/mm EF) are activated in a similar way as in during thrombocytosis [68]. Accordingly, the numerical parameter was calculated as 0.4627 V^{-1} .

α , β , and β_e : The fibrin activation rate α and the the blood quality factor β are 0.5 s^{-1} and $0.37 \text{ (mg/ml)}^{-1}$ respectively [68]. The electrical blood factor β_e is calculated observing that the denominator of Eq. (6.3) is zero when $\beta_e = 0.072 \text{ (V mg/ml)}^{-1}$. Accordingly, the numerical parameter is set to $0.02 \text{ (V mg/ml)}^{-1}$.

f_{max} : The maximum concentration of fibrin f_{max} is obtained from the experimental analysis of the blood clot composition as 2.5 mg/ml [71].

W_F, n : The threshold for the activation function controlled by fibrinogen W_f is 1.2 mg/ml [106]. The slope n of all the activation/inhibition functions is 10.

Osteogenic Cell Density and Osteogenic Chemical

D_{C_o}, D_{Q_o} : The diffusion constant for both the osteogenic cells and the osteogenic chemical are taken from [106] as $1.02 \times 10^{-5} \text{ mm}^2/\text{min}$ and $2.88 \times 10^{-3} \text{ mm}^2/\text{min}$ respectively.

H_{Q_o}, E_{C_o} : The chemotactic sensitivity of the cells H_{Q_o} is set to $2.0 \times 10^{-3} \text{ mm}^2/\text{min (ml/mg)}$ as in [106]. The electrical sensitivity is derived as 1.0×10^{-5} from the cell speed [5, 7] and the maximal EF strength that cells can withstand before undergoing irreversible electroporation of the membrane [9].

$r_{C_o}, r_{QD}, r_{QI}, r_{Q_o}$: The production coefficients are taken from [106] as $3.57 \times 10^{-3} \text{ min}^{-1}$, $5.76 \times 10^{-5} \text{ min}^{-1}$, $1.6 \times 10^{-4} \text{ mg/(ml min)}$, and $1.0 \times 10^{-6} \text{ min}^{-1}$, respectively. However, r_{Q_o} was numerical determined as $5.0 \times 10^{-5} \text{ min}^{-1}$ so as to obtain osteogenic chemical concentrations comparable with data on EF cell exposure [60, 74].

r_{QE}, r_{QEI} : Since no related experimental data was found, the EF-mediated chemical production, r_{QE} , is numerically adjusted to $5.0 \times 10^{-5} \text{ min}^{-1}$. The chemical released by the electrically activated platelets, r_{QEI} , is also numerically adjusted to $5.0 \times 10^{-4} \text{ (V min)}^{-1}$.

$\delta_{C_o}, \delta_{Q_o}, \delta_{QC}$: The death coefficients are $1.388 \times 10^{-5} \text{ min}^{-1}$, $2 \times 10^{-3} \text{ min}^{-1}$, and $3 \times 10^{-5} \text{ min}^{-1} \text{ (ml/mg)}$, respectively, as in [106].

C_i, W_{Q_o} : The cell saturation coefficient is set to $1 \times 10^{-3} \text{ cells/ml}$ assuming a normalized cell density [86]. The threshold for the activation function controlled by the chemical W_{Q_o} is $1 \times 10^{-3} \text{ mg/ml}$ [106].

Granulation Tissue

r_G, r_{GE} : The production rate r_G is $8.33 \times 10^{-5} \text{ min}^{-1} \text{ (ml/mg)}$ [106]. The production rate due to EF exposure r_{GE} is set to $2.0 \times 10^{-2} \text{ (V min)}^{-1}$, based on the fact that electrical stimulation enhances the synthesis of collagen by 20-50 % [60, 74].

δ_G, W_{C_o} : The degradation coefficient and the threshold for the activation function controlled by the osteogenic cells are $1.235 \times 10^{-2} \text{ min}^{-1}$ and 0.5 cells/ml , respectively [106].

Displacements

$E_{max}, E_{min}, \nu_{max}, \nu_{min}$: The mechanical properties of fibrin fibers were taken from [71] and adjusted to the values 650 N/m^2 , $1 \times 10^{-3} \text{ N/m}^2$, 250 and 50, respectively [106].

μ_1, μ_2 : The Lamé coefficients for fibrin are both assumed equal to the shear viscosity modulus of elastic polymers and adjusted to 0.3 Pa s as in [106].

$\tau_{C_o}, \lambda_{C_o}$: The individual cell traction constant and the saturation coefficient are based on [88, 139] and adjusted to the values $0.15 \text{ (ml/mg)}^{-1}$ and $2 \times 10^{-5} \text{ (N/m}^2) \cdot \text{(ml/mg)}$ respectively.

a_o, a_{max}, t_{max} : The initial radius for an ideal spherical cell is assumed to be 25×10^{-3} mm [4]. The maximal elongation in the direction perpendicular to the EF is obtained through the experimental measurements performed on cell elongation [126]. By estimating the elongation values from Fig. 5 in [126], we adopted $a_{max} = a_o \frac{0.005E+2.1015}{2.1015}$, with $E = V_B/L$ (see Section 6.3.1). The maximal time for cell elongation t_{max} is taken from the same experimental measurements [126] and is set to 1440 minutes (24 hours).

$h_U, W_{fh}, W_{V_{eh}}$: Variations in the mechanical properties of the fibrillar network are obtained by changing the physiological conditions and by using electrostimulation [71, 127]. Therefore, in order to obtain changes comparable with data in literature, the coupling coefficient h_U is numerically adjusted to 2 (V mg/ml)^{-1} . Furthermore, the threshold values for the activation functions are set to values ensuring the presence of both fibrin and electric potential during the modification of the mechanical properties. Accordingly, $W_{fh} = 2 \text{ mg/ml}$, and $W_{V_{eh}} = 1.0 \times 10^{-3} \text{ V}$.

Osteogenesis

r_{BC}, r_{BQ} : The control parameters for cell adhesion and cell proliferation are based on experimental observations on osteoblastic-like cell cultures [140] and adjusted as in [106] to the values 1 and 75, respectively.

c_4, c_5 : The coefficients for electrical mediation in cell adhesion and cell proliferation are set to reproduce experimental observations according to which the increment of the bone matrix (when using electrostimulation) is the order of 10-20 % [61, 76]. Therefore, the values are 0.4 and 0.16.

W_U : The threshold value for the activation function controlled by the displacements is set to the minimal displacement of the fibers required to obtain a successful osseointegration of the dental implant [129]. Accordingly, the value is set to 0.4 mm.

APPENDIX B

LIST OF PUBLICATIONS

The following list of products summarizes the results obtained during the course of the work presented in this thesis:

Journal articles

Vanegas-Acosta JC, Garzón-Alvarado DA, Zwamborn AP. Mathematical model of electrotaxis in osteoblastic cells. *Biochemistry* 88, 2012: 88-134.

Vanegas-Acosta JC, Garzón-Alvarado DA, Lancellotti. Numerical investigation into blood clotting at the bone-dental implant interface in the presence of an electrical stimulus. Submitted for publication, 2012.

Vanegas-Acosta JC, Garzón-Alvarado DA, Lancellotti. Numerical simulation of electrically stimulated osteogenesis in dental implants. Submitted for publication, 2013.

Book chapters

Guerrero, JA, Vanegas JC, Garzón DA, Casale M and Arzate H. Mechanobiology of oral implantable devices. In: Pignatello R (ed), *Biomaterials science and engineering*. Intech, 2010, pp 309-336.

Awards

J.C. Vanegas was funded by the Universidad Nacional de Colombia through the scholarships program for graduate students or *Programa de Becas a Estudiantes Sobresalientes de Posgrado - PBESP*, years 2010-2013.

Academic internship

J.C. Vanegas worked between June 2010 and August 2010 in the Department of Electrical Engineering at the University of Delaware, USA. He took part of the 2010 Summer Research

APPENDIX B. LIST OF PUBLICATIONS

Internship Program 2010, getting an insight in the field of Computational Electromagnetics. This internship was afforded by the student thanks to the financial support provided by the *Programa de Becas a Estudiantes Sobresalientes de Posgrado - PBESP*, year 2010.

J.C. Vanegas worked between July 2011 and July 2013 in the framework of an academic internship and cooperation project with the Electromagnetics and Microwaves division of the Department of Electrical Engineering at the Eindhoven University of Technology, The Netherlands. This internship was endorsed by the Faculty of Engineering at the Universidad Nacional de Colombia and the PBESP program.

REFERENCES

- [1] MCCAIG C, RAJNICEK A, SONG B & ZHAO M. *Controlling cell behavior electrically: Current views and future potential*. Physiology Review, 85: **2006**; 943–978.
- [2] SIMON J & SIMON B. *Electrical bone stimulation*. En: *Musculoskeletal tissue regeneration. Biological materials and methods.*, (ed.) PIETRZAK W. Humana Press: **2008**, págs. 260–287.
- [3] KUZYK P & SCHEMITSCH E. *The science of electrical stimulation therapy for fracture healing*. International Journal of Orthopaedics, 43(2): **2009**; 127–131.
- [4] FUNK R, MONSEES T & ÖZKUCUR N. *Electromagnetic effects: From cell biology to medicine*. Progress in Histochemistry and Cytochemistry, 43: **2009**; 177–264.
- [5] ZHAO M. *Electrical fields in wound healing - An overriding signal that directs cell migration*. Seminars in Cell and Developmental Biology, 20: **2009**; 674–682.
- [6] FUNK R & MONSEES T. *Effects of electromagnetic fields on cells: Physiological and therapeutic approaches and molecular mechanisms of interaction: A review*. Cells Tissues Organs, 182: **2006**; 59–78.
- [7] ÖZKUCUR N, MONSEES T, PERIKE S, DO H & FUNK R. *Local calcium elevation and cell elongation initiate guided motility in electrically stimulated osteoblast-like cells*. PLoS ONE, 4(7): **2009**; e6131.
- [8] HADDAD J, OBOLENSKY A & SHINNICK P. *The biological effects and therapeutic mechanism of action of electric and electromagnetic field stimulation on bone and cartilage: New findings and a review of earlier work*. The Journal of Alternative and Complementary Medicine, 13(5): **2007**; 485–490.
- [9] CURTZE S, DEMBO M, MIRON M & JONES D. *Dynamic changes in traction forces with DC electric field in osteoblast-like cells*. Journal of Cell Science, 117(13): **2004**; 2721–2729.
- [10] YONEMORI K, MATSUNAGA S, ISHIDOU Y, MAEDA S & YOSHIDA H. *Early effects of electrical stimulation on osteogenesis*. Bone, 19(2): **1996**; 173 – 180.
- [11] GIANNUNZIO G, SPEERLI R & GUGLIELMOTTI M. *Electrical field effect on peri-implant osteogenesis: A histologic and histomorphometric study*. Implant Dentistry, 17(1): **2008**; 118–126.
- [12] AUKHIL I. *Biology of wound healing*. Periodontology 2000, 22: **2000**; 44–50.

REFERENCES

- [13] HÄKKINEN L, UITTO V & LARJAVA H. *Cell biology of gingival wound healing*. *Periodontology* 2000, 24: **2000**; 127–152.
- [14] MOREO P, GARCÍA-AZNAZ J & DOBLARÉ M. *Bone ingrowth on the surface of endosseous implants. Part I: Mathematical model*. *Journal of Theoretical Biology*, 260: **2009**; 1–12.
- [15] AMBARD D & SWIDER P. *A predictive mechano-biological model of the bone-implant healing*. *European Journal of Mechanics and Solids*, 25: **2006**; 927–937.
- [16] ALBREKTSSON T & JOHANSSON C. *Osteoinduction, osteoconduction and osseointegration*. *European Spine Journal*, 10: **2001**; S96–S101.
- [17] HUANG C, CHEN X & CHEN Z. *Osteocyte: The impresario in the electrical stimulation for bone fracture healing*. *Medical Hypotheses*, 70: **2008**; 287–290.
- [18] SCHENK R & BUSER D. *Osseointegration: A reality*. *Periodontology* 2000, 17: **1998**; 22–35.
- [19] HANSSON H, ALBREKTSSON T & BRANEMARK P. *Structural aspects of the interface between tissue and titanium implants*. *Journal of Prosthetic Dentistry*, 50(1): **1983**; 108–113.
- [20] BRANEMARK P. *Osseointegration and its experimental background*. *Journal of Prosthetic Dentistry*, 50(3): **1983**; 399–410.
- [21] ELLINGSEN J, THOMSEN P & LYGSTADAAS P. *Advances in dental implant materials and tissue regeneration*. *Periodontology* 2000, 41: **2006**; 136–156.
- [22] MATSUNO H, YOKOYAMA A, WATARI F, UO M & KAWASAKI T. *Biocompatibility and osteogenesis of refractory metal implants, titanium, hafnium, niobium, tantalum and rhenium*. *Biomaterials*, 22: **2001**; 1253–1262.
- [23] GAPSKI R, WANG H, MASCARENHAS P & LANG N. *Critical review of immediate implant loading*. *Clinical Oral Implants Research*, 14: **2003**; 515–527.
- [24] SIKAVITSAS V, TEMENOFF J & MIKOS A. *Biomaterials and bone mechanotransduction*. *Biomaterials*, 22: **2001**; 2581–2593.
- [25] FRAGISKOS F & ALEXANDRIDIS C. *Osseointegrated Implants*. En: *Oral Surgery*, (eds.) FRAGISKOS F & ALEXANDRIDIS C. Springer Berlin Heidelberg: **2007**, págs. 337–348.
- [26] BAILON-PLAZA A & VAN DER MEULEN M. *A mathematical framework to study the effects of growth factor influences on fracture healing*. *Journal of Theoretical Biology*, 212: **2001**; 191–209.
- [27] AMOR N, GERIS L, VANDER-SLOTEN J & VAN-OOSTERWYCK H. *Modelling the early phases of bone regeneration around an endosseous oral implant*. *Computer Methods in Biomechanics and Biomedical Engineering*, 12(4): **2009**; 459–468.
- [28] HUISKES R, VAN DRIEL W, PRENDERGAST P & SOBALLE K. *A biomechanical regulatory model for periprosthetic fibrous-tissue differentiation*. *Journal of Materials Science: Materials in Medicine*, 8: **1997**; 785–788.
- [29] PATRA A, DEPAOLO J, D’SOUZA K, DETALLA D & MEENAGHAN M. *Guidelines for analysis and redesign of dental implants*. *Implant Dentistry*, 7(4): **1998**; 355–366.

REFERENCES

- [30] LINDHE J, KARRING T & ARAUJO M. *Anatomy of the Periodontium*. En: *Clinical Periodontology and Implant Dentistry*, (eds.) LINDHE J, KARRING T & LANG N. Blackwell Munksgaard: **2003**, págs. 3–49.
- [31] LANG N, ARAUJO M & KARRING T. *Alveolar Bone Formation*. En: *Clinical Periodontology and Implant Dentistry*, (eds.) LINDHE J, KARRING T & LANG N. Blackwell Munksgaard: **2003**, págs. 866–896.
- [32] ADELL R, LEKHOLM U, ROCKLER B & BRANEMARK P. *15-year study of osseointegrated implants in the treatment of the edentulous jaw*. Journal of Oral Surgery, 10: **1981**; 387–416.
- [33] APARICIO C. *Tratamientos de superficie sobre titanio comercialmente puro para la mejora de la osteointegración de los implantes dentales*. Tesis Doctoral, Universitat Politècnica de Catalunya. Barcelona, España.: **2005**.
- [34] ADELL R, HANSSON B, BRANEMARK P & BREINE U. *Intra-osseous anchorage of dental prostheses II. Review of clinical approaches*. Scandinavian Journal of Plastic and Reconstructive Surgery, 4: **1990**; 19–34.
- [35] RATNER B, HOFFMAN A, SHOEN F & LEMONS J. *Biomaterials Science: An Introduction to Materials in Science*. Academic Press, San Diego: **1996**.
- [36] DAVIES J. *Understanding peri-implant endosseous healing*. Journal of Dental Education, 67(8): **2003**; 932–949.
- [37] KLEIN-NULEND J, BACABAC R & MULLENDER M. *Mechanobiology of bone tissue*. Pathologie Biologie, 53: **2005**; 576–580.
- [38] BRANEMARK P, BREINE U, ADELL R, HANSSON O, LINDSTÖM J & OHLSSON A. *Intra-osseous anchorage of dental prostheses I. Experimental studies*. Scandinavian Journal of Plastic and Reconstructive Surgery, 3: **1969**; 81–100.
- [39] MARTÍNEZ J, SÁNCHEZ C, TRAPERIO C, MARTÍNEZ M & GARCÍA F. *Diseño de los implantes dentales: estado actual*. Avances en Periodoncia, 14(3): **2002**; 129–136.
- [40] STANFORD C & SCHNEIDER G. *Functional behavior of bone around dental implants*. Gerodontology, 21: **2004**; 71–77.
- [41] DAVIES J. *Bone bonding at natural and biomaterial surfaces*. Biomaterials, 28: **2007**; 5058–5067.
- [42] LECKHOLM U. *The Surgical Site*. En: *Clinical Periodontology and Implant Dentistry*, (eds.) LINDHE J, KARRING T & LANG N. Blackwell Munksgaard: **2003**, págs. 852–865.
- [43] HEYDENRIJK K, RAGHOEBAR G, MEIJER H, VAN DER REIJDEN W, VAN WINKELHOFF A & STEGENGA B. *Two-stage IMZ implants and ITI implants inserted in a single-stage procedure. A prospective comparative study*. Clinical Oral Implants Research, 13: **2002**; 371–380.
- [44] PULEO D & NANJI A. *Understanding and controlling the bone-implant interface*. Biomaterials, 20: **1999**; 2311–2321.
- [45] HUANG Y, XIROPAIDIS A, SORENSEN R, ALBANDAR J, HALL J & WIKESJÖ U. *Bone formation at titanium porous oxide [TiUnite] oral implants in type IV bone*. Clinical Oral Implants Research, 16: **2005**; 105–111.

REFERENCES

- [46] WENNERBERG A, ALBREKTSSON T & LINDHE J. *Surface Topography of Titanium Dental Implants*. En: *Clinical Periodontology and Implant Dentistry*, (eds.) LINDHE J, KARRING T & LANG N. Blackwell Munksgaard: **2003**, págs. 821–828.
- [47] DIMITRIOU R, TSIRIDIS E & GIANNOUDIS P. *Current concepts of molecular aspects of bone healing*. *Injury: International Journal of the Care of the Injured*, 36: **2005**; 1392–1404.
- [48] MINORS D. *Haemostasis, blood platelets and coagulation*. *Anaesthesia and intensive care medicine*, 8(5): **2007**; 214–216.
- [49] PASI K. *Hemostasis*. En: *Hemostasis and Thrombosis Protocols*, (eds.) PERRY D & PASI K. Humana Press: **1999**, págs. 3–24.
- [50] GORKUN O, VEKLIH Y, WEISEL J & LORD S. *The conversion of fibrinogen to fibrin: Recombinant fibrinogen typifies plasma fibrinogen*. *Blood*, 89(12): **1997**; 4407–4414.
- [51] MALMQUIST J, CLEMENS S, OIEN H & WILSON S. *Hemostasis of oral surgery wounds with the HemCon dental dressing*. *Journal of Oral and Maxillofacial Surgery*, 66: **2008**; 1177–1183.
- [52] ANSELME K. *Osteoblast adhesion on biomaterials*. *Biomaterials*, 21: **2000**; 667–681.
- [53] KASEMO B. *Biological surface science*. *Surface Science*, 500: **2002**; 656–677.
- [54] COLLEN D & LIJNEN H. *Basic and clinical aspects of fibrinolysis and thrombolysis*. *Blood*, 78: **1991**; 3114–3124.
- [55] BURGER E, KLEIN-NULEND J & MULLENDER M. *Mechanobiology of Bone*. En: *Engineered Bone*, (eds.) PETITE H & QUARTO R. Landes Bioscience-Eurekah.com: **2005**, págs. 28–44.
- [56] KNOTHE-TATE M. *Whither flows the fluid in bone? An osteocyte's perspective*. *Journal of Biomechanics*, 36: **2003**; 1409–1424.
- [57] GUGLIELMI G, VIÑUELA F, SEPETKA I & MACELLARI V. *Electrothrombosis of saccular aneurysms via endovascular approach*. *Journal of Neurosurgery*, 75(1): **1991**; 1–7.
- [58] CARDINAL D & FLOWER R. *The electronic aggregometer: A novel device for assessing platelet behavior in blood*. *Journal of Pharmacological Methods*, 3(2): **1980**; 135–158.
- [59] COLE M, VOELCKER N, THISSEN H & GRIESSER H. *Stimuli-responsive interfaces and systems for the control of protein surface and cell surface interactions*. *Biomaterials*, 30: **2009**; 1827–1850.
- [60] CHAO P, LU H, HUNG C, NICOLL S & BULINSKI J. *Effects of applied DC electric field on ligament fibroblast migration and wound healing*. *Connective Tissue Research*, 48: **2007**; 188–197.
- [61] SHAYESTEH Y, ESLAMI B, DEHGHAN M, VAZIRI H, ALIKHASSI M, MANGOLI A & KHOJASTEH A. *The effect of a constant electrical field on osseointegration after immediate implantation in dog mandibles: A Preliminary Study*. *Journal of Prosthodontics*, 16 (5): **2007**; 337–342.
- [62] GENG J, TAN K & LIU G. *Application of finite element analysis in implant dentistry: A review of literature*. *Journal of Prosthetic Dentistry*, 85: **2001**; 585–598.
- [63] ISAKSSON H, VAN DONKELAAR C, HUISKES R & ITO K. *A mechano-regulatory bone-healing model incorporating cell-phenotype specific activity*. *Journal of Theoretical Biology*, 252: **2008**; 230–246.

REFERENCES

- [64] GERIS L, GERISCH A, VANDER-SLOTEN J, WEINER R & VAN-OOSTERWYCK H. *Angiogenesis in bone fracture healing: A bioregulatory model*. Journal of Theoretical Biology, 251: **2008**; 137–158.
- [65] MOREO P, GARCÍA-AZNAJ J & DOBLARÉ M. *Modeling mechanosensing and its effect on the migration and proliferation of adherent cells*. Acta Biomaterialia, 4: **2008**; 613–621.
- [66] DIMILLA P, BARBEE K & LUFFENBURGER D. *Mathematical model for the effects of adhesion and mechanics on cell migration speed*. Biophysics Journal, 60: **1991**; 15–37.
- [67] COLIJN C & MACKEY M. *A mathematical model of hematopoiesis I. Periodic chronic myelogenous leukaemia*. Journal of Theoretical Biology, 237: **2005**; 117–132.
- [68] VANEGAS-ACOSTA J, LANDÍNEZ N & GARZÓN-ALVARADO D. *Mathematical model of the coagulation at the bone-dental implant interface*. Computers in Biology and Medicine, 40(10): **2010**; 791–801.
- [69] TRACQUI P, NAMY P & OHAYON J. *In Vitro Tubulogenesis of Endothelial Cells: Analysis of a Bifurcation Process Controlled by a Mechanical Switch*. En: *Mathematical Modeling of Biological Systems*, (eds.) DEUTSCH A, BRUSCH L, BYME H, DE VRIES G & HERZEL H, tomo I. Springer- Birkhäuser: **2007**, págs. 47–57.
- [70] MANTZARIS N, WEBB S & OTHMER H. *Mathematical modeling of tumor-induced angiogenesis*. Journal of Mathematical Biology, 49: **2004**; 111–187.
- [71] WEISEL J. *The mechanical properties of fibrin for basic scientists and clinicians*. Biophysical Chemistry, 112: **2004**; 267–276.
- [72] SAFFAR J, LASFARGUES J & CHERRUAU M. *Alveolar bone and the alveolar process: The socket that is never stable*. Periodontology 2000, 13: **1997**; 76–90.
- [73] VANEGAS-ACOSTA J, LANDÍNEZ N & GARZÓN D. *Generalidades de la interfase hueso-implante dental*. Revist Cubana de Investigaciones Biomédicas, 28(3): **2009**; 130–146.
- [74] KLOTH L. *Electrical stimulation for wound healing: A review of evidence from in vitro studies, animal experiments, and clinical trials*. Lower Extremity Wounds, 4(1): **2005**; 23–44.
- [75] HART F. *Cytoskeletal forces produced by extremely low-frequency electric fields acting on extracellular glycoproteins*. Bioelectromagnetics, 31(1): **2010**; 77–84.
- [76] HAGIWARA T & BELL W. *Effect of electrical stimulation on mandibular distraction osteogenesis*. Journal of Cranio-Maxillofacial Surgery, 28(1): **2000**; 12–19.
- [77] MADZVAMUSE A, WATHEN A & MAINI P. *A moving grid finite element method applied to a model biological pattern generator*. Journal of Computational Physics, 190: **2003**; 478–500.
- [78] GARZÓN-ALVARADO D. *Simulación de procesos de reacción-difusión: Aplicación a la morfogénesis del tejido óseo*. Tesis Doctoral, Zaragoza, España: **2007**.
- [79] MAINI P. *Using mathematical models to help understand biological pattern formation*. Comptes Rendus Biologies, 327(3): **2004**; 225–234.
- [80] TURING A. *The chemical basis of morphogenesis*. Philosophical Transactions of the Royal Society, 237: **1957**; 37–72.

REFERENCES

- [81] MURRAY J. *Mathematical Biology II: Spatial models and biomedical applications*. Springer-Verlag: **1993**.
- [82] MURRAY J. *Mathematical Biology I: An introduction*. Springer-Verlag: **2002**.
- [83] VANEGAS-ACOSTA J, LANDÍNEZ N & GARZÓN-ALVARADO D. *Analysis of Turing instabilities in biological models*. Revista DYNA. Universidad Nacional de Colombia - Medellín., 158: **2009**; 123–134.
- [84] WANG Z, LI W & RUAN S. *Travelling wave fronts in reaction-diffusion systems with spatio-temporal delays*. Journal of Differential Equations, 222: **2006**; 185–232.
- [85] PAGE K, MAINI P & MONK N. *Pattern formation in spatially heterogeneous Turing reaction diffusion models*. Physica D, 181: **2003**; 80–101.
- [86] PAINTER K. *Chemotaxis as a mechanism for morphogenesis*. Tesis Doctoral, United Kingdom: Oxford University: **1997**.
- [87] MAINI P. *Spatial pattern formation in chemical and biological systems*. Journal of the Chemical Society, Faraday Transactions, 93(20): **1997**; 3601–3610.
- [88] MURRAY J & OSTER G. *Cell traction models for generation pattern and form in morphogenesis*. Journal of Mathematical Biology, 19: **1984**; 265–279.
- [89] IZAGUIRRE J, CHATURVEDI R, HUANG C & CICKOVSKI T. *Compucell, a multi-model framework for simulation of morphogenesis*. Bioinformatics, 20: **2004**; 1129–1137.
- [90] MADZVAMUSE A. *A numerical approach to the study of spatial pattern formation*. Tesis Doctoral, Oxford, UK, Computing Laboratory. University of Oxford: **2000**.
- [91] CRAMPIN E. *Reaction diffusion patterns on growing domains*. Tesis Doctoral, Oxford, UK, Magdalen College. University of Oxford: **2000**.
- [92] RAO S. *The Finite Element Method in Engineering*. Elsevier Science and Technology Books: **2004**.
- [93] OÑATE E, MIQUEL J & ZÁRATE F. *Stabilized solution of the multidimensional advection-diffusion-absorption equation using linear finite elements*. Computers and Fluids, 36: **2007**; 1–111.
- [94] OÑATE E. *Cálculo de Estructuras por el Método de los Elementos Finitos*. CIMNE, España: **1992**.
- [95] ZIENKIEWICZ O & TAYLOR R. *The Finite Element Method. Solid Mechanics*, tomo 2. Butterworth-Heinemann: **2000**.
- [96] HOFFMAN J. *Numerical Methods for Engineers and Scientists*. Marcel Dekker Inc, New York: **2001**.
- [97] HIBBIT, KARLSSON & INC S. *Abaqus User Guide V. 6.6*. HKS Inc., Pawtucket, RI, USA: **2004**.
- [98] VANEGAS J, LANDÍNEZ N & GARZÓN D. *Computational solution of biological models of spatial-temporal pattern formation*. Ingeniare Revista chilena de ingeniería, 17(2): **2009**; 182–194.
- [99] ZHAO M, PU J, FORRESTER J & MCCAIG C. *Membrane lipids, EGF receptors, and intracellular signals colocalize and are polarized in epithelial cells moving directionally in a physiological electric field*. Journal of the Federation of American Societies for Experimental Biology, 16: **2002**; 857–859.
- [100] ZHAO M, SONG B, PU J, WADA T, REID B, TAI G, WANG F, GUO A, WALCZYNSKO P, GU Y, SASAKI T, SUZUKI A, FORRESTER J, BOURNE H, DEVREOTES P, MCCAIG C & PENNINGER J. *Electrical signals*

REFERENCES

- control wound healing through phosphatidylinositol-3-OH kinase- γ and PTEN.* Nature, 442: **2006**; 457–460.
- [101] RAJNICEK A, FOUBISTER L & MCCAIG C. *Prioritising guidance cues: Directional migration induced by substratum contours and electrical gradients is controlled by a rho/cdc42 switch.* Dev Biol, 312(1): **2007**; 448 – 460.
- [102] OLSEN L, SHERRATT J & MAINI P. *A mechanochemical model for adult dermal wound contraction and the permanence of the contracted tissue displacement profile.* Journal of Theoretical Biology, 177: **1995**; 113–128.
- [103] BISTOLFI F. *Evidence of interlinks between bioelectromagnetics and biomechanics: from biophysics to medical physics.* Physica Medica, 22: **2006**; 71–95.
- [104] EROL O, UYSAL O & AGAOGLU G. *Percutaneous Electrothrombosis: A Minimally Invasive Technique for the Treatment of Deep Hemangiomas.* Aesthetic Plastic Surgery, 34: **2010**; 214–217.
- [105] HENKES H, BREW S, FELBER S, MILOSLAVSKI E, MOGILEVSKI G, TAVROVSKI I & KÜHNE D. *In vitro and in vivo studies of the extent of electrothrombotic deposition of blood elements on the surface of electrolytically detachable coils.* Interventional Neuroradiology, 10(3): **2004**; 189–201.
- [106] VANEGAS-ACOSTA J, LANDÍNEZ N, GARZÓN-ALVARADO D & CASALE M. *A finite element method approach for the mechanobiological modeling of the osseointegration of a dental implant.* Computer Methods and Programs in Biomedicine, 101(3): **2011**; 297–314.
- [107] FROESCH E, SCHMID C, SCHWANDER J & ZAPF J. *Actions of insulin-like growth factors.* Annual Review of Physiology, 47: **1985**; 443–467.
- [108] LAMI E, MATTACHINI F, SALA R & VIGL H. *A mathematical model of electrostatic field in wires-plate electrostatic precipitators.* Journal of Electrostatics, 39: **1997**; 1–12.
- [109] SHIAU Y & VALENTINO A. *ELF electric field coupling to dielectric spheroidal models of biological objects.* IEEE Transactions on Biomedical Engineering, 28(6): **1981**; 429–437.
- [110] MONSEES T, BARTH K, TIPPELT S, HEIDEL K, GORBUNOV A, POMPE W & FUNK R. *Effects of different titanium alloys and nanosize surface patterning on adhesion, differentiation, and orientation of osteoblast-like cells.* Cells Tissues Organs, 180: **2005**; 81–95.
- [111] EISENBACH M, ZIMMERMAN J, CIOBOTARIU A, FISCHLER H & KORENSTEIN R. *Electric field effects on bacterial motility and chemotaxis.* Bioelectrochemistry and Bioenergetics, 10(5-6): **1983**; 499 – 510.
- [112] HWANG S, SONG J, CHO T, SONG Y, LEE T, CHOUNG S, JANG J, KIM I & KIM J. *Enhanced bone formation around dental implant using electrical stimulation.* Bioengineering Conference, 2007. NEBC '07. IEEE 33rd Annual Northeast: **2008**; 11 – 12.
- [113] BUTENAS S & MANN K. *Blood coagulation.* Biochemistry, 67(1): **2002**; 3–12.
- [114] SAWYER P, DENNIS C & WESOLOWSKI S. *Electrical hemostasis in uncontrollable bleeding states.* Annals of Surgery, 154(4): **1961**; 556–562.

REFERENCES

- [115] WOLBERG A & CAMPBELL R. *Thrombin generation, fibrin clot formation and hemostasis*. Transfusion and Apheresis Science, 38: **2008**; 15–23.
- [116] SHUEY K. *Platelet-associated bleeding disorders*. Seminars in oncology nursing, 12(1): **1996**; 15–27.
- [117] HEUCK C, SCHIELE U, HORN D, FRONDA D & RITZ E. *The role of surface charge on the accelerating action of heparin on the antithrombin III-inhibited activity of alpha-thrombin*. Journal of Biological Chemistry, 260(8): **1985**; 4598–603.
- [118] HANDAGAMA P, SCARBOROUGH R, SHUMAN M & BAINTON D. *Endocytosis of fibrinogen into megakaryocyte and platelet α -granules is mediated by Iib 3 (glycoprotein Iib-IIIa)*. Blood, 82(1): **1993**; 135–138.
- [119] SCHULZ-HEIK K, RAMACHANDRAN J, BLUESTEIN D & JESTY J. *The extent of platelet activation under shear depends on platelet count: Differential expression of anionic phospholipid and factor Va*. Pathophysiology of Haemostasis and Thrombosis, 34: **2005**; 255–262.
- [120] VANEGAS-ACOSTA J, LANDÍNEZ N & GARZÓN-ALVARADO D. *Modelo matematico de la coagulacion en la interfase hueso-implante dental*. Revist Cubana de Investigaciones Biomédicas, 28: **2009**; 167–191.
- [121] KASEMO B & LAUSMAA J. *The Biomaterial-Tissue Interface and its Analogues in Surface Science and Technology*. En: *The Bone-Biomaterial Interface*, (ed.) DAVIES J. University of Toronto Press: **1991**, págs. 19–32.
- [122] PARK J, GEMMELL C & DAVIES J. *Platelet interactions with titanium: modulation of platelet activity by surface topography*. Biomaterials, 22: **2001**; 2671–2682.
- [123] VANEGAS-ACOSTA J, GARZÓN-ALVARADO D & ZWAMBORN A. *Mathematical model of electrotaxis in osteoblastic cells*. Bioelectrochemistry, 8: **2012**; 134 – 143.
- [124] AARON R, BOYAN B, CIOMBOR D, SCHWARTZ Z & SIMON B. *Stimulation of growth factor synthesis by electric and electromagnetic fields*. Clinical Orthopaedics and Related Research, 419: **2004**; 30–37.
- [125] AARON R & CIOMBOR D. *Therapeutic effects of electromagnetic fields in the stimulation of connective tissue repair*. Journal of Cellular Biochemistry, 52(1): **1993**; 42–46.
- [126] ZHAO M, BAI H, WANG E, FORRESTER J & MCCAIG C. *Electrical stimulation directly induces pre-angiogenic responses in vascular endothelial cells by signaling through VEGF receptors*. Journal of Cell Science, 117: **2003**; 397–405.
- [127] PARK J & KENNER G. *Effect of electrical stimulation on the tensile strength of the porous implant and bone interface*. Artificial Cells, Blood Substitutes and Biotechnology, 3(2): **1975**; 233–243.
- [128] SIEBERS M, BRUGGE P, WALBOOMERS X & JANSSEN J. *Integrins as linker proteins between osteoblasts and bone replacing materials: A critical review*. Biomaterials, 26: **2005**; 137–146.
- [129] FRANCHI M, FINI M, GIAVARESI G & OTTANI V. *Peri-implant osteogenesis in health and osteoporosis*. Micron, 36: **2005**; 630–644.
- [130] MITTELMEIER W, LEHNER S, KRAUS W, MATTER H, GERDESMAYER L & STEINHAUSER E. *BISS: concept and biomechanical investigations of a new screw system for electromagnetically induced internal osteostimulation*. Archives of Orthopaedic and Trauma Surgery, 124: **2004**; 86–91.

REFERENCES

- [131] LINCKS J, BD B, BLANCHARD C, LOHMANN C, LIU Y, COCHRAN D, DEAN D & SCHWARTZ Z. *Response of MG63 osteoblast-like cells to titanium and titanium alloy is dependent on surface roughness and composition*. *Biomaterials*, 19(23): **1998**; 2219 – 2232.
- [132] RAJNICEK A, FOUBISTER L & McCAIG C. *Prioritising guidance cues: Directional migration induced by substratum contours and electrical gradients is controlled by a rho/cdc42 switch*. *Developmental Biology*, 312(1): **2007**; 448 – 460.
- [133] PADOLECCHIA R, GUGLIELMI G, PUGLIOLI M, CASTAGNA M, NARDINI V, COLLAVOLI P, GUIDETTI G, DAZZI M, ZUCCHI V & NARDUCCI P. *Role of Electrothrombosis in Aneurysm Treatment with Guglielmi Detachable Coils: An In Vitro Scanning Electron Microscopic Study*. *American Journal of Neuroradiology*, 22(9): **2001**; 1757–1760.
- [134] BÄCHLE M & KOHAL R. *A systematic review of the influence of different titanium surfaces on proliferation, differentiation and protein synthesis of osteoblast-like MG63 cells*. *Clinical Oral Implants Research*, 15(6): **2004**; 683–92.
- [135] RAJNICEK A, FOUBISTER L & D McCAIG C. *Alignment of corneal and lens epithelial cells by co-operative effects of substratum topography and DC electric fields*. *Biomaterials*, 29(13): **2008**; 2082 – 2095.
- [136] TSONG T. *Electroporation of cell membranes*. *Biophysical Journal*, 60(2): **1991**; 297 – 306.
- [137] PU J & ZHAO M. *Golgi polarization in a strong electric field*. *J Cell Sci*, 118(6): **2005**; 1117–1128.
- [138] HINKLE L, McCAIG C & ROBINSON K. *The direction of growth of differentiating neurones and myoblasts from frog embryos in an applied electric field*. *Journal of Physiology*, 314: **1981**; 121–35.
- [139] TRANQUI L & TRACQUI P. *Mechanical signalling and angiogenesis. The integration of cell-extracellular matrix couplings*. *Comptes Rendus de l'Académie des sciences*, 323: **2000**; 31–47.
- [140] GUERRERO J, VANEGAS-ACOSTA J, GARZÓN-ALVARADO D, CASALE H & ARZATE H. *Mechanobiology of Oral Implantable Devices*. En: *Biomaterials Science and Engineering*, (ed.) PIGNATELLO R. InTech: **2011**, págs. 309–336.